

VOLUMETRIC RANDOM PHASED ARRAYS AND THEIR APPLICATIONS

A Dissertation

by

SHIH-YUAN YEH

Submitted to the Office of Graduate and Professional Studies of
Texas A&M University
in partial fulfillment of the requirements for the degree of

DOCTOR OF PHILOSOPHY

Chair of Committee,	Gregory H. Huff
Committee Members,	Robert D. Nevels
	Jean-Francois Chamberland
	Harlan Rusty Harris
Head of Department,	Miroslav Begovic

August 2018

Major Subject: Electrical Engineering

Copyright 2018 Shih-Yuan Yeh

ABSTRACT

This dissertation mainly focuses on the topics of phased array, volumetric array, random array, circular polarization, beamforming, beamshaping, mobile platform, and all these combinations. The ultimate goal was to realize wireless phased array applications carried out by mobile platforms. To make this idea into reality, there are some challenges we need to overcome. The first one is the wireless phase synchronization, and not only the frequency but also the phases should be synchronized. The second challenge is to know the relative position location and global position orientation of each array element. The last is to develop collaborative beamforming algorithms, which is the major contribution of this dissertation.

There is a total of five projects in this dissertation. The first one constructed a volumetric random array with two types of dissimilar antennas and generated a circular polarized radiation pattern. The goals were to understand how to make diverse antennas work cooperatively and what is the standardized step by step procedures to achieve the best system performance.

The second project generated a circular polarized radiation pattern with each antenna element arbitrarily oriented and distributed randomly within a volume. The purpose of giving each antenna element some freedoms of rotation is to simulate the real mobile platform environment.

The third project developed an amplitude tapering algorithm for the volumetric random array. The reason to apply the amplitude tapering on random array is because the

sidelobe cancellation for a small number of elements is trivial. For this reason, it is necessary to apply amplitude tapering on random array to further reduce the sidelobe level.

The fourth project investigated the reflect beamforming how the incident waves reflect back to the original direction or to a specific direction. Therefore, the project is separated to two parts. Part A is to develop a retrodirective array prototype, which has the same functionality as a reflector based on the Van Atta array structure. Then part B added additional phase shifters to make the prototype become a signal relay system.

The fifth project investigated both the indirect beamforming and amplitude tapering techniques implemented on a metal plate with circular slots. One advantage of this topology is to create a two-hundred-element array radiation pattern by using a single plane wave excitation. Beam scanning by moving the plane wave excitation was also investigated.

ACKNOWLEDGEMENTS

I would like to thank the committee chair, Dr. Huff, and the committee members, Dr. Nevels, Dr. Chamberland, and Dr. Harris, for their unlimited patience, advisories, and supports throughout this research. I also like to express my special gratitude to Dr. Huff, who inspired and led me to the volumetric random phased array.

Appreciations also go to the National Chung-Shan Institute of Science and Technology that provides me everything to advance my research.

No doubt, my wife, Leah W. Yeh, puts lots of efforts and energy taking good cares of our kids, Jessie and Ryan. She made a fantastic job, so I would like to share my achievements with her.

It is so honorable to become parts of the Aggie families. I have a wonderful time and fabulous journey at Texas A&M University.

CONTRIBUTORS AND FUNDING SOURCES

Dr. Huff is my research advisor, and he is also my committee chair. Other committee members, such as Dr. Nevels, Dr. Chamberland, and Dr. Harris, are also the contributors of this dissertation.

The National Chung-Shan Institute of Science and Technology provides me full-time in-service educational scholarship to advance my research.

NOMENCLATURE

5G	5 th generation mobile networks / 5 th generation wireless systems
AESA	Active Electronically Scanned Array
AF	Array Factor
ARP	Antenna Reference Point
BER	Bit Error Rate
C/N	Carrier-to-noise Ratio
CW	Continuous Wave
COTS	Commercial off-the-shelf
DAC	Digital to Analog Converter
DF	Direction Finding
DOA	Direction-of-arrival
DOF	Degrees of Freedom
DPS	Degrees per Second
EP	Element Pattern
FOV	Field of View
GO	Geometrical Optics
GPS	Global Positioning System
HPBW	Half-Power Beamwidth
I	In-Phase
IMU	Inertial Measurement Unit

LAN	Local Area Network
LHCP	Left Hand Circular Polarization
LNA	Low-Noise Amplifier
LO	Local Oscillator
MIMO	Multiple-input and Multiple-output
PA	Power Amplifier
PCB	Printed Circuit Board
PEC	Perfect Electrical Conductor
PMF	Polarization Mismatch Factor
PLL	Phase Locked Loop
Q	Quadrature
RADAR	Radio Detection and Ranging
RCS	Radar Cross-section
RF	Radio Frequency
RHCP	Right Hand Circular Polarization
RX	Receive
SLL	Sidelobe Level
SNR	Signal-to-noise Ratio
T/R	Transmit/Receive
TX	Transmit
UAV	Unmanned Aerial Vehicle
VCC	Voltage at the Common Collector

VCO	Voltage-controlled Oscillator
VNA	Vector Network Analyzer
VSWR	Voltage Standing Wave Ratio

TABLE OF CONTENTS

	Page
ABSTRACT	ii
ACKNOWLEDGEMENTS	iv
CONTRIBUTORS AND FUNDING SOURCES.....	v
NOMENCLATURE.....	vi
TABLE OF CONTENTS	ix
LIST OF FIGURES.....	xii
LIST OF TABLES	xvii
1. INTRODUCTION.....	1
1.1. Phased Array	1
1.2. Volumetric Array	4
1.3. Random Array.....	5
1.4. Circular Polarization	7
1.5. Wireless Phased Arrays on Mobile Platforms.....	9
1.6. Wireless Phase Synchronization	11
2. AN INVESTIGATION OF BEAMFORMING USING DISSIMILAR ANTENNAS IN VOLUMETRIC RANDOM ARRAYS.....	13
2.1. Introduction	13
2.2. Antennas.....	15
2.2.1. Microstrip Patch	15
2.2.2. Monopole	17
2.2.3. Phase Center Estimation.....	18
2.3. Array.....	20
2.3.1. Distance Phase from the Scan Angle	21
2.3.2. Rotation Phase - RHCP	22
2.3.3. Amplitude Equalization.....	22
2.4. Experiment	23
2.4.1. Anechoic Chamber	23
2.4.2. Simulation Testing	23

2.4.3. Integrated Array System Hardware	24
2.4.4. 90° Hybrid Coupler	26
2.5. Results	29
2.6. Conclusion.....	34
2.6.1. Discussion	34
2.6.2. Summary	34
3. CIRCULAR POLARIZED BEAMFORMING ON VOLUMETRIC RANDOM ARRAYS WITH ARBITRARILY ORIENTED ARRAY ELEMENTS	35
3.1. Introduction	35
3.2. Beamformer System Overview	38
3.2.1. Microstrip Patch Antenna.....	39
3.2.2. Vector Modulator	42
3.2.3. Voltage Control Board	43
3.2.4. Spatial Recognition System	44
3.2.5. Antenna Orientation	46
3.3. RHCP Rotation Phase Estimation.....	47
3.4. Experiments and Results	47
3.5. Conclusion.....	50
3.5.1. Discussion	50
3.5.2. Summary	50
4. AMPLITUDE TAPERING ON VOLUMETRIC RANDOM ARRAYS*	51
4.1. Introduction	51
4.2. Theory	52
4.2.1. Previous Work.....	52
4.2.2. Amplitude Tapering for Linear and Planar Arrays	53
4.2.3. Preliminary Test	54
4.3. 3D Amplitude Tapering Procedures.....	57
4.3.1. Beamforming and Phase Optimization	59
4.3.2. Tapering Methods	59
4.3.3. Define Array Aperture	60
4.3.4. Amplitude Mapping (Binomial).....	61
4.3.5. Amplitude Averaging.....	62
4.3.6. Depth Gain	63
4.4. Simulated and Measurement Results	64
4.5. Conclusion.....	67
5. A MAGNETLESS DUPLEX RETRODIRECTIVE PATCH ARRAY WITH PHASE SHIFTERS FOR SIGNAL RELAY	68
5.1. Introduction	68
5.2. Retrodirective Array Prototype Overview	71

5.2.1. Aperture-coupled Microstrip Patch Antenna	74
5.2.2. Directional Coupler	77
5.2.3. Crossover Ring.....	78
5.2.4. Delay Line Phase Shifter.....	80
5.3. Array Radiation Pattern Analysis.....	83
5.3.1. Geometrical Optics Analysis.....	83
5.3.2. Scattered Field.....	87
5.3.3. Reradiated Field	88
5.4. Experiment and Results.....	89
5.4.1. Retrodirective Array Prototype	89
5.4.2. Radiation Pattern of the Retrodirective Array Prototype	90
5.4.3. Retrodirective Array as a Relay System	100
5.4.4. Radiation Pattern of the Relay System.....	102
5.5. Conclusion.....	103
6. AN INVESTIGATION OF INDIRECT BEAMFORMING AND BEAMSHAPING IMPLEMENTED ON A SLOT ARRAY	104
6.1. Introduction	104
6.2. Array Overview.....	105
6.2.1. Metal Plate.....	105
6.2.2. Circular Slots.....	107
6.2.3. Plane Wave Excitation	108
6.3. Array Beamshaping.....	108
6.3.1. Tapering Method	109
6.3.2. Find the Array Aperture	110
6.3.3. Distribution Counts	111
6.3.4. Amplitude Mapping	114
6.3.5. Slot Aperture vs. Amplitude.....	115
6.4. Array Indirect Beamforming.....	118
6.5. Simulation Results.....	118
6.6. Conclusion.....	126
7. CONCLUSION AND FUTURE WORK.....	127
REFERENCES.....	128

LIST OF FIGURES

	Page
Figure 1 Average SLL vs. Antenna Elements.	7
Figure 2 A wireless phased array beamforming system carried out by drones.....	10
Figure 3 The simulated volumetric random array modeled in the HFSS.....	14
Figure 4 Simulated VSWR and Smith chart (overlaid) of the microstrip patch.	16
Figure 5 Simulated radiation pattern (dB) of the microstrip patch.	16
Figure 6 Simulated VSWR and Smith chart (overlaid) of the monopole.	17
Figure 7 Simulated radiation pattern (dB) of the monopole.	18
Figure 8 Phase variation of the patch antenna with $\phi = 0^\circ$ and θ scans from -45° to 45°	19
Figure 9 Phase variation of the monopole antenna with $\phi = 90^\circ$ and θ scans from -45° to 45°	20
Figure 10 Structure of the thirty-two-element volumetric random array beamformer. ...	25
Figure 11 The thirty-two-element volumetric random array was placed in the anechoic chamber.	26
Figure 12 Signal in and out of the symmetric four-port coupler.....	27
Figure 13 Photograph of the coupler connects with the receiver in the chamber.	28
Figure 14 Comparison of measured and simulated G_θ pattern.....	29
Figure 15 Comparison of measured and simulated G_ϕ pattern.....	30
Figure 16 Comparison of measured and simulated G_{RHCP} pattern.....	31
Figure 17 Comparison of measured and simulated G_{LHCP} pattern.	32
Figure 18 The photograph of the Medusa platform placed on the pedestal in the anechoic chamber.	37
Figure 19 Beamformer architecture.	39

Figure 20 Measured VSWR and Smith Chart (overlaid) of the microstrip patch.	41
Figure 21 Measured radiation pattern (dB) of the microstrip patch.	41
Figure 22 Photo of a voltage control board.	44
Figure 23 A volumetric random phased array placed on the turning table and a camera is used to capture the XYZ positions of the array.	46
Figure 24 Comparison of measured and simulated G_{RHCP} pattern.	48
Figure 25 Comparison of measured and simulated G_{LHCP} pattern.	49
Figure 26 Radiation patterns of the linear random array with (right) and without (left) amplitude tapering.	55
Figure 27 Radiation patterns of the planar random array with (right) and without (left) amplitude tapering.	56
Figure 28 Radiation patterns of the volumetric random array with (right) and without (left) amplitude tapering.	56
Figure 29 A sixteen-element volumetric random array modeled in the HFSS.	58
Figure 30 A sixteen-element volumetric random array implemented on the Medusa platform and measured in the anechoic chamber.	58
Figure 31 Sixteen array elements (red cross) projected on the array aperture.	60
Figure 32 Sixteen array elements map to the normalized amplitude tapering curve (blue curve).	61
Figure 33 Amplitude averaging for proximity antennas.	62
Figure 34 Propagation loss of an antenna from 0 m to 0.5 m.	63
Figure 35 Simulation results of tapering, non-tapering, and expected value ($\phi = 0^\circ$).	65
Figure 36 Measured results of tapering, non-tapering, and expected value ($\phi = 0^\circ$).	66
Figure 37 Photo of the designed retrodirective array: top layer (left), middle layer (center), and bottom layer (right).	70
Figure 38 A 3D transparent layout of the retrodirective array designed in the HFSS.	71
Figure 39 A geometry and system block diagram of the retrodirective array prototype.	72

Figure 40 Photographs of the edge feed patch (left; $L \times W = 120 \text{ mm} \times 110 \text{ mm}$) and the aperture-coupled feed patch (right; $L \times W = 115 \text{ mm} \times 65 \text{ mm}$) retrodirective arrays.	73
Figure 41 Aperture-coupled patch antennas with normal (left) and reversed (right) feed topology.	75
Figure 42 Simulated $ S_{11} $ of the aperture-coupled microstrip patch.	76
Figure 43 Simulated radiation pattern (dB) of the microstrip patch.	76
Figure 44 Geometry of the directional coupler.	77
Figure 45 Simulated S_{21} and S_{31} of the directional coupler.	78
Figure 46 Geometry of the crossover ring structure.	79
Figure 47 Simulated S_{41} and S_{31} of the crossover ring.	80
Figure 48 Illustration of a plane wave ($\theta_i, \phi_i = 0^\circ$) incidents on the relay system.	82
Figure 49 Parallel polarized plane wave reflects and refracts between boundaries.	84
Figure 50 Two-element retrodirective array positioned along the x-axis ($\phi_i = 0^\circ$).	88
Figure 51 Simulated bistatic RCSs (normal incidence) of a metal plate, the scattered plate, the retrodirective array ($l = -720^\circ$), and a normalized patch array radiation pattern.	91
Figure 52 Simulated bistatic RCSs (normal incidence) of a metal plate, the scattered plate, the retrodirective array ($l = -900^\circ$), and a normalized patch array radiation pattern.	93
Figure 53 Simulated bistatic RCSs (oblique incidence) of a metal plate, the scattered plate, the retrodirective array ($l = -720^\circ$), and a normalized patch array radiation pattern.	95
Figure 54 Simulated bistatic RCSs (oblique incidence) of a metal plate, the scattered plate, the retrodirective array ($l = -900^\circ$), and a normalized patch array radiation pattern.	96
Figure 55 Simulated bistatic RCSs of the retrodirective array with oblique TM polarized plane wave incidence ($\theta_i = 0^\circ, 15^\circ, 30^\circ, \phi_i = 0^\circ; l = -720^\circ$).	97

Figure 56 Simulated monostatic RCSs of a metal plate, the scattered plate, the retrodirective array ($l = -720^\circ$), and a normalized patch array radiation pattern.	98
Figure 57 Simulated monostatic RCSs of a metal plate, the scattered plate, the retrodirective array ($l = -900^\circ$), and a normalized patch array radiation pattern.	99
Figure 58 The retrodirective array relay system ($L \times W = 126 \text{ mm} \times 65 \text{ mm}$).	101
Figure 59 Measured bistatic radiation pattern of the retrodirective array relay system along with the simulated two-element patch array.	102
Figure 60 A two-hundred-element slot array prototype simulated in the HFSS.	106
Figure 61 A photo of the two-hundred-element slot array prototype.	106
Figure 62 A photo of the slot array in the middle of two plastic board.	107
Figure 63 Two hundred circular slots (red cross) projected on the array aperture, and the center blue dot is the aperture origin.	110
Figure 64 Counts distribution along the array aperture – horizontal tapering.	111
Figure 65 Amplitude adjustment according to the counts – horizontal tapering.	112
Figure 66 Distribution counts slots along the array aperture – radial tapering.	113
Figure 67 Amplitude adjustment according to the counts – radial tapering.	113
Figure 68 Two hundred circular slots map to the normalized amplitude tapering curve (blue curve) – horizontal tapering.	114
Figure 69 Two hundred circular slots map to the normalized amplitude tapering curve (blue curve) – radial tapering.	115
Figure 70 Field amplitudes vs. slot aperture.	116
Figure 71 The estimated slot aperture for each circular slot – horizontal tapering.	117
Figure 72 The estimated slot aperture for each circular slot – radial tapering.	117
Figure 73 The slot array with horizontal tapering modeled in the HFSS (left), and the fabricated plate (right).	119

Figure 74 The slot array with radial tapering modeled in the HFSS (left), and the fabricated plate (right).	119
Figure 75 Simulation results of the slot array prototype and the array with horizontal tapering.	120
Figure 76 Simulation results of the slot array prototype and the array with radial tapering.	121
Figure 77 Simulation results of the slot array prototype and the rotated array with radial tapering.	122
Figure 78 Simulation results of the slot array prototype and the array with horizontal tapering for $(\theta_i, \phi_i) = (30^\circ, 0^\circ)$	123
Figure 79 Simulation results of the slot array prototype and the array with radial tapering for $(\theta_i, \phi_i) = (30^\circ, 0^\circ)$	124
Figure 80 Simulation results of the array prototype and the rotated array with radial tapering for $(\theta_i, \phi_i) = (30^\circ, 0^\circ)$	125

LIST OF TABLES

	Page
Table 1 - Properties of the Radiation Pattern	33
Table 2 - Phases at each antenna element of different plane wave incident and main beam reflection angles for the two delay line phase shifters with 19.94 mm length difference.....	82
Table 3 - The corresponding θ_r , θ_t , and electric fields with the known incident angles...	85
Table 4 - Round-trip phase delay of the wave propagating along the substrate (31 mil thickness) with different refraction angles	86

1. INTRODUCTION

This research work mainly focuses on the topics of phased array, volumetric array, random array (both position and orientation are random), circular polarization, beamforming, beamshaping, mobile platform, and all these combinations. The ultimate goal was to realize wireless phased array applications carried out by mobile platforms.

1.1. Phased Array

Phased arrays have been used on applications, such as radar, direction finding (DF), tracking, missile guiding, navigation, jamming, or communication system, for many years. One major advantage of the phased array is it scans the beams electronically with the speed of the microprocessor, which is much faster than the conventional mechanical scan. From a system's point of view, phased arrays are reliable and redundant to the single point of failure. Clearly even when parts of the array elements fail, the array beamformer still can drive the main beam with a little compromise of power and gain reduction. With the narrow pencil beam characteristics, driving the main beam to the designated direction mitigates the interferences, which is very helpful for the communication.

The electronically scanned phased array system includes active/passive components, such as antenna, circulator, phase shifter, attenuator, power combiner, transmission line, power amplifier (PA), low-noise amplifier (LNA), and so on [1]. As an incident wavefront arrives at the array antenna, it creates phase delay among antennas. For uniform distributed array elements with equal spacing d , the progressive phase shift ξ can be calculated as $\xi = \beta d \cdot \cos\theta$, where β is the phase constant and θ is the incident angle

between the rays and the array baseline. By well adjusting the phases of each antenna element, we can drive the array elements simultaneously and form a main beam to the desired angle. Ideally the total array fields are the summation of individual antenna field (based on the superposition theorem), and people like to use the pattern multiplication method to describe this field pattern. The total field is the array factor (AF) multiplies the element pattern (EP) and is expressed as

$$F(\theta, \phi) = AF(\theta, \phi) \cdot EP(\theta, \phi) \quad (1)$$

The AF is the pattern of the whole array with antennas replaced by an isotropic radiator. The EP is the pattern of the specific antenna placed at the origin. Keep in mind, this is a general expression for most of the cases. For some complex phased arrays like using dissimilar antennas, or antennas with arbitrary orientation in this dissertation, the general form still can be used, but has to be modified and transformed to

$$F(\theta, \phi) = \sum_{n=1}^N [A_n e^{j\psi_n} \cdot EP_n(\theta_n, \phi_n)], \quad (2)$$

where A_n is the amplitude and $e^{j\psi_n}$ is the phase of the n -th array element.

For many years of development, phased array techniques have been widely spread and used for civilian application. Commercial off-the-shelf (COTS) components become easily to acquire and cheap to buy on the market. Therefore, there are more and more commercial applications that start to build their systems on the phased array platform and replace the single antenna system. For instance, one arising application is the 5th generation mobile networks (5G). In 5G networks, there are five major breakthroughs compared to the previous generation, and they are full duplex, phased array beamforming, massive multiple-input and multiple-output (MIMO), millimeter wave, and small cells.

Obviously, the phased array beamforming should work together with DF and tracking to make beamforming become meaningful. Based on the reciprocity theorem, no matter whether the base station or personal devices do the beamforming; the received power from either side would increase evenly. In 5G, to provide more data rate, these changes mentioned above are reasonable and inevitable. The question is why the 5G chooses the phased array as its antenna candidate. The following is from the Shannon capacity limit

$$C = B \cdot \log_2 \left(1 + \frac{S}{N} \right), \quad (3)$$

where C is the channel capacity in bits/s, B is the bandwidth in Hz, and S/N is the signal-to-noise ratio (SNR) in Watt. To provide users higher data rate, it is necessary to provide either higher bandwidth or SNR. One way to do this is to shift the frequency all the way up to millimeter wave band. Moreover, using phased arrays can significantly increase the gain and power at the same time. Ideally, an N -element phased array has N times SNR, gain, transmitting power, and N^2 times received power compared to one single antenna. With high SNR, not only can advanced modulation techniques like 64-QAM be used to increase the bandwidth efficiency, but also bit error rate (BER) can be reduced [2]. It is obvious for certain modulation techniques that the carrier-to-noise ratio (C/N) increases, the BER decreases accordingly. To achieve the same BER, more advanced modulation techniques need higher SNR.

Above all, we can conclude high SNR is important for communication systems. As a result, the phased array becomes an optimal choice in the 5G development down the road. Nevertheless, there are still questions to clarify and challenges to overcome, such as who does the DF, should DF be done on RF band or baseband, how can the main beam be

casted continuously on the fast-moving target, how can beamform be driven if user's device orientation changes over time, how can coherent data stream be provided (information mixed with carrier frequency; a true time delay scanning is wanted), and so on. Similarly, higher SNR provides radar system better probability of detection [3].

1.2. Volumetric Array

Volumetric array is investigated in this work because the geometry is similar to the formation of swarming unmanned aerial vehicles (UAVs). In general, most phased arrays are primarily built on planar surfaces; however, many advantages have been discovered by distributing the array elements in a 3D volume.

First, the 3D distributed array has less mutual coupling than the linear or planar array. Mutual coupling is the interaction between our antenna and other antennas, and it alters the original impedance and phase from the design value. One reason for this is the spacing between each array element can be larger, and the mutual coupling is proportional to the antenna spacing [4, 5]. Another reason for this is the transmit waves from the planar array would easily become surface waves and propagate along the planar metal surface. The metal ground plate is commonly used for linear and planar array to increase the directivity.

Second, the volumetric array maintains a constant gain, beamwidth, and beamshape through 3π scan coverage if an isotropic radiator is used [6, 7, 8]. In contrast, the planar array does have beamwidth degrades as the main beam scans away from the array broadside [7]. Likewise, the uniform planar array can only maintain symmetrical

beamshape at array broadside, but the beamshape distorts by the depth difference toward wide angles.

Third, without a doubt there are more antenna elements that can be put into a volume; therefore, the volumetric array can have more transmitting power. It may not have more received power because the received power is determined by the effective aperture of the array, which is possibly the same area as a planar array. To put more T/R modules into the radome [9], engineers have to design larger radome cross-sections, which greatly affect the aerodynamic performance of the airplane. If antennas can be displaced in a volumetric style, we can assume more T/R modules can be displaced. Therefore, more transmitting power and higher gain can be acquired.

1.3. Random Array

Random array (also known as distributed array, or aperiodic array) has the feature of array elements distributed non-uniformly or randomly. For the wireless phased array applications on mobile platforms, clearly the drones' formation is close to a random style. The random position brings the array more spatial diversity and benefits, such as lower mutual coupling, automatic sidelobe cancellation, smaller radar cross-section (RCS) [10], and so on. The specialties of the random array are described as follows.

First, the random array can have element spacing greater than a half wavelength without suffering from grating lobes in the field of view (FOV). This results in an increased directivity, better angle resolution [11], and minimal influence by the mutual coupling. The mutual coupling in uniform phased arrays causes serious scan blindness problem ($\Gamma = 1$ at certain scan angle), and it is not acceptable especially for a radar system.

The scan blindness is caused by all the element impedances that largely deviate from the design values (normally 50Ω) and change at the same rate. Then the transmitting power would totally reflect back to the radio frequency (RF) circuit and cause unexpected damages to the TX/RX front-end system.

Second, all the array elements operate at full power to provide maximum radiated power. For random array, it is more favorable to reduce the sidelobe level (SLL) by increasing the antenna elements rather than tapering the amplitude. For this reason, random array is a more efficient way to exploit the RF power; without a doubt, RF power is expensive. In contrast to the conventional SLL reduction method on uniform array, the tapered amplitudes along the array aperture make the array run in an inefficient way. The radiation efficiency significantly decreases as the array elements become larger.

Third, the uniform (periodicity) spacing is the primary factor to generate sidelobes, yet the random (aperiodic) spacing/position of the random array would effectively diminish the grating lobes and reduce the SLL. In fact, any pattern or repetition tendencies would create the sidelobes. From [8, 12], the average SLL of the random array is inversely proportional to the array elements, and is calculated as

$$P_{ave_SLL} = \frac{P_{sidelobe}}{P_{main_beam}} = \left(\frac{\sqrt{N}}{N}\right)^2 = \frac{1}{N}, \quad (4)$$

where N is the number of array elements [4]. In dB form, the ratio becomes

$$P_{ave_SLL} = 10 \log \left(\frac{1}{N}\right). \quad (5)$$

A plot in Fig. 1 shows relations between the average SLL and the array elements. For example, if array elements equal to 100, a -20 dB average SLL is expected. When array elements equal to 1000, a -30 dB average SLL is prospective.

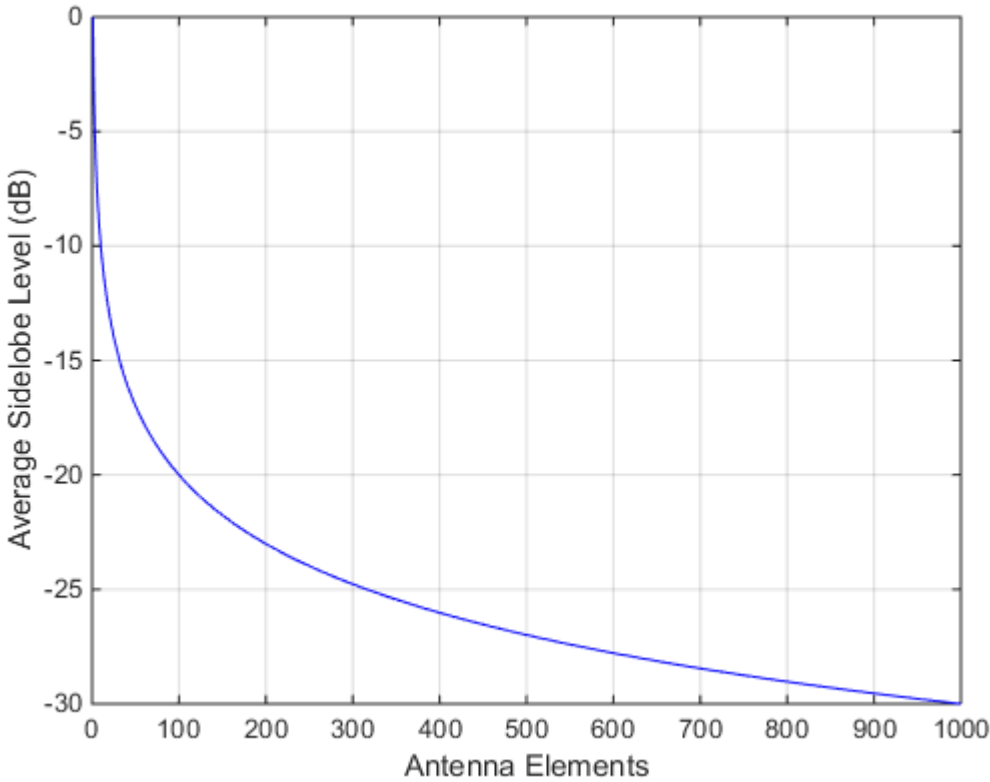


Figure 1 Average SLL vs. Antenna Elements.

1.4. Circular Polarization

Due to the essence of continuous orientation changes on mobile platforms, this dissertation involves lots of circular polarization among the projects to avoid cross-

polarization. For example, if both TX and RX adopt linear polarized systems, the orientation changes from either platform (usually the user device), causing power level fluctuations. For this reason, circular polarized topology increases the system stability and alleviates the polarization loss or polarization mismatch between the transmitter and the receiver.

The polarization is the locus of the E vector [13]. For the most part, plane waves can be categorized into linear polarization or circular polarization. A polarization mismatch factor (PMF) p is defined in [14] as $p = |\hat{e}^i \cdot \hat{h}^*|^2$, where \hat{e}^i is the complex unit vector accounting for the incident wave, and \hat{h} is the complex unit vector of the receiving antenna vector effective length. The p ranges from 0 to 1 for cross-polarized and co-polarized cases, respectively. For co-polarized cases [15], both right hand circular polarization (RHCP) and vertical polarized antennas have 0 dB polarization loss. For cross-polarized cases, both RHCP and vertical polarized antennas have more than 25 dB polarization loss.

Besides increasing the system stability, there are other favorable reasons to embrace circular polarization. For radar detection, it is reported that a double bounce circular polarization radar can reach 20 to 30 dB higher SNR than the linear polarized in moderate to heavy rain conditions [16]. Rain clutters are effectively filtered out in this case. It is also reported in [17] that the RCS response heavily depends on the polarization of incident waves, and E-wave (TE polarization) or circular polarized waves are recommended for radar detection. A circular polarized beam can have average RCS of the target. The shape of the stealth fighter normally reduced the RCS for certain polarization,

so the circular polarization waves would be expected to derive higher return signals (RCS) than the linear polarized waves.

1.5. Wireless Phased Arrays on Mobile Platforms

With the emerge of drones, quadcopters, and UAVs, some traditional applications transformed to mobile platforms become a fresh topic. Mobile platforms do not limit themselves to the drones, but they can be extended to the use of traditional carriers, such as constellations of satellites, group of cars, fleets of ships, and so on. The major difference compared to the fixed platform is the array element maneuverability. Position shifts or orientation (yaw, pitch, and roll) can change over time. Mobile platform applications have tremendous advantages over the fixed platform in some ways. One well-known feature is the maneuverability. For some extreme cases like the disaster rescue, the fast deployment, easy of driving, and high agility features make it become an outstanding candidate to fulfill the works. In the same way, there are many potential capabilities that can be exploited on the mobile platforms, such as communication, remote sensing, searching, cargo, mapping/GIS, and so on. In this dissertation, our goal was to take advantage of the mobile platform maneuverability and realize a wireless phased array application on it. Fig. 2 gives an imaginary idea of a wireless phased array beamforming system implemented by drones.

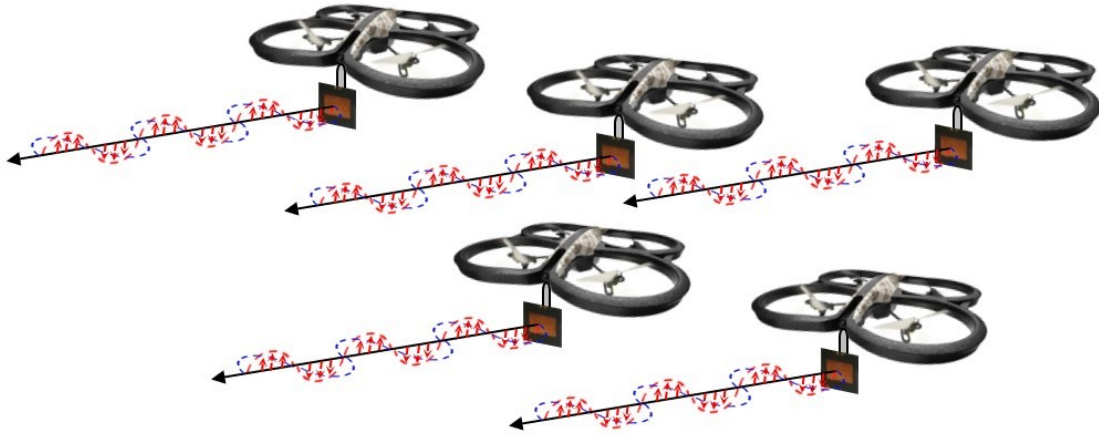


Figure 2 A wireless phased array beamforming system carried out by drones.

To successfully realize the idea depicted in Fig. 2, there are some challenges that need to be solved. The first is the wireless phase synchronization, and not only the frequency [18] but also the phases should be synchronized. The second challenge is to know the relative position location and global position orientation of each array element, which can be acquired by visual camera (for indoor), global positioning system (GPS), or inertial measurement unit (IMU) sensors. The last is to develop collaborative beamforming algorithms, which is the major contribution of this dissertation. The solutions to solve the array element maneuverability and create the corresponding beamforming algorithm are provided in this work, but the wireless phase synchronization is not covered.

1.6. Wireless Phase Synchronization

Although the wireless phase synchronization is not covered in this work, it is worthwhile to offer detail explanations addressing why this matter is difficult to deal with. Clearly, the local oscillator (LO) signal plays an important role in the modern microwave system. It is used to upconvert, downconvert or even act as the transmit continuous wave (CW) source. One thing needed to be clarified beforehand, the phase synchronization means the LO signal to each antenna has not only the same frequency but also the same phase.

For wired phased arrays with central-fed LO topology, the frequency is fixed because they all come from the same voltage-controlled oscillator (VCO). The signals distributed to the end array element may have phase discrepancies that come from the non-equal length of the transmission lines. The phase difference can be examined from the vector network analyzer (VNA) and compensated by the phase shifter. Ideally, the calibration process is only needed to be done once, and all the sub-channels should have equal phases thereafter.

On the other hand, for wireless phased arrays with central-fed LO topology, the LO signals are delivered by broadcasting wirelessly. The LO signals arrive at each element through the free space air medium, and therefore the phase can vary from 0° to 360° . Unlike the wired phased arrays, the phase from the wireless phased array changes over time, and errors from multipath or shadowing cannot be ignored.

In contrast, the wireless phased array with distributed LO topology has its own VCO for an individual array element. One common way to fix the frequency is to adopt

the phase locked loop (PLL); however, the PLL can only guarantee the LO signal is stable with low phase noise; it has nothing to do with the phases. To make every LOs have the same phase, a common method is to use a feedback system. In [19], a node is designated as the master and broadcasts a sinusoidal reference signal to the slaves. The spacing from the master node to the slave node creates a phase delay. When the slaves return the shifted signal back, the master node analyzes and estimates the phase shifting from the channel. Providing this information back to the slaves, the master node helps the slaves adjust their oscillator accordingly. A different approach reported in [20] that all slaves transmit a broadband sequence to the master. Then the master bounces back the complex conjugate of the received signal. The slaves should be able to tell the phase difference to the master's LO. As the slave does the calculations by itself, the computational burden is distributed evenly among the slaves. After all, these solutions mentioned above all take system resources and processing time to figure out the phase difference between the slave and the master. For low latency applications or large distributed elements, a more efficient and real-time solution is interested.

2. AN INVESTIGATION OF BEAMFORMING USING DISSIMILAR ANTENNAS IN VOLUMETRIC RANDOM ARRAYS

2.1. Introduction

Beamforming using phased arrays on mobile platforms has been a topic of discussion for many years. Mobile platforms can be UAVs with an embedded antenna flying in the air. One critical problem of mobile platform beamforming is collaboratively and correctly steering the main beam to the target angle. The major difference compared to the fixed platform is the array element maneuverability. The movement includes position shifts or orientation changes. Therefore, a circular polarization radiation pattern is preferable to mitigate the polarization loss for the mobile platform application. To examine the characteristics of the phased array on mobile platforms, it is necessary to evaluate the performance of the volumetric random array first.

The volumetric random array has features of 360° radiation coverage in both azimuth and elevation planes. The aperiodic spacing of each array element can effectively diminish the grating lobes and reduce the SLL [21, 22]. It is reported by [23] that an array with uniform spatial density distribution within a sphere has a SLL of -20.6 dB, which is lower than the uniform planar array (-13.5 dB SLL). In addition, the beamwidth of the main beam can stay constant through the entire scan angle [6], and the beamwidth for linear or planar arrays becomes broader when scanned toward the endfire direction [7].

Moreover, the volumetric random array can have element spacing greater than a half wavelength without suffering from the grating lobe problem. Increasing the element

spacing alleviates the mutual coupling effects [4]. The mutual coupling will cause phase variations especially for the edge elements at wide angles.

The array in this work is composed of sixteen horizontal polarized patch antennas and sixteen vertical polarized monopole antennas. The patches are used to represent platforms with directional radiation properties and the monopoles are intended to represent platforms with omnidirectional radiation properties. The patch sub-array works collaboratively with the monopole sub-array to create a maximum RHCP radiation pattern. The thirty-two antenna elements are randomly placed in a spherical volume of a 380-mm radius. The whole experiment is operated at 2.46 GHz to evaluate the array performance. A simulation model (in Fig. 3) is constructed in the HFSS to help develop the beamforming algorithm.

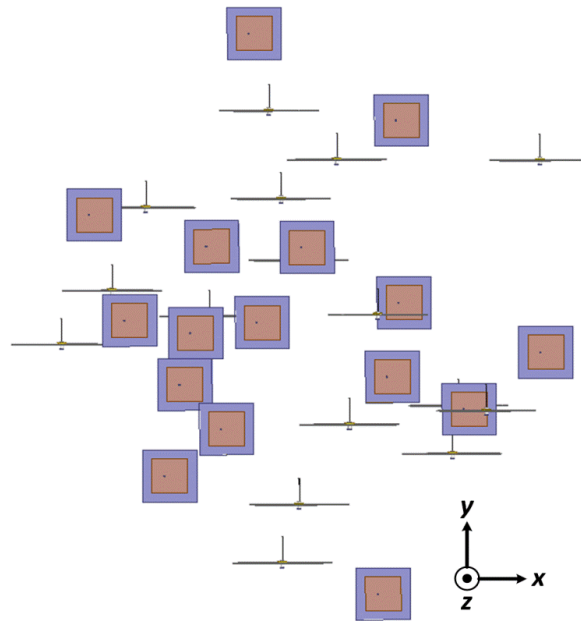


Figure 3 The simulated volumetric random array modeled in the HFSS.

2.2. Antennas

2.2.1. Microstrip Patch

The microstrip patch antenna built on the Duroid 5880 substrate contains three layers, which are the patch radiator, a dielectric layer, and the copper ground plane. The square patch gives a maximum bandwidth [24] and has dimensions of a width of $w = 40$ mm and a resonant length of $L = 39.6$ mm; the antenna reference point (ARP) is defined at the center of the patch plate. The substrate has a dielectric constant of 2.2 and thickness of 1.57 mm; the ground plane has dimensions of a width of 60 mm and a length of 60 mm. The probe feed is directly coupled with the patch and has a distance of 13.6 mm from the patch edge. The antenna has 21.66 dB return loss and 7.17 dB gain at 2.46 GHz. Besides, the half-power beamwidth (HPBW) of HP_{θ} is 83° . Fig. 4 shows the simulated input impedance and voltage standing wave ratio (VSWR) of the patch antenna from 2 to 3 GHz. Fig. 5 shows the simulated radiation pattern for the two-elevation cut-planes at 2.46 GHz.

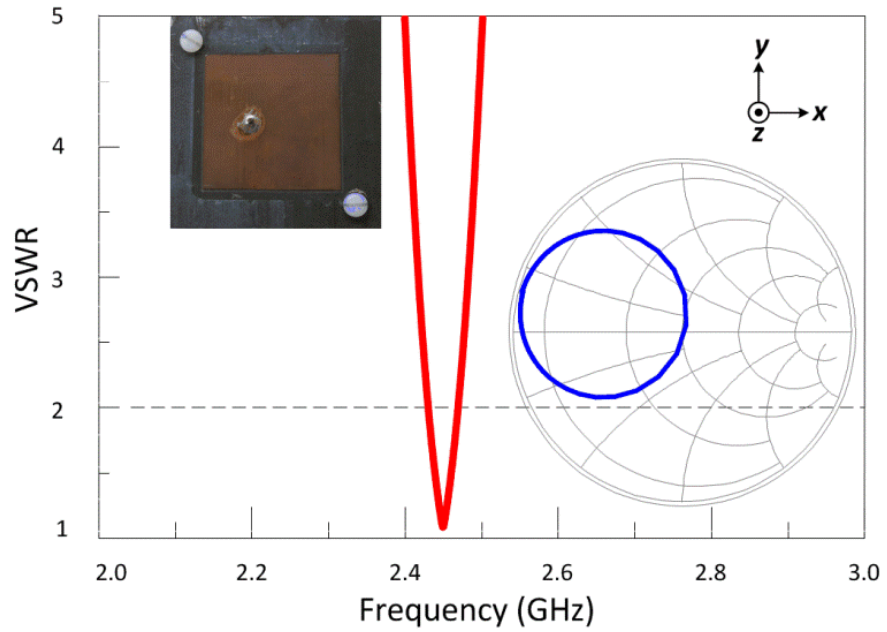


Figure 4 Simulated VSWR and Smith chart (overlaid) of the microstrip patch.

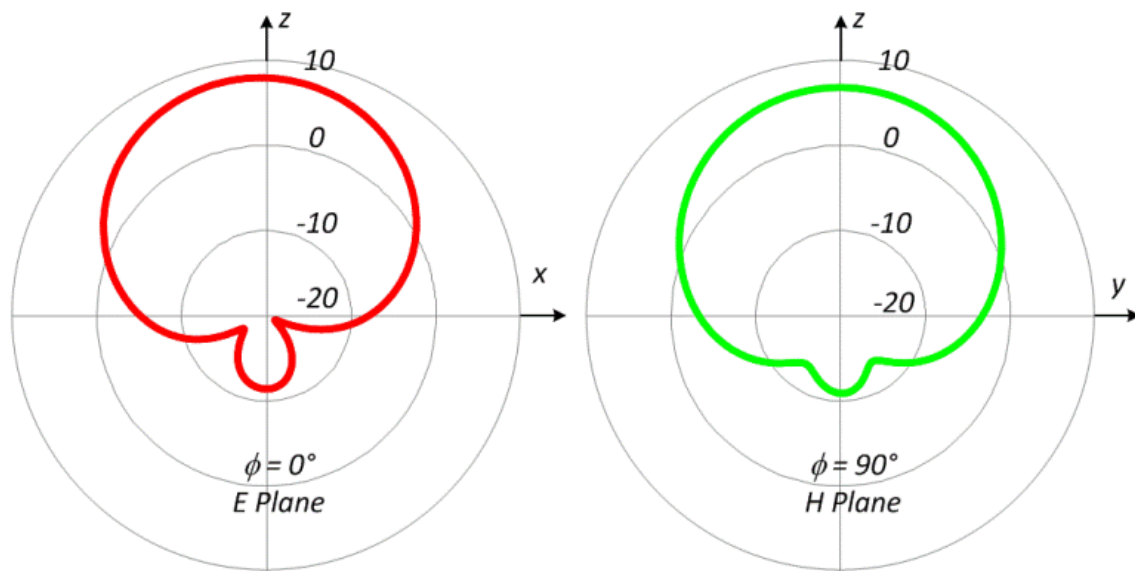


Figure 5 Simulated radiation pattern (dB) of the microstrip patch.

2.2.2. Monopole

The quarter-wavelength monopole has wire length of 30 mm, which is mounted above an aluminum ground plane of 40 mm in radius. The ARP is defined at the center of the aluminum plate. The monopole has a return loss of 21.99 dB and a gain of 1.41 dB at 2.46 GHz. Fig. 6 shows the simulated input impedance and VSWR of the monopole antenna from 2 to 3 GHz. Fig. 7 gives the simulated radiation pattern for the two-elevation cut-planes at 2.46 GHz.

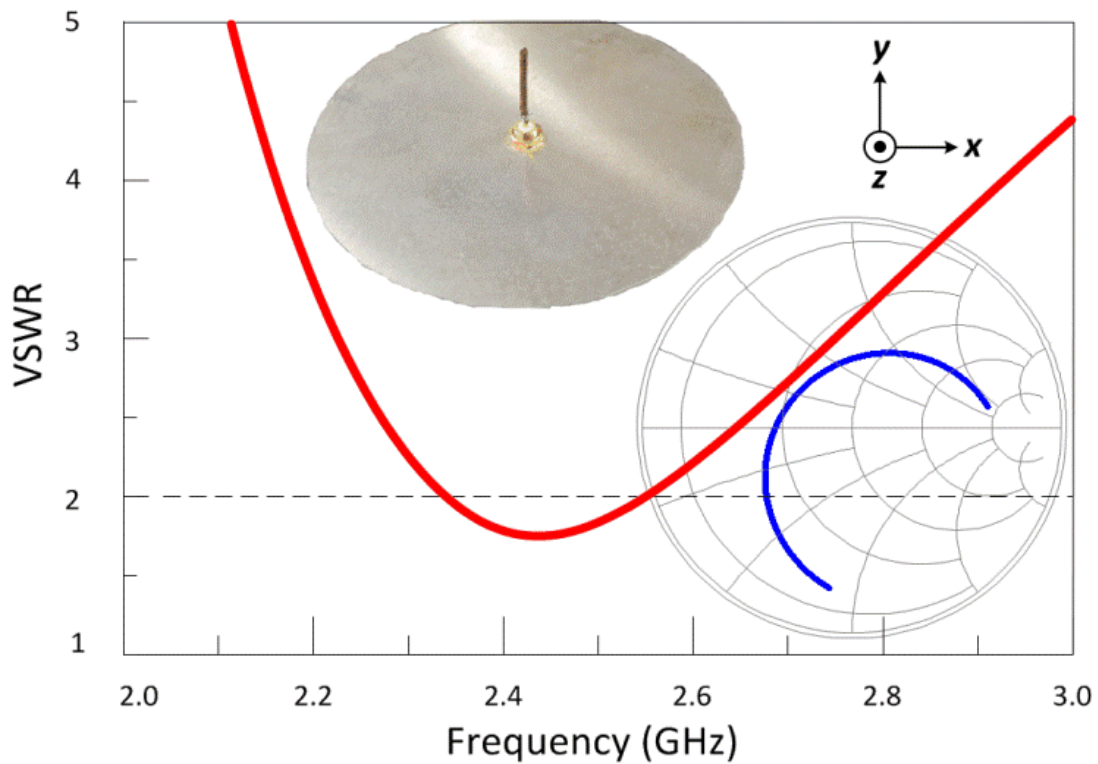


Figure 6 Simulated VSWR and Smith chart (overlaid) of the monopole.

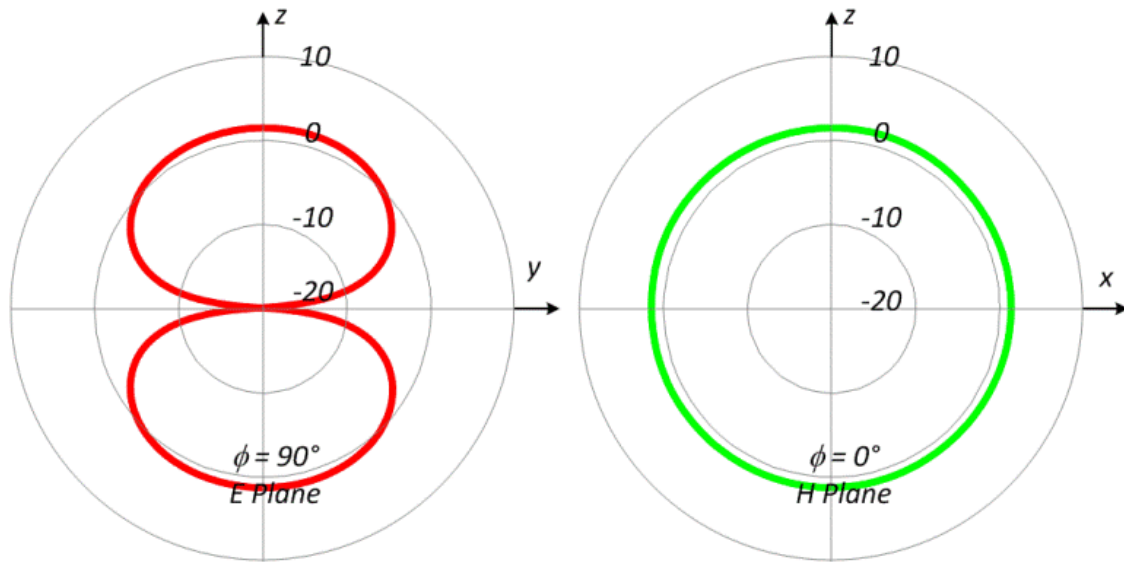


Figure 7 Simulated radiation pattern (dB) of the monopole.

2.2.3. Phase Center Estimation

The phase center is the origin of the spherical wave radiated from the antenna and hence phases on the radiated spherical wave in the far-field are supposed to be constant. DF applications, which use phase difference to determine the direction-of-arrival (DOA), rely heavily on the phase accuracy. The phases deviate from the ARP and would be estimated and added to correctly drive the main beam.

A method uses the actual phase front to derive the locus of the real phase center that it is developed in [25]. This method is used in this experiment to estimate the phase deviation from the ARP. The phase variation would only be evaluated from -45° to 45° , and the variation from the wide angles are neglected. In fact, the phase variation from the wide angles is much higher; however, the majority of the applications provide service

from -45° to 45° . The resulting phase center of the patch antenna is observed 1 mm (0.008λ at 2.46 GHz) from the ARP, and the location is 1 mm above the patch surface. On the other hand, the monopole phase center is 22 mm (0.17λ at 2.46 GHz) from the ARP, and the location is on the wire axis and 22 mm above the aluminum plate. Both results are obtained from the simulated radiation patterns modeled in the HFSS.

The phase variations of both antennas are given in Figs. 8 and 9, respectively. When moving the ARP from both antennas to the phase center, the patch and monopole antennas have maximum peak to peak phase variations of 2.59° and 6.27° , respectively.

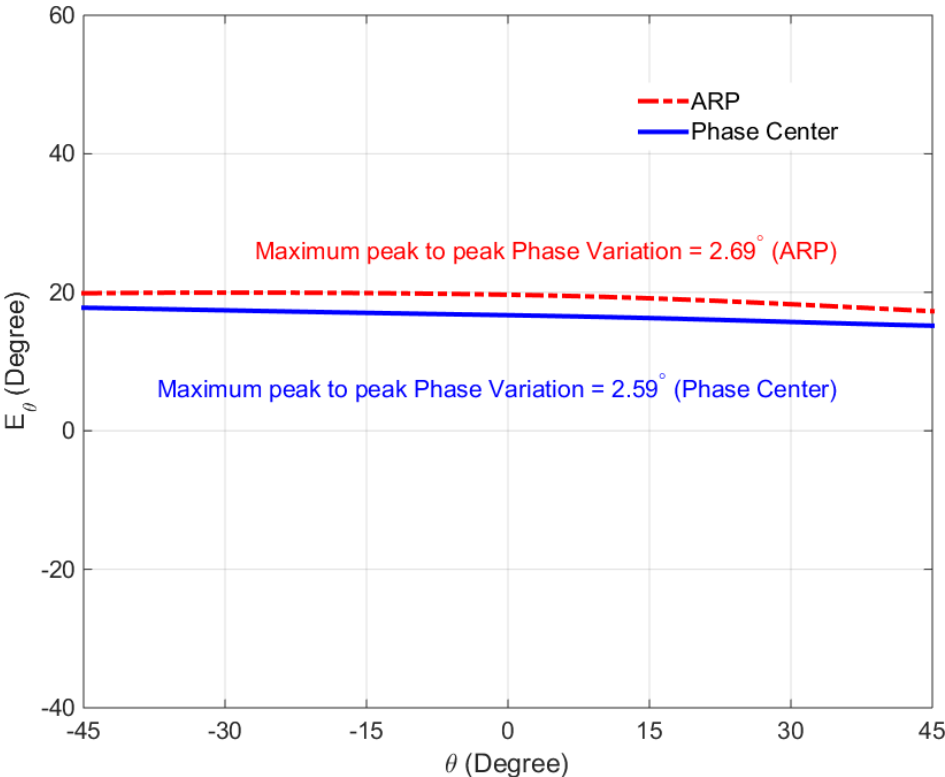


Figure 8 Phase variation of the patch antenna with $\phi = 0^\circ$ and θ scans from -45° to 45° .

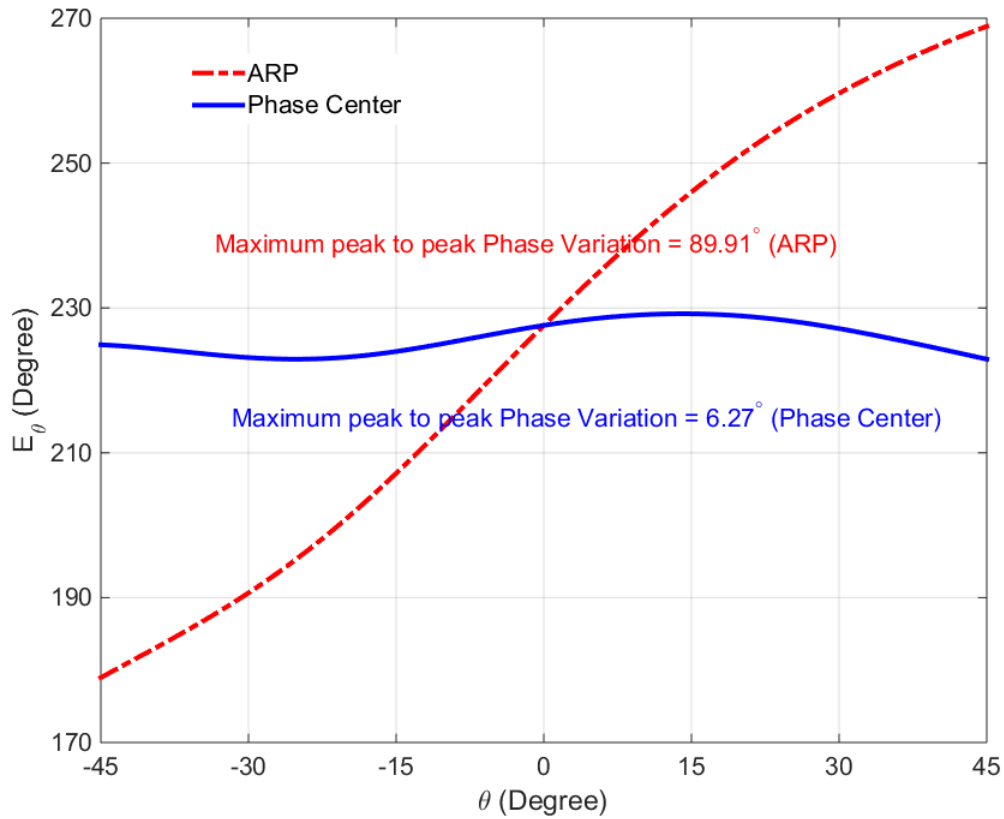


Figure 9 Phase variation of the monopole antenna with $\phi = 90^\circ$ and θ scans from -45° to 45° .

2.3. Array

One major task in this experiment is to successfully beamform the array with a RHCP radiation pattern. A RHCP radiation pattern is achieved by adjusting the phases of each array element. To successfully drive the main beam, step by step procedures have to be built up to correctly calculate the corresponding phases from each stage. All these procedures are elaborated upon in the following section.

2.3.1. Distance Phase from the Scan Angle

To drive the main beam to scan angle (θ, ϕ) , phase differences from the observation point $R(r, \theta, \phi)$ to each antenna element needed to be calculated. The locations of the thirty-two array elements are designated as $P_n(x_n, y_n, z_n)$, where $n = 1 \dots 32$. In the far-field, the $\overline{P_n R}$ is approximately parallel to \overline{OR} , where O is the origin. The phase difference from each array element dominates the total array performance; however, the magnitude differences change with a factor of $1/r$, which is insignificant in this work.

A method using matrix multiplication is designed to easily calculate the offset distances. The T is the transform matrix. The P matrix is the location of the thirty-two array elements. The D matrix is the results of the offset distance. Casting these in matrix form gives

$$D = PT, \quad (6)$$

where

$$P = \begin{bmatrix} x_1 & y_1 & z_1 \\ x_2 & y_2 & z_2 \\ \vdots & \vdots & \vdots \\ x_n & y_n & z_n \end{bmatrix}, T = \begin{bmatrix} R \sin \theta \cos \phi \\ R \sin \theta \sin \phi \\ R \cos \theta \end{bmatrix}, \text{ and}$$

$$D = \begin{bmatrix} R \sin \theta \cos \phi \cdot x_1 + R \sin \theta \sin \phi \cdot y_1 + R \cos \theta \cdot z_1 \\ R \sin \theta \cos \phi \cdot x_2 + R \sin \theta \sin \phi \cdot y_2 + R \cos \theta \cdot z_2 \\ \vdots \\ R \sin \theta \cos \phi \cdot x_n + R \sin \theta \sin \phi \cdot y_n + R \cos \theta \cdot z_n \end{bmatrix}.$$

Once the offset distances are calculated, the corresponding distance phases for each array element can be calculated. Up to this point, each array element should contribute an equal phase along the scan angle.

2.3.2. Rotation Phase - RHCP

The volumetric random array has two sub-arrays, which are patch and monopole sub-array, respectively. For illustration purposes, numbers 1 to 16 ($q = 1 \dots 16$) are assigned to monopole antennas, and numbers 17 to 32 ($p = 17 \dots 32$) are assigned to microstrip patch antennas. Theoretically, a RHCP wave equation should have the form as follows [26]

$$\bar{E}(z) = \hat{x} \sum_{p=17}^{32} a_{x_p} e^{-jkz} + \hat{y} \sum_{q=1}^{16} a_{y_q} e^{j-90^\circ} e^{-jkz}, \quad (7)$$

where a_{x_p} and a_{y_q} are the amplitudes of the patch and monopole elements, respectively. After transforming from Cartesian to spherical coordinate systems, the original electric field equations decomposed into two spherical components (in the far-field, suppressing the radial \hat{R} term), which are

$$\bar{E}_\theta = \sum_{p=17}^{32} a_{x_p} e^{-jkR\cos\theta} \cos\theta \cos\phi + \sum_{q=1}^{16} a_{y_q} e^{j-90^\circ} e^{-jkR\cos\theta} \cos\theta \sin\phi, \text{ and} \quad (8)$$

$$\bar{E}_\phi = \sum_{p=17}^{32} -a_{x_p} e^{-jkR\cos\theta} \sin\phi + \sum_{q=1}^{16} a_{y_q} e^{j-90^\circ} e^{-jkR\cos\theta} \cos\phi. \quad (9)$$

To simplify the calculation procedures, it is important to drive the main beam to the broadside, where scan angle $\theta_s = (0^\circ, 0^\circ)$. After that, it is clear the E_θ field is primary from the contribution of the microstrip patch subarray; the E_ϕ field is primary from the monopole subarray. To successfully create a RHCP radiation pattern, a 90° phase delay is necessary to apply on all monopole subarray.

2.3.3. Amplitude Equalization

Because of the high gain feature of the microstrip patch antenna, obviously, the amplitude contribution from the patch sub-array and the monopole sub-array are unequal. As a result, additional attenuation has to apply on the patch sub-array to equalize the

amplitude. An empirically-derived attenuation of 8.7 dB is then added to the patch subarray to equalize the amplitudes of the E_θ and E_ϕ components. Once the amplitudes from both sub-arrays are equal, a maximum RHCP gain and a minimum left hand circular polarization (LHCP) gain is expected. This step is very crucial to get a maximum RHCP gain in this case.

2.4. Experiment

2.4.1. Anechoic Chamber

The radiation pattern of the thirty-two-element volumetric random array is demonstrated by measurement in the anechoic chamber (located at the Electromagnetics and Microwave Laboratory, Department of Electrical and Computer Engineering, Texas A&M University) to reduce interferences from multipath and simulating the free space environment.

The origin of the testing array is well aligned with the turning table in the chamber to minimize pattern distortion. The coordinate system has the same arrangement as the simulation setup (in Fig. 3), and therefore, the measured results could be used to compare with the simulated data directly without extra data transformation. The pedestal is designed to rotate on the x-z plane (θ from -180° to 180°). Furthermore, the quad-ridged guide horn antenna is used as the receiver, which can measure both horizontal and vertical fields at the same time.

2.4.2. Simulation Testing

The volumetric random array is modeled and simulated in the HFSS to estimate

the radiation characteristics. The locations of the thirty-two elements are chosen randomly within the sphere of a 380-mm radius. The simulation is run at scan angle θ_s set to $(0^\circ, 0^\circ)$ and amplitudes are equally excited. Next, an 8.7 dBm attenuator is added to the patch sub-array so that two sub-arrays have equal E_θ and E_ϕ amplitude.

The goals of this testing were to find the maximum RHCP gain and the minimum LHCP gain at the scan angle $(0^\circ, 0^\circ)$. The exported results of this testing are combined with the measurement to make a comparison.

2.4.3. Integrated Array System Hardware

Fig. 10 shows a block diagram of the thirty-two-element volumetric random array. The array is operated by entering the desired scan angle into the smart phone interface. The calculated phases for each array element are then wirelessly transmitted to the control board. The board accordingly generates corresponding DC bias voltages to drive the phase shifters. A fourth-order polynomial curve is developed in [27] to map the applied voltage to the corresponding phases. The hardware used to build the system is primarily from the COTS products, which are usually designed to have a characteristic impedance of 50Ω .

The signals out of the VNA are equally divided into thirty-two sub-channels by a 32-way Wilkinson power divider. Additional 8.7 dB attenuators are also added to the patch sub-array channels, so that the E_θ and E_ϕ have the same amplitude.

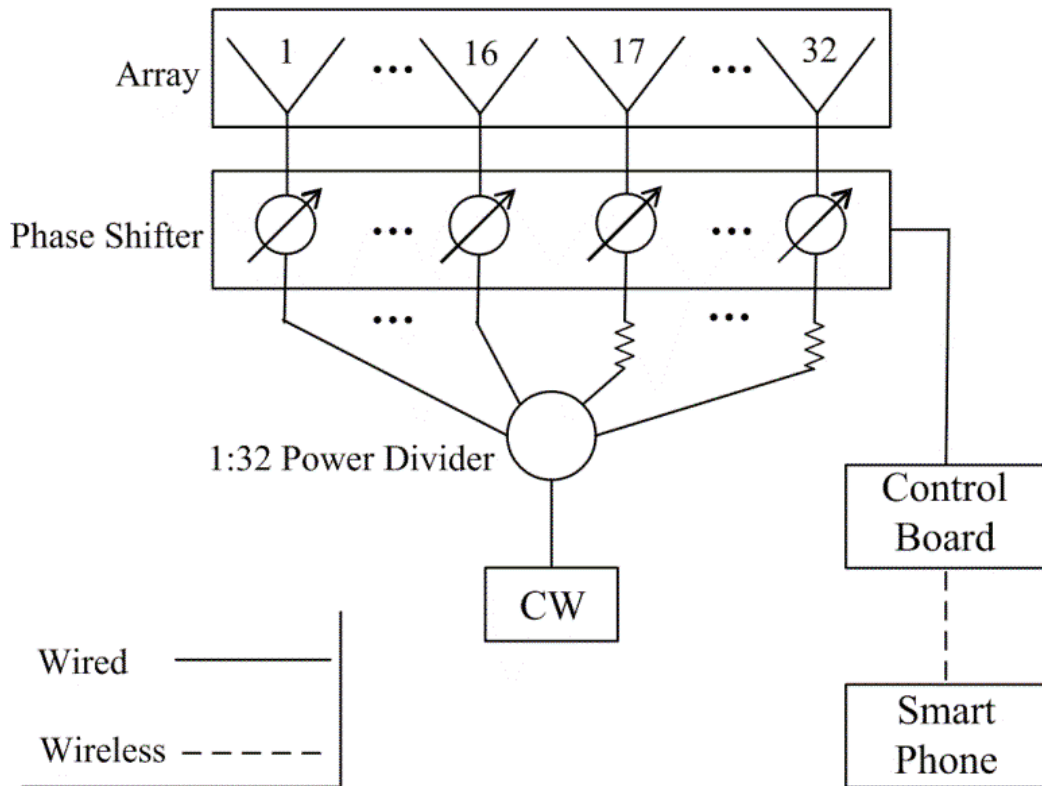


Figure 10 Structure of the thirty-two-element volumetric random array beamformer.

Fig. 11 displays a thirty-two-element volumetric random array tested in the anechoic chamber. The testing is completed by rotating the θ from -180° to 180° with ϕ equal to 0° and measured by the vertical (G_ϕ) and horizontal (G_θ) power. The supporting sticks are made of wood to minimize the scattering and alleviate the electromagnetism shielding effects. A minor shadowing effect [28] that comes from the coaxial cables is inevitable and can be accepted.

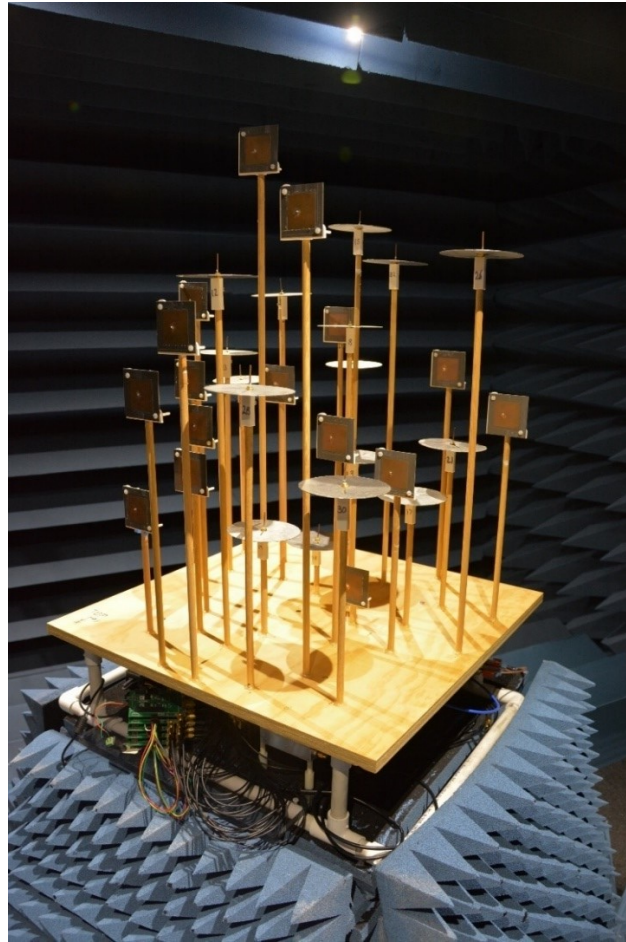


Figure 11 The thirty-two-element volumetric random array was placed in the anechoic chamber.

2.4.4. 90° Hybrid Coupler

The 90° hybrid coupler is commonly used to divide the signals with an equal power split, causing one channel to have a path length of 90° longer than the other. Here the 90° hybrid coupler is used to collect power from vertical and horizontal directions and

transform to the RHCP and LHCP gains by using the 90° phase delay property. The coupler connection diagram is shown in Fig. 12 for a better understanding.

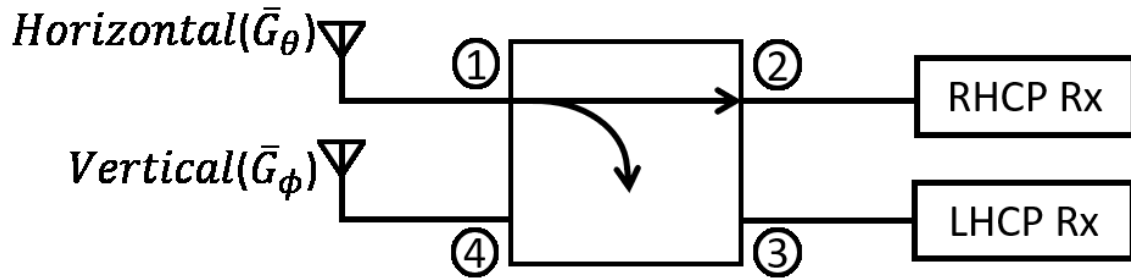


Figure 12 Signal in and out of the symmetric four-port coupler.

Without any modification, the received horn antenna in the anechoic chamber can only provide vertical and horizontal gain measurements. Instead of the vertical (G_θ) and horizontal (G_ϕ) gain measurements, the RHCP and LHCP gains are our interests in this work. Therefore, a four-port 90° hybrid coupler is used to connect the horn antenna to transform the vertical (G_θ) and horizontal (G_ϕ) gains into the RHCP and LHCP gains. A photograph taken in the chamber is shown in Fig. 13.

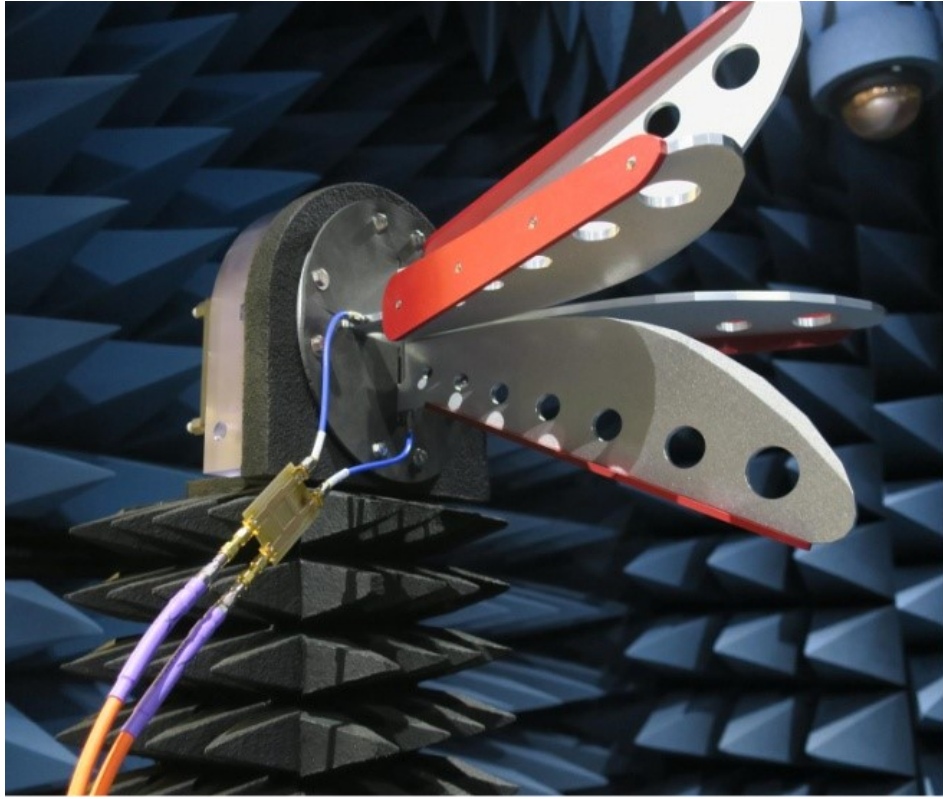


Figure 13 Photograph of the coupler connects with the receiver in the chamber.

The S parameter (at 2.46 GHz) of the symmetrical four-port 90° hybrid coupler is measured and has the values of

$$[S] = \begin{bmatrix} 0 & 0.41e^{j106.46^\circ} & 0.38e^{j17.97^\circ} & 0 \\ 0.41e^{j106.46^\circ} & 0 & 0 & 0.38e^{j17.97^\circ} \\ 0.38e^{j17.97^\circ} & 0 & 0 & 0.41e^{j106.46^\circ} \\ 0 & 0.38e^{j17.97^\circ} & 0.41e^{j106.46^\circ} & 0 \end{bmatrix}$$

Note that the signal at port #2 is from the summation of port #1 and #4, where the signal from port #4 has an additional path length of 88.49° longer than port #1. Thus, the horizontal signals (G_0) leads the vertical signals (G_θ) by 88.49°, which is the RHCP gain.

On the other hand, the signal at port #3 is the summation of port #1 and #4, where the signal from port #1 has an additional phase delay of 88.49° ($\angle S_{34} - \angle S_{31} = 88.49^\circ$) longer than port #4. Thus, the vertical signals (G_ϕ) leads the horizontal signals (G_θ) by 88.49° , which is the LHCP gain.

2.5. Results

Before evaluating the whole array system, we need to know the amplitude contribution from each sub-array. The first experiment measures the gains of G_θ and G_ϕ and the results are shown in Figs. 14 and 15, respectively.

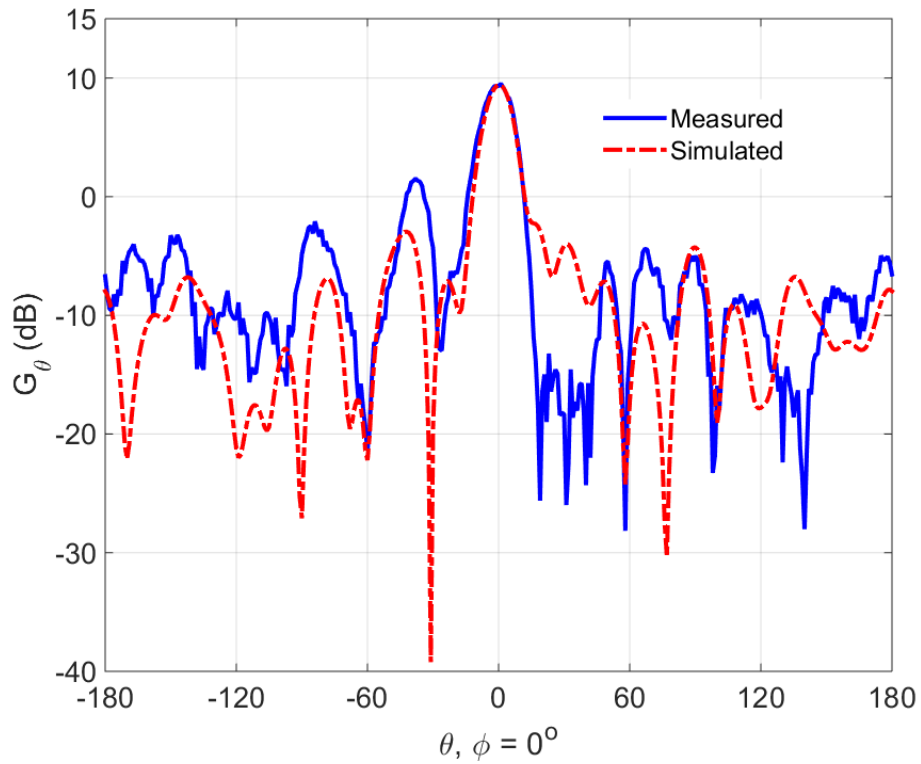


Figure 14 Comparison of measured and simulated G_θ pattern.

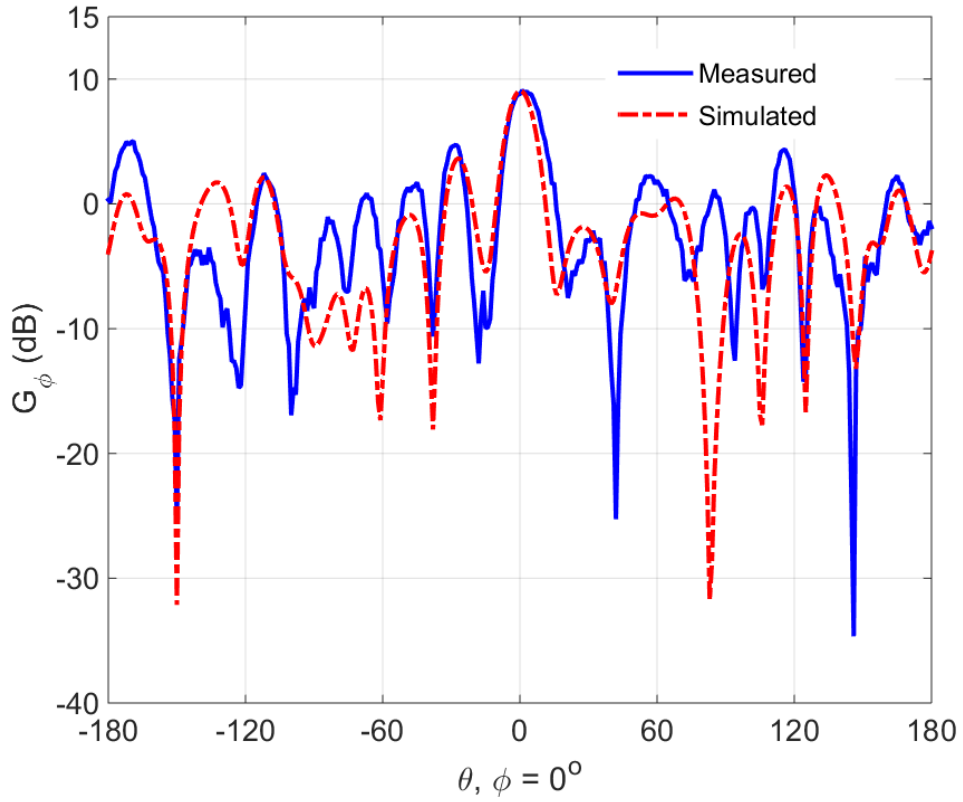


Figure 15 Comparison of measured and simulated G_ϕ pattern.

Each measured gain is normalized, and it is combined with the simulated one for comparison. Keep in mind that an 8.7 dB attenuator is already added on the patch sub-array, and the results show the maximum G_θ and G_ϕ , which are both around 9 dB at array broadside. This experiment makes sure that both the contributions from the patch sub-array and monopole sub-array are equal. From the system's point of view, a high RHCP gain is required; therefore, making sure both G_θ and G_ϕ have an equal amplitude is essential. For both sub-arrays, we observe no grating lobes in the FOV.

The second measurements shown in Figs. 16 and 17 are the G_{RHCP} and G_{LHCP} from both measured and simulated results. The measured gains are normalized to make a better comparison with the simulated data.

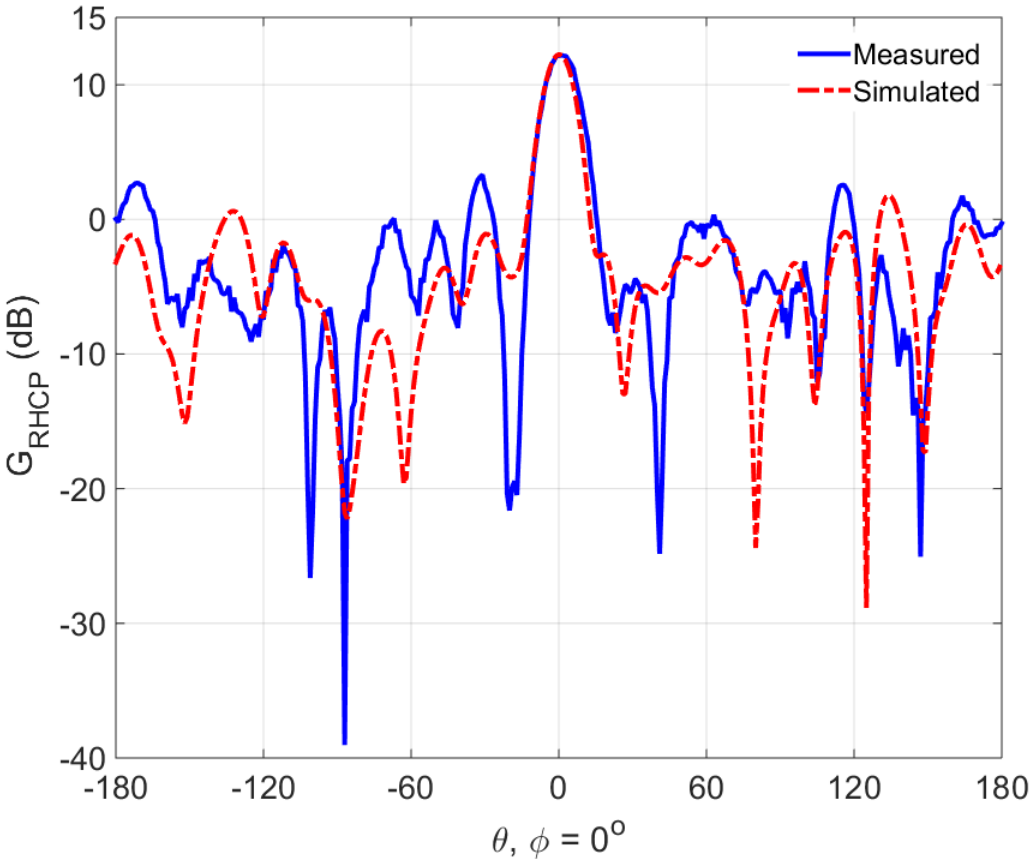


Figure 16 Comparison of measured and simulated G_{RHCP} pattern.

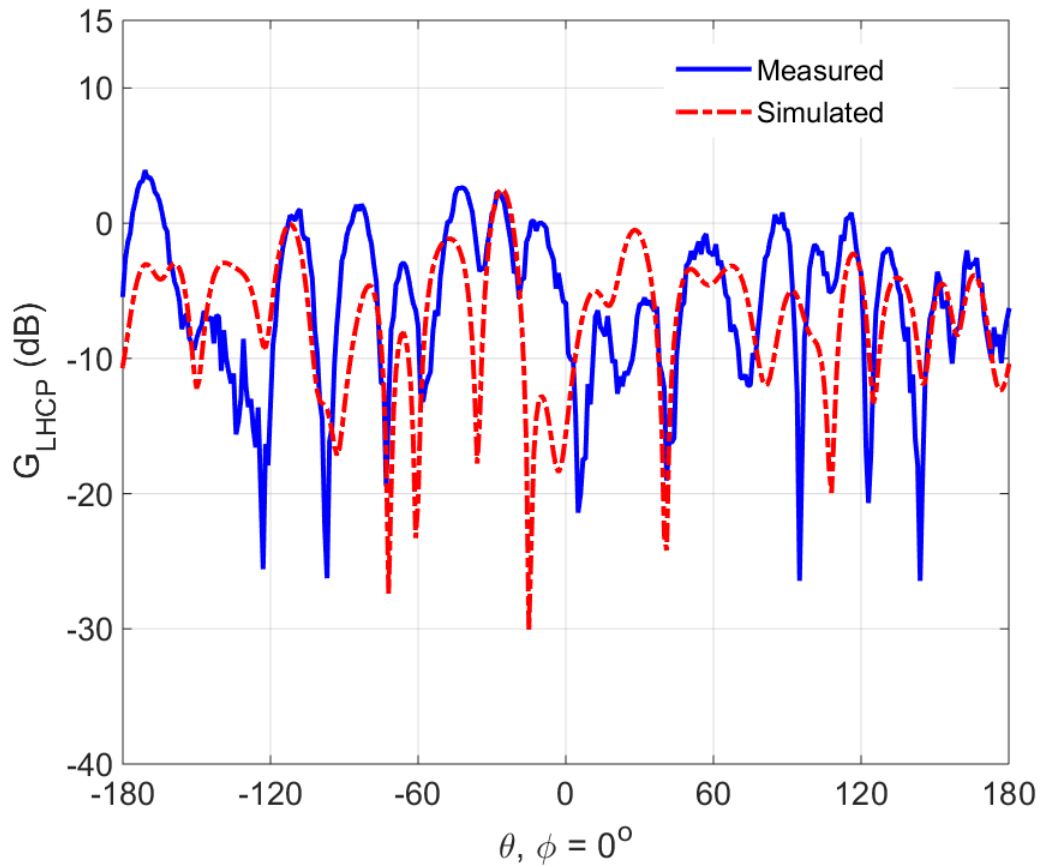


Figure 17 Comparison of measured and simulated G_{LHCP} pattern.

For measured results, the maximum G_{RHCP} is 12.25 dB, and the minimum G_{LHCP} is -5.84 dB. There is an 18.09 dB polarization loss between the RHCP and the LHCP gains. For a thirty-two-element volumetric random array, the measured SLL_{RHCP} is -8.95 dB. For simulated results, the maximum G_{RHCP} is 12.25 dB, and the minimum G_{LHCP} is -15.56 dB. There is a 27.81 dB polarization loss between the RHCP and the LHCP gains; a -10.46 dB SLL_{RHCP} is obtained. The G_{LHCP} is higher than expected values because the hybrid coupler

is not a perfect 90° (88.49° coupler is used in this work). There is no grating lobe observed in either the G_{RHCP} and G_{LHCP} pattern. Other parameters are summarized in Table 1.

Table 1 - Properties of the Radiation Pattern

	Measured	Simulated
G_θ	9.42 dB	9.42 dB
G_ϕ	8.79 dB	8.95 dB
G_{RHCP}	12.25 dB	12.25 dB
G_{LHCP}	-5.84 dB	-15.56 dB
SLL_θ	-7.89 dB	-12.36 dB
SLL_ϕ	-3.8 dB	-5.41 dB
SLL_{RHCP}	-8.95 dB	-10.46 dB
$HPBW_\theta$	15°	14°
$HPBW_\phi$	15°	12°
$HPBW_{RHCP}$	15°	13°

In general, the measured results are in accordance with the simulated ones. The difference majorly comes from the alignment of the microstrip patch (not exactly facing the Z-axis) and the shadowing from the coaxial cables, which is not modeled in the simulation. The test array, contributing to some pattern distortions, is not displaced in the far-field, and the pattern has worse results at wide angles. Others miscellaneous factors, such as the antenna fabrication precision, distortion of the antenna surface (especially the

monopole aluminum ground plane), or phase variation caused by temperature, are very minor and can be ignored.

2.6. Conclusion

2.6.1. Discussion

This project successfully demonstrates beamforming by using two kinds of dissimilar antennas to create a RHCP radiation pattern. The characteristics of the microstrip patch, monopoles and volumetric random arrays are evaluated, respectively. Simulations and measurements of the volumetric random array are provided and comparisons are made to benchmark their performance with theoretical expectations.

2.6.2. Summary

Since there are no grating lobes observed within the visible region, it confirms that the volumetric random array can have spacing greater than a half wavelength without having grating-lobe problems. The measured SLL of RHCP is around 8.95 dB, which is still too high for real communication application. The main reason comes from the small array elements; therefore, we are eager to acquire a further SLL reduction method. Methods like amplitude tapering can help further reduce the SLL around the main beam, especially for a small number of array elements. Furthermore, this method is designed to drive the main beam at the design angle ($\theta = \phi = 0^\circ$). When driving the main beam away from the design angle, the phase errors will increase. The phase errors are proportional to the angles away from the $(\theta, \phi) = (0^\circ, 0^\circ)$. For future work, it is necessary to create another beamforming algorithm to drive the main beam away from the array broadside.

3. CIRCULAR POLARIZED BEAMFORMING ON VOLUMETRIC RANDOM ARRAYS WITH ARBITRARILY ORIENTED ARRAY ELEMENTS

3.1. Introduction

Based on the suggestion from “An Investigation of Beamforming Using Dissimilar Antennas in Volumetric Random Arrays” concluded at the end of chapter 2, a beamforming algorithm developed to drive the main beam away from $(\theta, \phi) = (0^\circ, 0^\circ)$ with RHCP is needed. In this project, a more general beamforming algorithm not only provides RHCP waves but also extends the antenna directions from uniform alignment to arbitrary orientation.

The phased array has been used on high performance applications, such as radar or communication systems, for many years. Using the phased array on mobile platforms becomes an ongoing interest. Mobile platforms may be swarms of UAVs, fleets of ships, or constellations of satellites. The major difference between fixed platforms and mobile ones is the array element maneuverability. The movements of the array element include position shifts or orientation (yaw, pitch, and roll) tilts over time.

To realize the mobile phased array application, there are some challenges need to overcome, such as the wireless phase synchronization, relative location of array elements, beamforming algorithms. Although many techniques need to be established, this project primarily focuses on beamforming algorithm development.

When considering the characteristics of the mobile platform criteria, the volumetric random array becomes a proper candidate in this work and therefore needs to

be further investigated. In this work, the array is demonstrated by sixteen patch antennas randomly located in a volume. Fig. 18 shows a reconfigurable phased array, which is named “Medusa.” One special feature of the Medusa platform is the position and orientation reconfigurability for each array element. The whole system uses COTS components to lower the expenses, and it operates at 2.4 GHz. Each patch antenna has a degree of freedom to rotate along the coordinate axis. The rotation capability is used to replicate the real mobile platform dynamic environment. Moreover, a spatial recognition system [29] also needs to be involved to correctly acquire XYZ positions of each array element. Next, the array is designed to provide a RHCP radiation pattern to alleviate the polarization loss from the mobile platforms. According to [16], the double bounce circular polarization radar can have 20 to 30 dB higher SNR than the linear polarized in moderate to heavy rain conditions. As a result, the circular polarized beamforming can have more resistibility against rain clutter than the linear polarized.

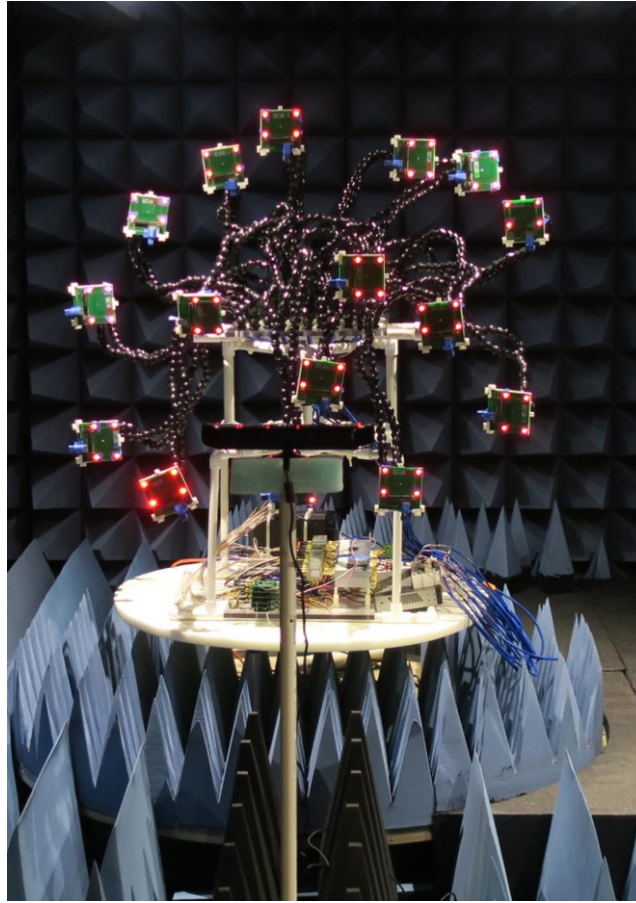


Figure 18 The photograph of the Medusa platform placed on the pedestal in the anechoic chamber.

On the other hand, the reasons to adopt the volumetric random array in this experiment, rather than the conventional uniform planar array, need to be addressed more. The uniform planar phased array does suffer gain reduction as the main beam is away from the array broadside direction [7], and the best SLL is around -13.5 dB. In contrast, the volumetric random array can maintain a constant beamwidth with isotropic radiators for elements with uniform density distribution [6]. Additionally, the volumetric random array

can provide 3π ($0 \leq \theta \leq \pi$, $0 \leq \phi \leq 2\pi$) scan coverage in both elevation and azimuth, which is favorable for the mobile platform application. When increasing the antenna elements, the average SLL significantly decreases by a factor of $1/N$, where N is the total array elements [4]. Thus, random array application is likely to increase the antenna elements to lower the SLL rather than adopt amplitude tapering. This results in a better received power compared to the tapering one. The random position of the array elements effectively eliminates the grating lobes and provides a smaller RCS [10]. Therefore, the spacing between each antenna element can be extended greater than a half wavelength without causing the grating-lobe problem. The greater spacing results in an increased directivity, a better angle resolution, and less influences by mutual coupling [5].

This work provides the first experimental demonstration of RHCP beamforming in volumetric random arrays using arbitrarily oriented antenna elements. This work also seeks to advance the capabilities of spatially distributed antennas deployed on mobile platforms.

3.2. Beamformer System Overview

A block diagram of the beamformer system is shown in Fig. 19. The array system consists of patch antennas, vector modulators (variable attenuators and phase shifters), a voltage control board, a spatial recognition system, and the controller. The controller collects all the information and calculates the desired phases for each array element.

Operationally, the desired scan angle is entered into the controller, which is simply a personal computer loaded with the control codes. The CW signals generated by the VNA

are directly connected to an equal-split sixteen-way Wilkinson power divider. Other components are described in detailed in this section.

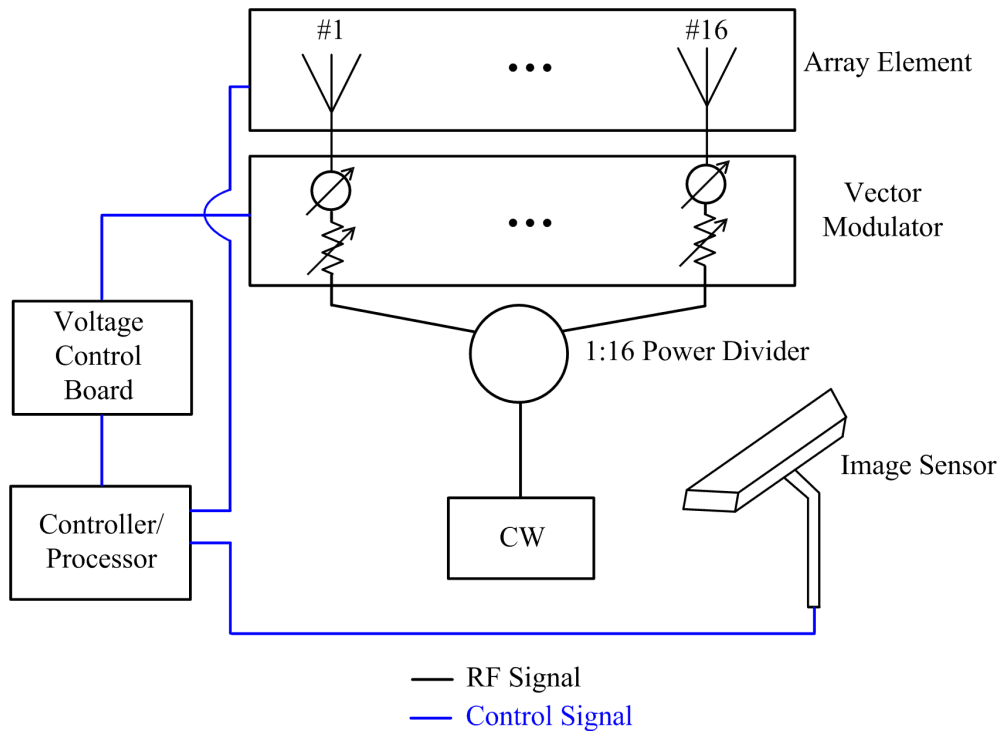


Figure 19 Beamformer architecture.

3.2.1. Microstrip Patch Antenna

The microstrip patch antenna acting as the array element has linearly-polarized characteristic. The linearity simplifies the follow-on derivation of the RHCP phases (each patch has random orientation). The patch is well designed to operate at 2.4 GHz with approximately 50Ω input impedance; therefore, no extra impedance matching network

needs to be added, which significantly reduces the complexity and cost of the antenna element. These antennas are fabricated on 62 mil (1.57 mm) thick FR4 ($\epsilon_r = 4.4$) and have a width $w = 38$ mm and resonant length $L = 28$ mm. The FR4 substrate is not a proper candidate for antenna design because the high dielectric constant characteristic of the FR4 makes the electric field difficult to radiate. However, the FR4 is the most common material used in the printed circuit board (PCB) manufacturing, and in this work, there are other electronic components needed to embed with the antenna. Thus, the FR4 still has to be chosen as the antenna substrate, and the antenna gain is acceptable for this application. The SMA probe feed is placed at a distance of 6 mm from the patch edge. Fig. 20 shows the measured VSWR and input impedance of the patch antenna from 2 GHz to 3 GHz. The antenna has a 2:1 VSWR bandwidth of 60 MHz (from 2.365 GHz to 2.425 GHz) centered at 2.395 GHz. Fig. 21 shows the measured radiation pattern at 2.4 GHz for the two-elevation cut-planes. The antenna has a maximum gain of 2.97 dB and a HPBW of $\text{HPBW}_0 = 75^\circ$.

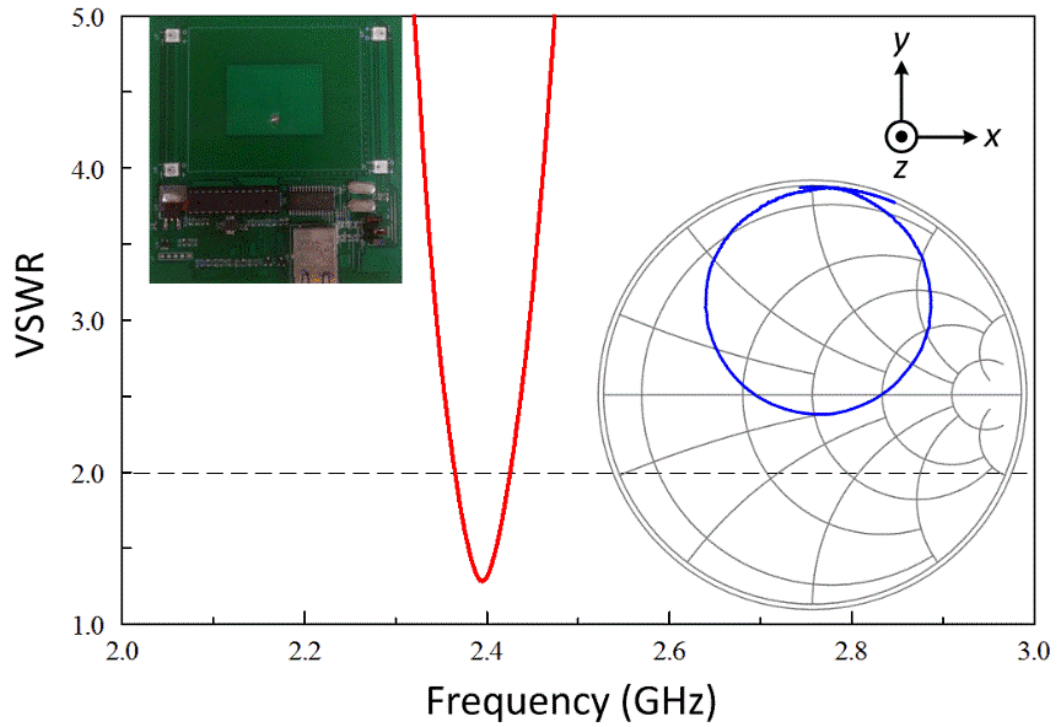


Figure 20 Measured VSWR and Smith Chart (overlaid) of the microstrip patch.

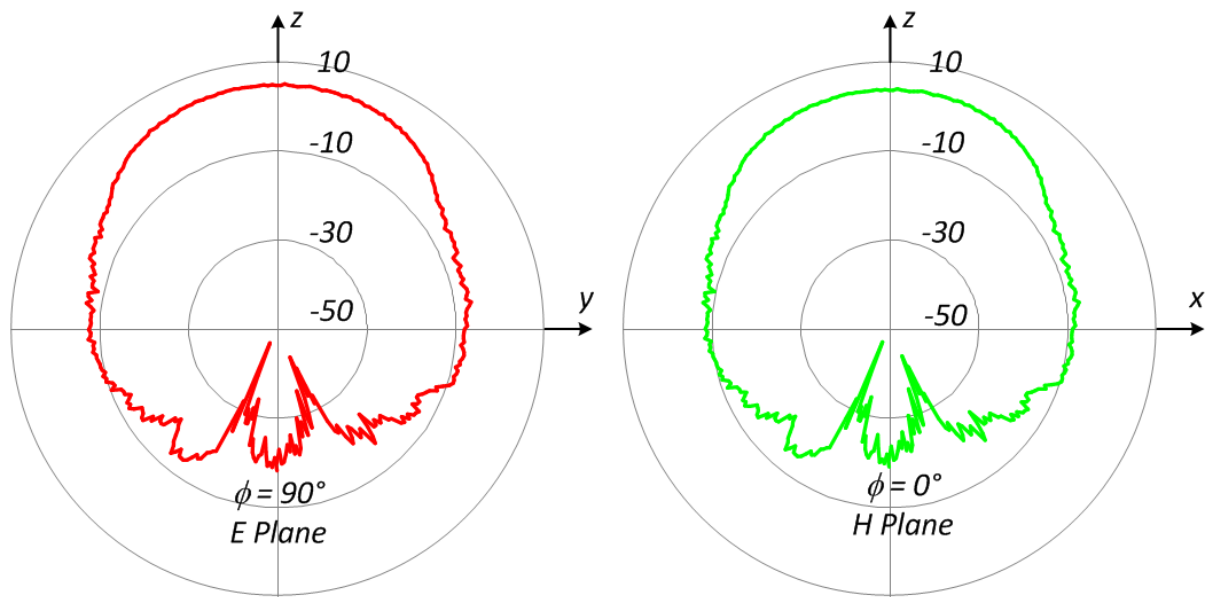


Figure 21 Measured radiation pattern (dB) of the microstrip patch.

There are other control circuits embedded with the antenna to fulfill the purposes of the position and orientation detection. The functionality of these components, such as LEDs, 9 degrees of freedom (DOF) inertial measurement units (IMU), and local area network (LAN) sockets, are further illustrated in the following sections.

3.2.2. Vector Modulator

The analog vector modulator [30] has both continuous 360° phases and 40 dB gain controls over 0.5-2.5 V bias voltage. By varying the in-phase (I) and quadrature (Q) voltages, the corresponding gains (G_n) and phases (θ_n) can be obtained and represented as

$$I_n + jQ_n = G_n e^{j\theta_n}, \quad (10)$$

where n is the antenna element number in the volumetric random array.

Nonetheless, this task mainly focuses on the RHCP beamforming rather than the beamshaping (excitation tapering), and hence the gain of each antenna element is fixed to the unity. The control voltages, I and Q , ranging from 0.5V to 2.5V, have the minimum gain (null point) centered at $I = 1.5V$ and $Q = 1.5V$. In practice, the I/Q circle slightly deviates from the center points (± 100 mV according to the data sheet [31]), and each board has a unique offset. To provide a precise measurement, a calibration procedure is adopted before the measurement to minimize the errors.

After the calibration process, there are four essential parameters needed to be acquired and they are V_{mi} (I voltage at null point), V_{mq} (Q voltage at null point), G_{max} (maximum gain in dB) and $\phi(f)$ (phase offset in degrees at f frequency). Once the four parameters are obtained, the desired gains and phases can be calculated by using [31]

$$G = G_{max} * 2 \sqrt{\left(\frac{I-V_{mi}}{V_r}\right)^2 + \left(\frac{Q-V_{mq}}{V_r}\right)^2}, \text{ and} \quad (11)$$

$$\angle\theta = \tan^{-1}\left(\frac{Q-V_{mq}}{I-V_{mi}}\right) + \Phi(f), \quad (12)$$

where V_r is the maximum voltage range from either I or Q .

From the system's perspective, the overall maximum gain should be constrained by the minimum gain of the sixteen vector modulators. Similarly, the $\phi(f)$ from each vector modular should compensate for the discrepancy (different length of the transmission line) from other vector modulators to have a consistent phase reference.

3.2.3. Voltage Control Board

The voltage control board (in Fig. 22) established in [27] is used to generate bias voltages to the phase shifter. In this work, the same board is used, but the output voltage (original is from 0 to 12 V) is divided to provide voltages ranging from 0 to 2.5 V with increment of 0.38 μ V. The difficult part of the board design is to provide linear phase shifts along the output voltages. Therefore, a fourth-order polynomial is used to represent the relationship of how the corresponding output voltages affect the phases. The board can provide a maximum of thirty-two channels of digital to analog converter (DAC) with each channel having sixteen-bit resolution.



Figure 22 Photo of a voltage control board.

3.2.4. Spatial Recognition System

The spatial recognition system built by [29] is used to estimate the relative position location of each antenna element (X, Y, and Z in Cartesian coordinate) on the Medusa platform. The system is assembled by sixteen antenna modules, a Kinect motion sensor, a sixteen-port TCP/IP router, and a server with a Java based control program. Each antenna module contains a microstrip patch antenna, four RGB LEDs, a microcontroller (Atmel 328p), and TCP/IP interface circuits. To acquire the XYZ position of each array element, step by step procedures are described as follows. First, the Kinect projects an infrared laser to the antenna module, and the reflected waves captured by a monochrome CMOS sensor are used to estimate the depth information (Z position). Next, a specific color pattern of

the four LEDs is generated. To successfully capture a clear LED image from the antenna module of interest, a program is designed to filter out the background noise. Then the Kinect RGB camera collects the real-time images and reports them back to the processor to evaluate the XY positions of the target antenna module.

After the process of the position acquisition is performed sequentially through all the array elements, the estimated positions are obtained and can be used to calculate the corresponding distance phases. Fig. 23 shows the Medusa platform placed on the turning table and an image sensor faces the array to estimate the XYZ positions. The control signals between the antenna modules and the server are transmitted back and forth through the TCP/IP interface. The private LAN is established to avoid the interference from another network traffic.

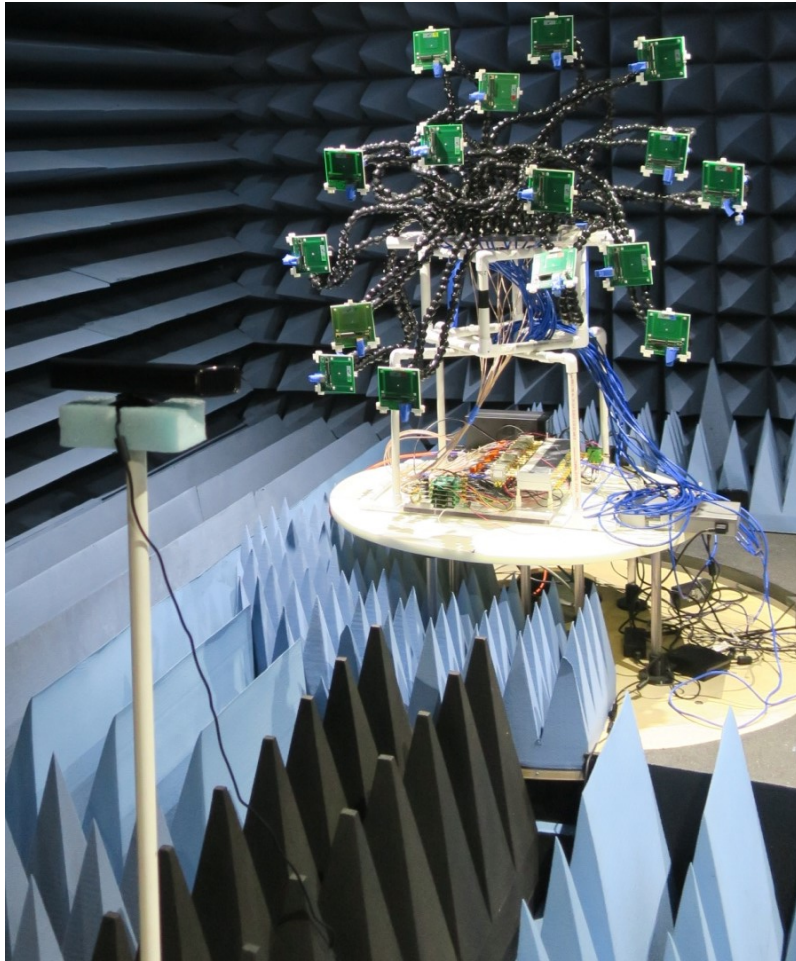


Figure 23 A volumetric random phased array placed on the turning table and a camera is used to capture the XYZ positions of the array.

3.2.5. Antenna Orientation

To successfully calculate the rotation phases, it is necessary to obtain the orientations of each array element first. A 9 DOF IMU sensor [32] is embedded on each antenna module to provide the yaw, pitch, and roll angles. The IMU sensor includes a digital angular rate sensor (gyroscope), a digital acceleration sensor (accelerometer), and

a digital magnetic sensor (magnetometer). It provides a total of 9 DOF information in a single chip. The accelerometer provides acceleration data in $\pm 2g$, $\pm 4g$, $\pm 6g$, $\pm 8g$, or $\pm 16g$ scale, where g is the gravity that is equals to 9.8 m/s^2 . The magnetometer measures the direction and strength of the magnetic fields in ± 2 , ± 4 , ± 8 , or ± 12 gauss scale. The gyroscope measures the angular velocity of a rotating object along the axes, and the scale can be set to ± 245 , ± 500 , or ± 2000 degrees per second (DPS). In general, a smaller scale provides a better resolution in these three sensors.

3.3. RHCP Rotation Phase Estimation

In [13], the polarization is described as “the shape and locus of the tip of the E vector (in the plane orthogonal to the direction of propagation) at a given point in space as a function of time.” In this work, the microstrip patch antenna has a linear polarization characteristic. To have a RHCP radiation pattern, a phase difference of 90° between the x-axis and the y-axis has to be created [13]. In fact, the y-axis should have a 90° phase delay after the x-axis. For the arbitrarily oriented antenna element; each antenna element should add a corresponding rotation phase, which is based on the antenna orientation. Extending from the results in Chapter 2, the rotation phases are proportional to the rotation angles, which are the relative angles between antennas on the scan angle plane.

3.4. Experiments and Results

Fig. 24 shows the G_{RHCP} of the measured and simulated results, when θ scans from -180° to 180° at $\phi = 0^\circ$. The measured RHCP gains are normalized and combined with the simulated ones for comparison. Both results have normalized maximum G_{RHCP} of 17.1 dB

at $\theta = \phi = 0^\circ$. The measured and simulated SLL_{RHCP} are both close to -8.2 dB, which are below its maximum gain respectively.

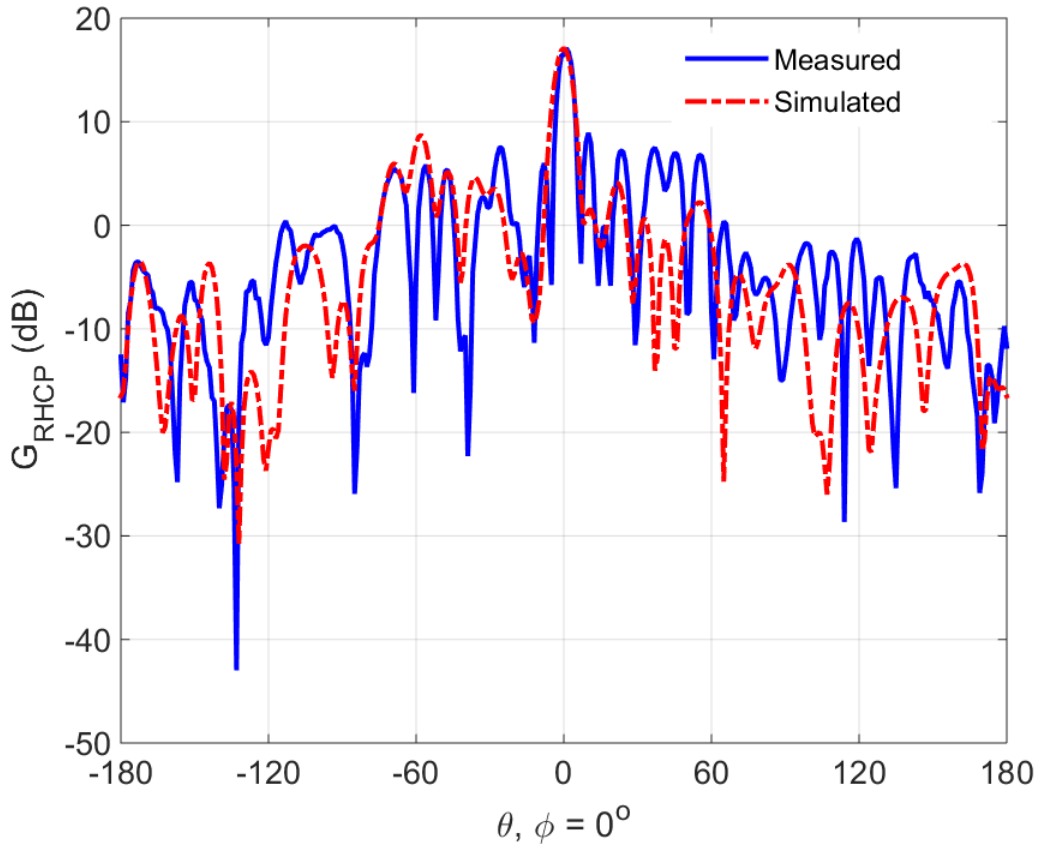


Figure 24 Comparison of measured and simulated G_{RHCP} pattern.

Fig. 25 shows the G_{LHCP} of the measured and simulated results when θ scans from -180° to 180° at $\phi = 0^\circ$. The measured and simulated LHCP gains are -8.7 dB and -2.6 dB at $\theta = \phi = 0^\circ$, respectively.

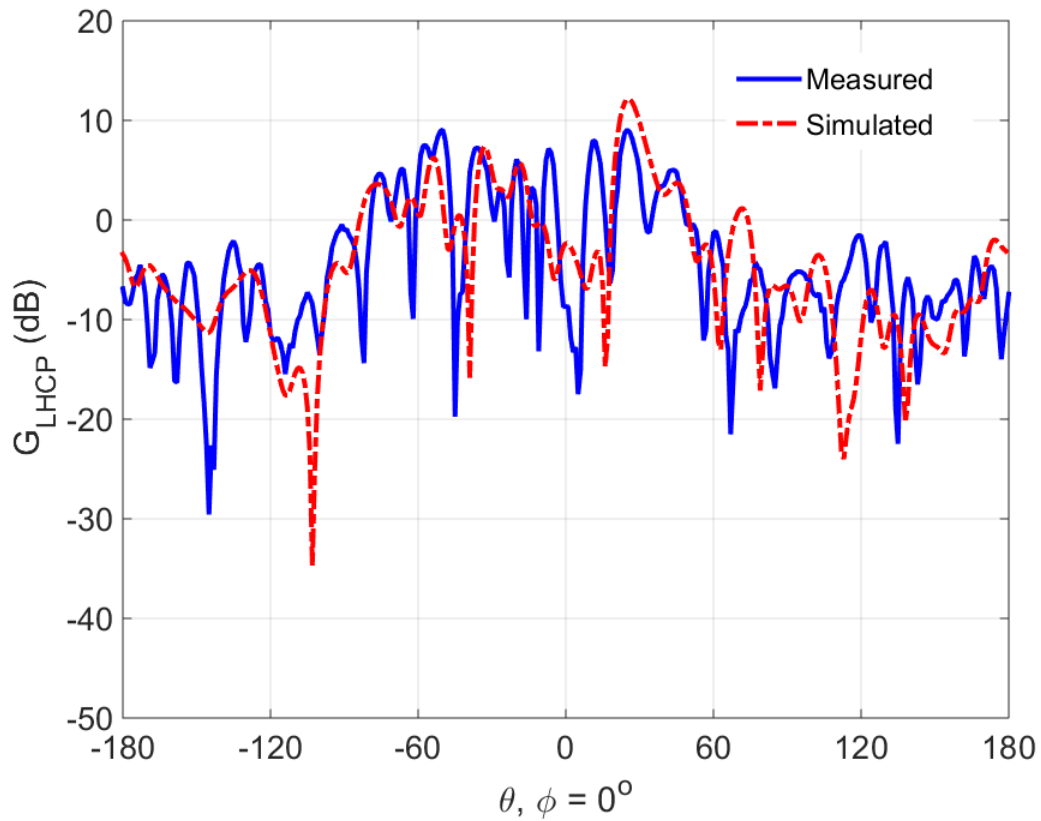


Figure 25 Comparison of measured and simulated G_{LHCP} pattern.

The results prove that the algorithm works correctly because a maximum RHCP and a relative minimum LHCP gain are observed at the scan angle. Overall, there are no grating lobes observed in the visible region. Some pattern deviations are caused by the spatial recognition system and the 9DOF IMU accuracy, but the pattern tendency is very close to the simulated results.

3.5. Conclusion

3.5.1. Discussion

This project successfully demonstrates beamforming by using sixteen microstrip patch antennas in a volumetric random array, with each element arbitrarily oriented and a RHCP radiation pattern created. The whole array is divided into several sub-systems, and its function is clearly elaborated in this article. The algorithm on how to estimate the rotation angles and transform rotation phases for each tilted antenna is explained. Simulated and measured radiation patterns for the random array are provided, and comparisons between them are made.

3.5.2. Summary

There are no grating lobes observed within the visible region, and the result is in accordance with the expectation. However, the SLL around the main beam is still high, especially when a small number of elements are used. The algorithm used to calculate the rotation phases for each array element is applicable for any scan angles. This method greatly reduces the phase errors that arose in the previous project (*An Investigation of Beamforming Using Dissimilar Antennas in Volumetric Random Arrays*). Nevertheless, it is necessary to develop another SLL reduction algorithm, particularly for a small number of elements.

4. AMPLITUDE TAPERING ON VOLUMETRIC RANDOM ARRAYS*

4.1. Introduction

Based on the suggestions of “An Investigation of Beamforming Using Dissimilar Antennas in Volumetric Random Arrays” and “Circular Polarized Beamforming on Volumetric Random Arrays with Arbitrarily Oriented Array Elements” concluded in chapters 2 and 3, an amplitude tapering algorithm specifically developed for the volumetric random array is necessary to further reduce the SLL around the main beam. To achieve our final goal (wireless phased arrays on mobile platforms), a 3D beamshaping algorithm needs to be developed along with the investigation of beamforming characteristics for swarming UAVs in this project.

The great advantage of the random array is the non-tapering requirement to lower the SLL because it uses its stochastic element positions to effectively cancel the sidelobes (destructive interference). In this work, we applied the amplitude tapering on a random array that seems contradictory to the virtue of randomization. However, the sidelobe cancellation for a small number of array elements (typically less than 32 elements) is trivial because the average SLL decreases by a factor of $1/N$, where N is the element number [4]. For some specific cases like a small number of array elements, applying tapered amplitude along the array aperture seems to be a more feasible way to further

*Part of the chapter is adapted from S. Yeh, J. F. Chamberland and G. H. Huff, "An investigation of geolocation-aware beamforming algorithms for swarming UAVs," *2017 IEEE International Symposium on Antennas and Propagation & USNC/URSI National Radio Science Meeting*, San Diego, CA, 2017, pp. 641-642.

reduce the SLL. Note that adopting more elements to lower the SLL is a more preferable way for making random arrays.

Next, we need to understand why developing a 3D rather than a linear or a planar beamshaping algorithm is necessary. For UAVs swarming in the air, it is impractical to align on a planar surface and maintain a uniform spacing because UAVs are more susceptible to the wind. A volumetric geometry is close to the drone's formation. Combining all these criteria, a 3D amplitude tapering algorithm [33] is an advisable solution to deal with the volumetric geometry and a small number of array elements.

4.2. Theory

4.2.1. Previous Work

Many researchers already did great comprehensive works on amplitude tapering for linear and planar array. Nonetheless, the volumetric array amplitude tapering method is still not widely reported in the open literatures. Before starting the work, it is necessary to gain some background knowledge to help us better understand this problem. Some reports related to SLL reduction for the volumetric array are available in [23, 28, 34]. Introduced in these reports are a concept called “density tapering” [23]. The array aperture is the smallest region that encloses all the antenna elements. The scan angle vector is the unit vector from the origin to the scan angle direction, and the array aperture plane is perpendicular to the scan angle vector. If the location of each array element is distributed uniformly, this array automatically has the density tapering characteristic. In other words, this kind of distribution lowers the SLL by nature without touching any excitation

amplitudes. When examining the distribution closely, we find that the distribution has the property of high density in the middle and low density around the edge. One is the Taylor distribution with an averaged SLL of -35 dB [23], and the other is the uniform distribution with an averaged SLL of -27 dB [23]. From the results, we can conclude that the more concentrated distribution in the middle leads to a higher SLL reduction.

For the density tapering result, it is more like a phenomenon than a method because the performance is not guaranteed. For the worst-case scenario, it may have high density distributed in the middle while causing minimum electrical fields at the same time (destructive interference from the phases difference). Due to the reasons mentioned above, it is not a systematic way to deal with the depth differences for the volumetric random array. Instead of lowering the SLL by element distribution, a more general, flexible and practical way is to adjust the excitation of each array element.

4.2.2. Amplitude Tapering for Linear and Planar Arrays

Before investigating the 3D amplitude tapering, it is suggested to contemplate on the conventional amplitude tapering method for linear and planar array. Amplitude tapering techniques have been used on linear and planar array for years. With the proper amplitude distribution along the array aperture, the beam shape changes accordingly. The amplitude tapering can start from the aperture origin (high amplitude) to the edge (low amplitude) or from the edge (high amplitude) to the origin (low amplitude). While the amplitude tapers from low (aperture origin) to high (edge), the HPBW becomes narrower. While the amplitude tapers from high (aperture origin) to low (edge), the HPBW becomes

broader. Similarly, the SLL increases for low (aperture origin) to high (edge) tapering; the SLL decreases for high (aperture origin) to low (edge) tapering.

A five-element, uniform spacing (a half wavelength), and isotropic radiators linear array is used to demonstrate the beamshaping effects [35]. A_n is the current amplitude of the n -th antenna, where $n = 1 \dots 5$, and it is normalized to unity at aperture origin. For example, a uniform current distribution gives a -12 dB SLL, and a Binomial current distribution has a $-\infty$ SLL.

From the conclusion made in [35]: “As the current amplitude is tapered more from the center to the edge of an array, the side lobes decrease and the beamwidth of the main beam increases.” The current distribution and the radiation pattern are Fourier transform or inverse Fourier transform pairs of each other [36]. Note that the phased array is constructed by discrete antennas, so it is a sampled aperture rather than a continuous aperture. Therefore, the radiation pattern is estimated by using the discrete Fourier transform rather than the fast Fourier transform.

4.2.3. Preliminary Test

From the previous study [35], a basic beamshaping technique for a five-element linear array has been introduced. In this preliminary test, the same technique would be forced to conduct simulations on the linear, planar, and volumetric random arrays with main beam scans to $(\theta_s, \phi_s) = (0^\circ, 0^\circ)$ to examine the results. The SLL from the volumetric random array is used to benchmark with the linear and planar ones to evaluate the impact from the depth. The depth is defined as the relative distance of each array element's

position vector projected on the scan angle vector. Clearly the depth changes with different scan angles.

One common feature of linear and planar arrays is that the array elements are all located on a planar surface, so their tapered amplitude, for $(\theta_s, \phi_s) = (0^\circ, 0^\circ)$, is assigned by the distance away from the origin. However, for volumetric random arrays, each array element has to project on the scan angle plane, which is a plane orthogonal to the scan angle vector. Then the tapered amplitudes can be assigned by the projection distances. Figures 26 to 28 display the radiation patterns before and after applying amplitude tapering. The Binomial coefficient of 1, 6, 15, 20, 15, 6, is implemented in this test.

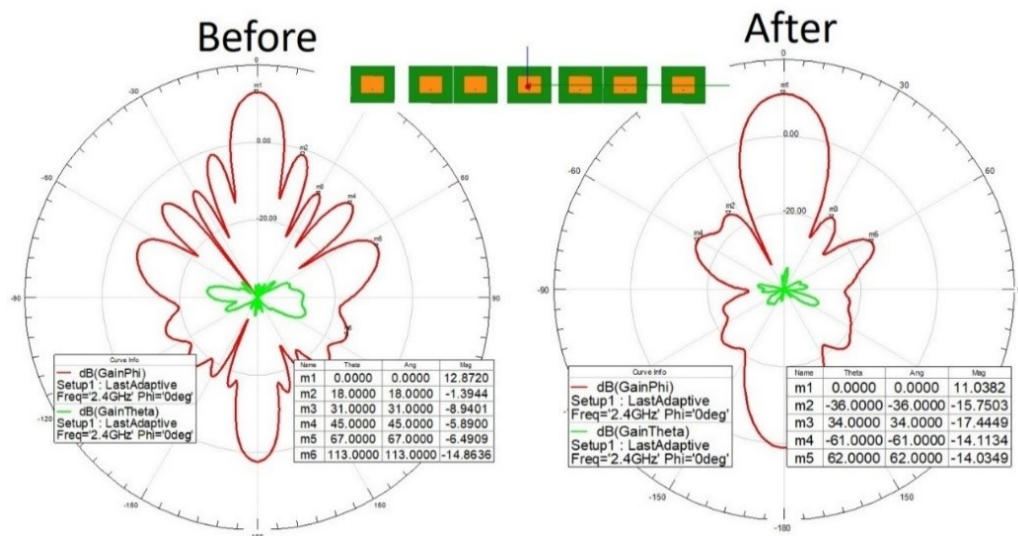


Figure 26 Radiation patterns of the linear random array with (right) and without (left) amplitude tapering.

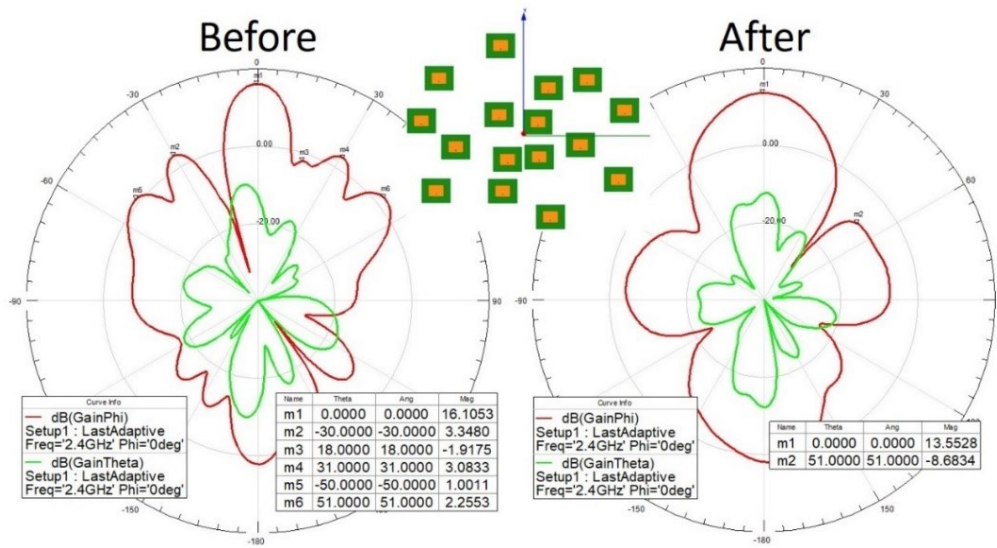


Figure 27 Radiation patterns of the planar random array with (right) and without (left) amplitude tapering.

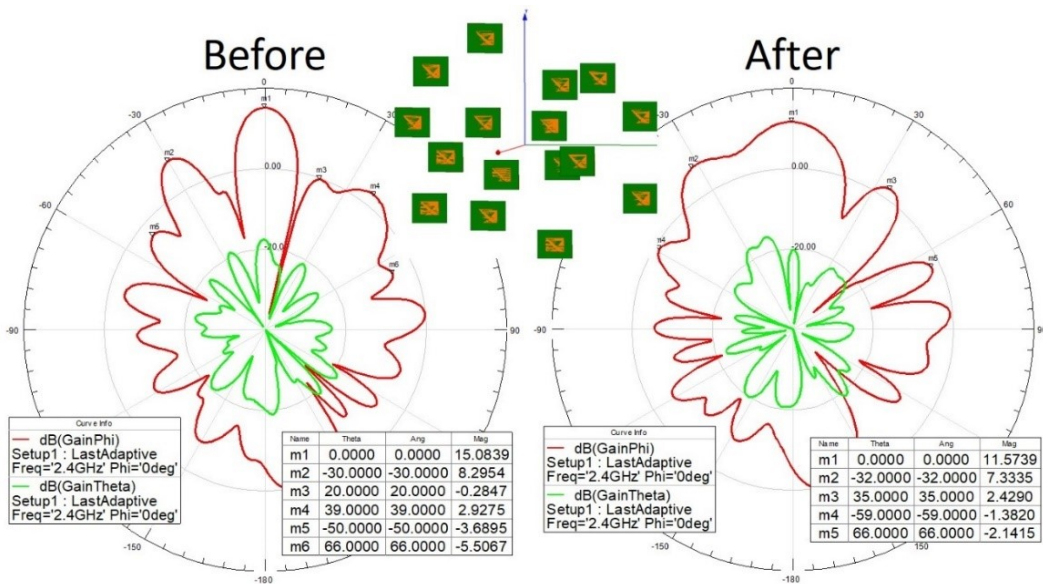


Figure 28 Radiation patterns of the volumetric random array with (right) and without (left) amplitude tapering.

The results show that the linear and planar random array reduce SLLs significantly, and parts of the sidelobes merge into the main beam. The lower SLL benefit comes with the side effects of reduced directivity, broader HPBW, and low aperture efficiency. However, the reduction effect of a decent SLL is not seen on the volumetric random array, which is in agreement with the expectations. This test illustrates that the depth of the volumetric random array deteriorates the beamshaping result.

4.3. 3D Amplitude Tapering Procedures

In this work, a unique tapering algorithm specially pays attention on the depth information for the volumetric array. Following the explanation theory for the volumetric random array, unique step by step amplitude tapering procedures are clearly illustrated and demonstrated in this section. Fig. 29 shows our experimental array consisted of sixteen patch antennas spatially stochastically distributed in a 3D space. The volumetric array with the same element distribution is assembled and placed in the anechoic chamber (as shown in Fig. 30). The array is evaluated at 2.4 GHz, and both the simulated and the measured arrays use the same coordinate system. In other words, all the antennas are y polarized and orthogonal to the z-axis.

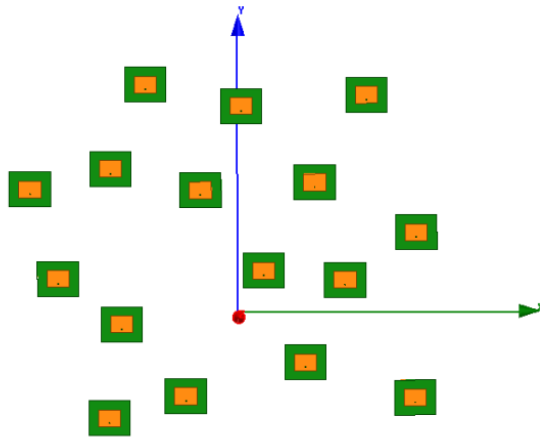


Figure 29 A sixteen-element volumetric random array modeled in the HFSS.

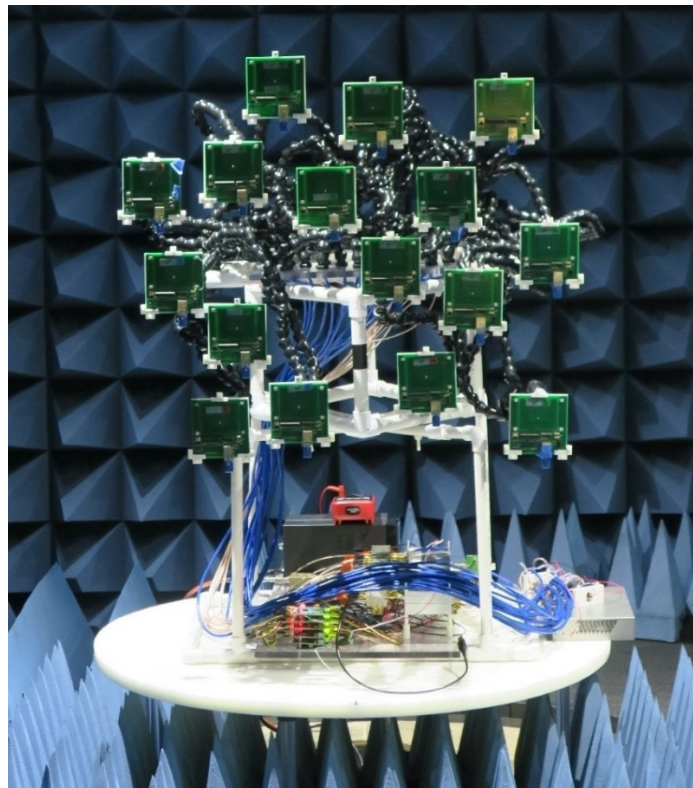


Figure 30 A sixteen-element volumetric random array implemented on the Medusa platform and measured in the anechoic chamber.

4.3.1. Beamforming and Phase Optimization

Drive the main beam to the signal of interest angle (θ_s, ϕ_s) and, at the same time, create the scan angle vector \bar{S} by

$$\bar{S} = \hat{x} \sin \theta_s \cos \phi_s + \hat{y} \sin \theta_s \sin \phi_s + \hat{z} \cos \phi_s. \quad (13)$$

Assuming that the observation point is located in the far-field; therefore, the distance phases for array element could be obtained by antenna position vector dot product \bar{S} (transform to degrees with known wavelength). Nevertheless, due to the mutual coupling effects, an extra phase optimization step could be considered to raise the phase accuracy.

4.3.2. Tapering Methods

Three kinds of tapering approaches that can be used in this experiment and they are radial, horizontal, and vertical tapering. For azimuth scan projects, it is suggested to taper horizontally. Likewise, for 3π scan coverage task, it is recommended to taper according to the radius. The horizontal tapering technique is illustrated in this dissertation.

To achieve the horizontal tapering technique, one reference vector \bar{u} is essential to create by

$$\bar{u}(x, y, z) = (\cos \theta_s \cos \phi_s, \cos \theta_s \sin \phi_s, -\sin \theta_s). \quad (14)$$

Next, the antenna elements need to project to the \bar{u} vector. After that, in the amplitude mapping procedure, the projection vectors information will be used to determine the corresponding tapering amplitudes.

4.3.3. Define Array Aperture

To deliver precise current distribution to each array element, the first step is to identify the array aperture and determine the location of the aperture origin. Fig. 31 shows sixteen array elements projected on the array aperture. The array aperture is the smallest region that encloses the utmost left and right phased array elements and the array aperture plane is perpendicular to the scan angle \bar{S} . Obviously, the array aperture is dependent on the scan angle. Take horizontal tapering method for example, the positions of the utmost left and right are assigned as the aperture boundary.

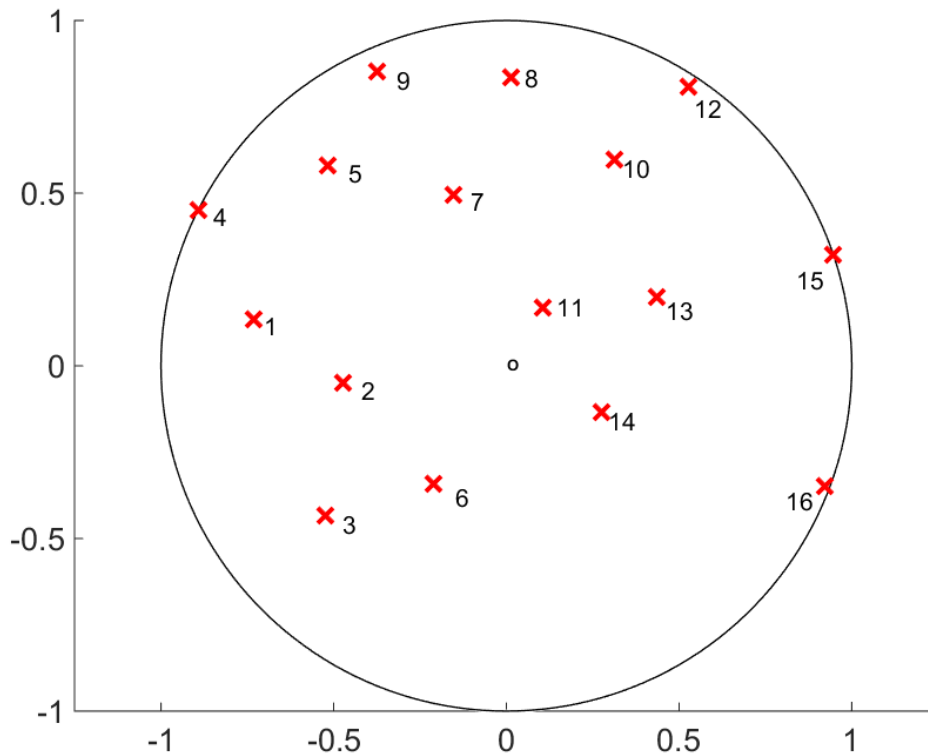


Figure 31 Sixteen array elements (red cross) projected on the array aperture.

4.3.4. Amplitude Mapping (Binomial)

In this task, the Binomial numbers (1, 6, 15, 20, 15, 6, 1) are demonstrated as the amplitude coefficients distributed along the aperture (as the blue curve shown in Fig. 32). Next, assign each array element to the relating amplitudes based on the distance how far you are away from our designated aperture origin. Therefore, the red cross spots are the results of the antennas' mapping amplitudes.

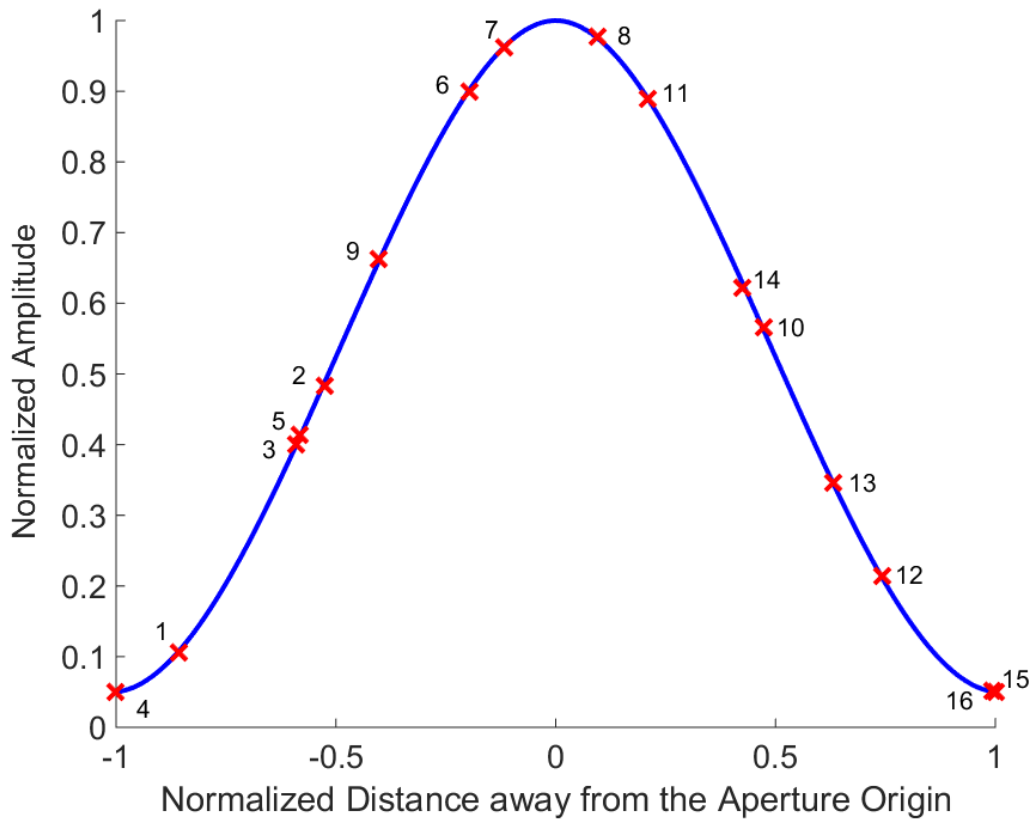


Figure 32 Sixteen array elements map to the normalized amplitude tapering curve (blue curve).

4.3.5. Amplitude Averaging

An ideal current distribution will result in a smallest SLL outcome. However, if some elements are too close to each other, it will create spike amplitude away from the ideal amplitude tapering curve. Thus, it is necessary to average the amplitudes to alleviate the spike amplitude. Fig. 33 shows the results of amplitude averaging for proximity antennas. For example, element 3 and 5 are close to each other; therefore, both of their amplitudes are divided by 2.

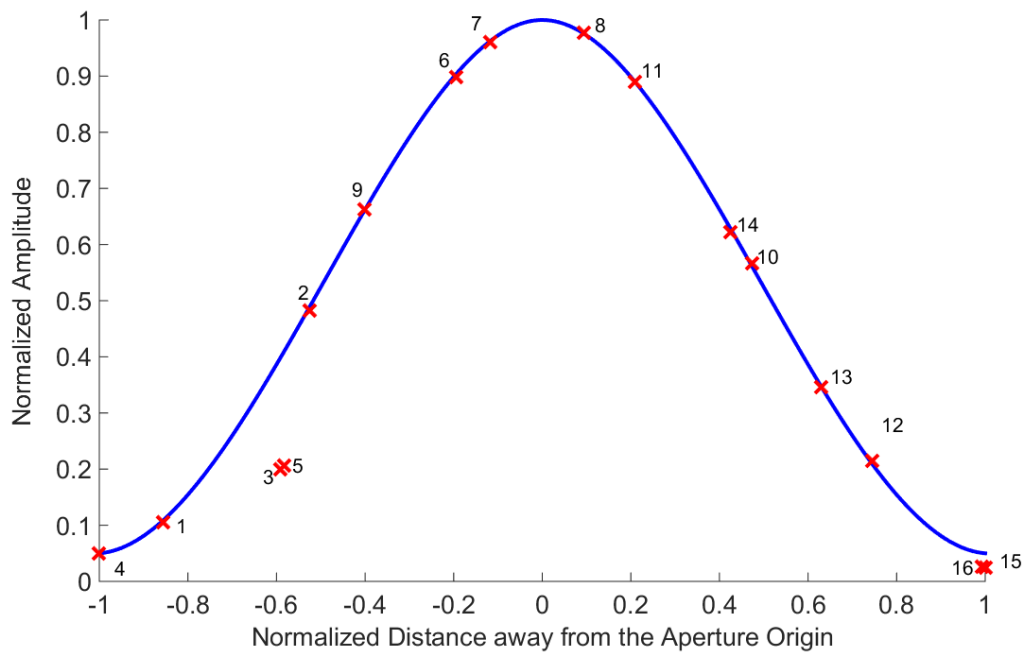


Figure 33 Amplitude averaging for proximity antennas.

4.3.6. Depth Gain

One major difference compared the volumetric array to the 1D or 2D array is the depth. Therefore, the further array element needs to be taken into consideration to reimburse for the excitation amplitude loss.

The depth is defined as the nearest distance between the array elements and the aperture plane. The aperture plane is the plane perpendicular to the \bar{S} . Once the depth of each array element is obtained, we map the depth to the power decay line, as shown in Fig. 34. The lost power from the depth need to add back to each antenna.

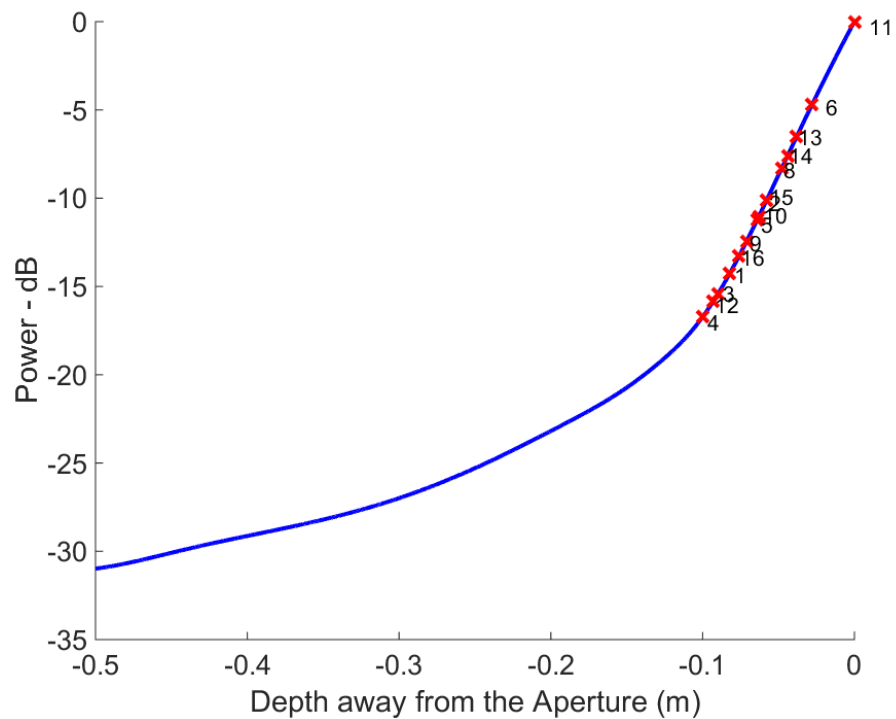


Figure 34 Propagation loss of an antenna from 0 m to 0.5 m.

4.4. Simulated and Measurement Results

The simulated and measured radiation patterns of the sixteen-element volumetric random array with tapering, non-tapering, and expected values are plotted in Fig. 35 and Fig. 36, respectively. The expected values are the theoretical radiation pattern of a sixteen-element volumetric random patch array, and they are derived by using the pattern multiplication method. The total expected pattern is that the sixteen-element AF multiplies the element pattern of a single patch antenna. The element pattern of the patch antenna is from the HFSS simulated data, and the AF of the sixteen-element volumetric random array is from the equation in [5]. The gains from these three results are all normalized to the maximum gain of the expected values for a better comparison. In this experiment, our interested sidelobes are set from -45° to 45° . For simulated results, the maximum gains are around 22 dB and located at the array broadside, which is $(\theta, \phi) = (0^\circ, 0^\circ)$. The SLL of the array without amplitude tapering is -11 dB ($\theta = -15^\circ$), and the SLL with amplitude tapering is -17 dB ($\theta = -27^\circ$). There is a 6 dB sidelobe reduction after using our developed tapering method. With the compromise of wider beamwidth, lower aperture efficiency, and lower directivity, the amplitude tapering approach significantly lowers the maximum SLL and moves the sidelobe away the main beam.

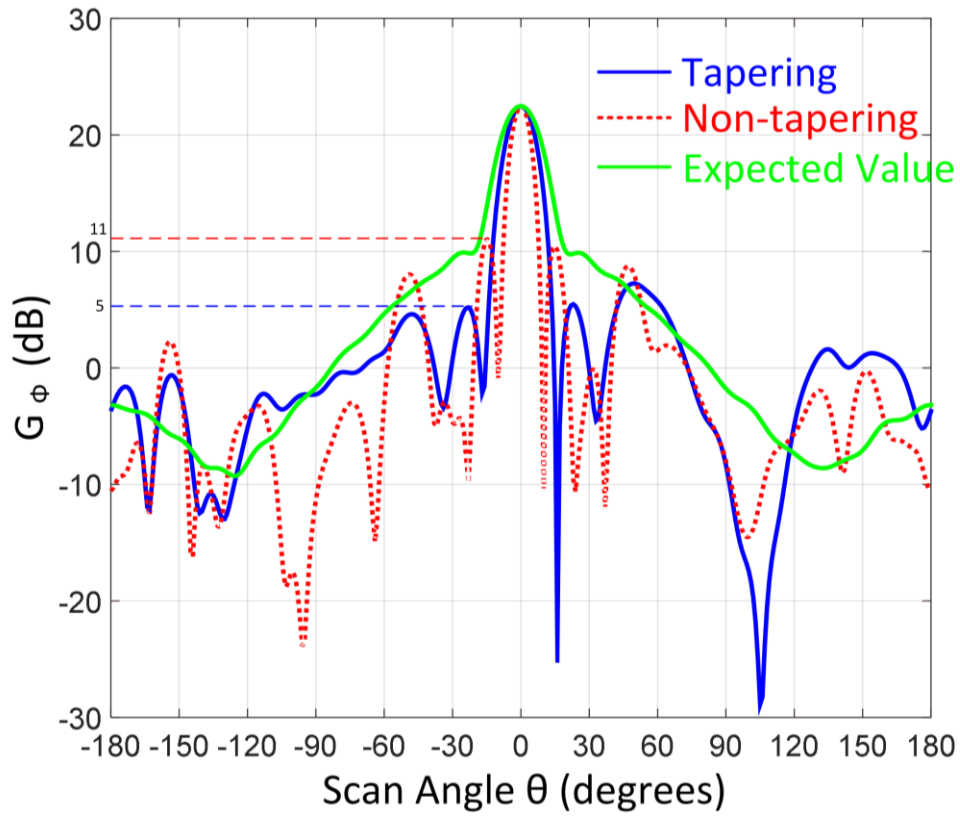


Figure 35 Simulation results of tapering, non-tapering, and expected value ($\phi = 0^\circ$).

For measured results, the radiation pattern of the sixteen-element volumetric random array is measured in the anechoic chamber (located at the Electromagnetics and Microwave Laboratory, Department of Electrical and Computer Engineering, Texas A&M University) to reduce interferences from multipath and simulate the free space environment. Considering position acquisition and movement, the Medusa platform is chosen as our testing array (as shown in Fig. 30). The platform is well centered on the turning table in the chamber to minimize pattern distortion. The measurement is

implemented by rotating the array from -180° to 180° on the x-z plane ($-180^\circ \leq \theta \leq 180^\circ$ and $\phi = 0^\circ$).

The maximum gains are around 22 dB, and they are located at the array broadside, which is $(\theta, \phi) = (0^\circ, 0^\circ)$. The SLL of the array without amplitude tapering is -10 dB ($\theta = -15^\circ$), and the SLL with amplitude tapering is -19 dB ($\theta = -27^\circ$). There is a 9 dB sidelobe reduction after using our developed tapering method. With the sacrifice of wider beamwidth, decreased directivity, and smaller aperture efficiency, the amplitude tapering approach lowers the maximum sidelobe and moves the sidelobe away the main beam.

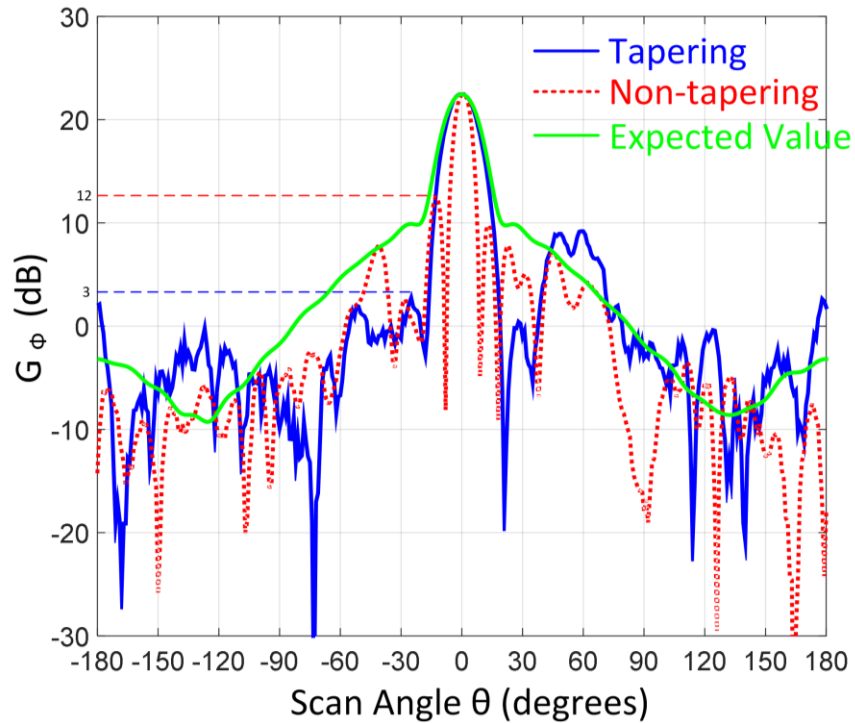


Figure 36 Measured results of tapering, non-tapering, and expected value ($\phi = 0^\circ$).

From both simulated and measured results, the developed tapering algorithm reduces the SLL at least 6 dB and moves the sidelobes away from the main beam (from -15° to -27°). The two maximum sidelobes merge into the main beam. Both simulated and measured results are in accordance with each other, and this proves that the designed 3D amplitude tapering algorithm can successfully deal with the volumetric scenario.

4.5. Conclusion

This work successfully develops an amplitude tapering algorithm specifically for the volumetric random array. The procedures of the amplitude tapering are clearly illustrated and explained. Both simulated and measured results of tapering, non-tapering, and expected values are provided to verify this method. The goal of developing a 3D beamshaping algorithm that can easily be implemented on volumetric cases to further minimize the SLL was successfully achieved.

5. A MAGNETLESS DUPLEX RETRODIRECTIVE PATCH ARRAY WITH PHASE SHIFTERS FOR SIGNAL RELAY

5.1. Introduction

This project investigated the reflect beamforming technique based on the Van Atta array structure [37]. The Van Atta array is one of several types of retrodirective reflectors that has been implemented on a number of applications, including satellite communication [38], remote identification [39], RCS enhancement, navigation systems, RFID interrogation [40, 41], and wireless power harvesting. The concept was first proposed by L. C. Van Atta and claimed as a patent in 1959 [37]. The proposed array automatically reflects the received signals back to the signal source without any prior knowledge of DOA.

The theory behind the automatic reflection is not complicated. If we make the spacing between each antenna uniform and connect the antennas in pairs (#1 connects to #4, and #2 connects to #3 [39]) with the same length transmission lines ($l_1 = l_2$), the incident waves will reflect back to the signal source automatically [39].

One major feature of the Van Atta array is its conceptual simplicity, which includes a concise microwave circuit (pairs of antennas connected by transmission lines) and a method/algorithm to reradiate back the incoming signals (maximum power in the incident angle). In the same manner, to accomplish the task by using the conventional DF method, the incoming signals have to be digitalized and fed to the computer to determine the

DOAs. This method requires more resources and a longer latency for the system to respond; therefore, for some time-sensitive applications, it may not be advisable. On the contrary, the Van Atta array is a true real-time system, and the response time is the duration from the received incident waves propagate to the paired reradiated antenna, which is around 845.22 ps for $1.5 \lambda_g$ path length (on the 31 mil Duroid 5880 at 2.42 GHz). This advantage of the Van Atta array makes some high mobility applications become possible. Compared to other real-time retrodirective reflectors, such as the corner reflector, the Van Atta array can reflect over wider angles [42].

In addition, the characteristic that automatically reflects back makes the Van Atta array ideal for the jamming system. Normally when the jamming system is on, it transmits high power noise signals to the target direction. At the same time, the DF receiver working in conjunction with the jamming system has to be turned off. This kind of operation is called the stop-and-see method. In contrast to the stop-and-see method, the Van Atta array that reradiates the incident signals back to the sources can operate without any DF necessities. Obviously, this method can be categorized as the non-stop method or the non-stop jamming.

Since the Van Atta array has a low profile (light weight) feature, the whole array system can be embedded on mobile platforms. Mobile platforms may be swarms of UAVs, constellations of satellites, or fleets of ships. The major difference between the fixed platforms and the mobile one is the array element maneuverability. Take the aforementioned jamming system as an example: the original system already has $1/R^2$ advantage over the radar system. If the jamming systems are carried out by mobile

platforms, we can drive our carrier, such as drones, much closer to the target. With the help of mobile platform carriers, the jamming performance can improve significantly (reduce R to the target).

In this work, a retrodirective array prototype without main beam shifting is investigated first, and then a signal relay system based on the prototype was implemented by adding additional phase shifters and amplifiers. The relay system drives the reradiated beam to the signal dead zone, which is designed 30° away from the original reradiated angle. The prototype array (photographs shown in Fig. 37 and transparent design layout shown in Fig. 38) is constructed by two aperture-coupled microstrip patch antennas, two directional couplers, two delay line phase shifters, and a crossover ring. To maintain the simplicity, all the circuitry is required to deploy on a planar surface and optimized at 2.42 GHz. The array is composed of two 31 mils Duroid 5880 substrates ($\epsilon_r = 2.2$) and three metal layers, which are a top layer (patch array), a middle layer (ground and aperture-coupled slots), and a bottom layer (signal routing network circuitry). The effect of the mutual couplings among antennas, passive components, and microstrip lines is assumed small and neglected throughout this project.



Figure 37 Photo of the designed retrodirective array: top layer (left), middle layer (center), and bottom layer (right).

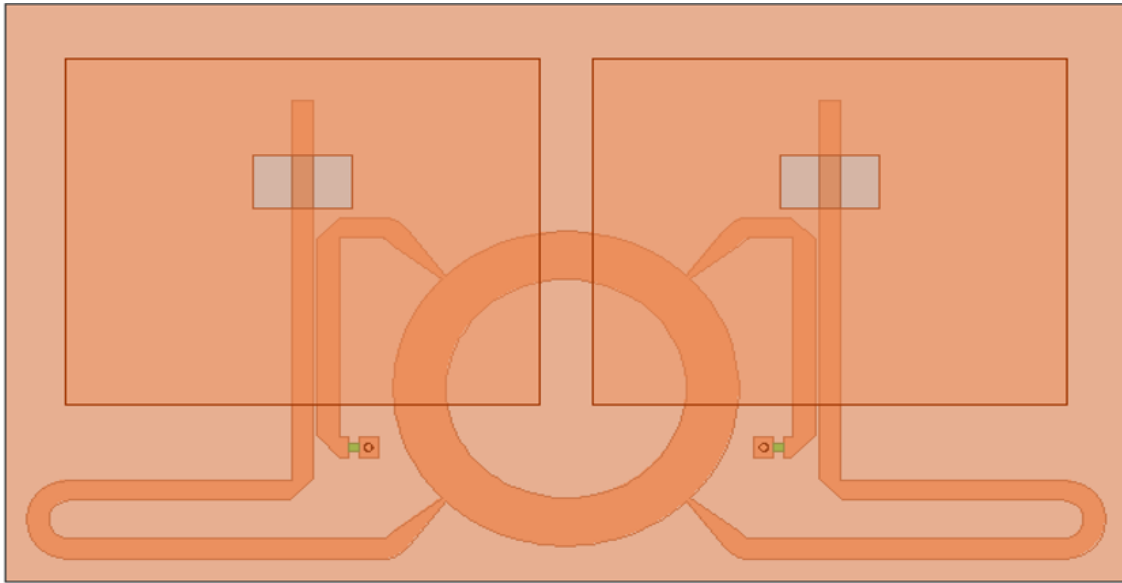


Figure 38 A 3D transparent layout of the retrodirective array designed in the HFSS.

This work demonstrates the preliminary mobile platform application for signal relay between two stations based on the Van Atta array structure. In Section 5.2, the components and functions used for the retrodirective array system are elaborated on. Section 5.3 discusses the theory and radiation pattern of the array. Section 5.4 describes the experiment setup and provides the simulated results. Section 5.5 contains the summary and the conclusion.

5.2. Retrodirective Array Prototype Overview

The geometry and system block diagram of the retrodirective array is shown in Fig. 39. In order to have the capability to integrate with other active/directional devices, ferrite circulators are necessary to separate the interchange signals. Limited by the low-profile constraint, an interchangeable traffic routing network between two patch antennas

was constructed by adopting two directional couplers, two delay-line phase shifters, and one crossover ring. Without using ferrite circulators greatly alleviates the fabrication complexity, the total cost, and magnetic fields shielding necessity.

The incoming signals first captured by the patch antennas are fed into the directional couplers. The majority of signals go into and out of the through line, and a portion of the signals are induced and leave the couple line. Because the traffic routing network has the symmetry property, two divided signals are recombined again on the other paired directional coupler.

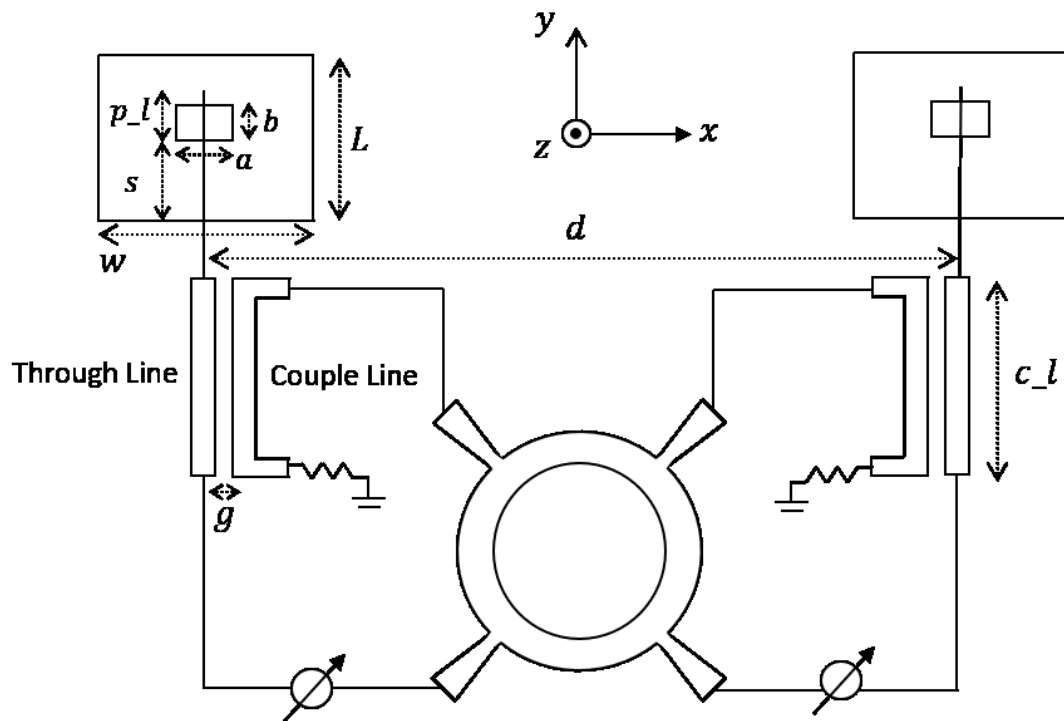


Figure 39 A geometry and system block diagram of the retrodirective array prototype.

Two aperture-coupled patches have spacing d of 54 mm, which is equivalent to $0.44 \lambda_0$ (λ_0 is free space wavelength at 2.42 GHz). The following are the reasons to adopt the aperture-coupled feed rather than the edge feed microstrip patch antennas. First, using aperture-coupled feed significantly decreases the total design areas. In fact, the signal routing network circuitry shares the common ground plane with the patch antennas, and therefore, the scattered fields from the ground plane are minimized.

Second, due to the isolation of the ground plane, the coupling between the patch antennas on the top side and the microwave circuitry on the bottom side is reduced. An edge feed and an aperture-coupled feed patch design are compared and shown in Fig. 40. On the whole, the aperture-coupled patch retrodirective array ($7.475 \times 10^{-3} \text{ m}^2$) reduces the substrate areas by 43.37%, comparing to the edge feed patch array ($13.2 \times 10^{-3} \text{ m}^2$).

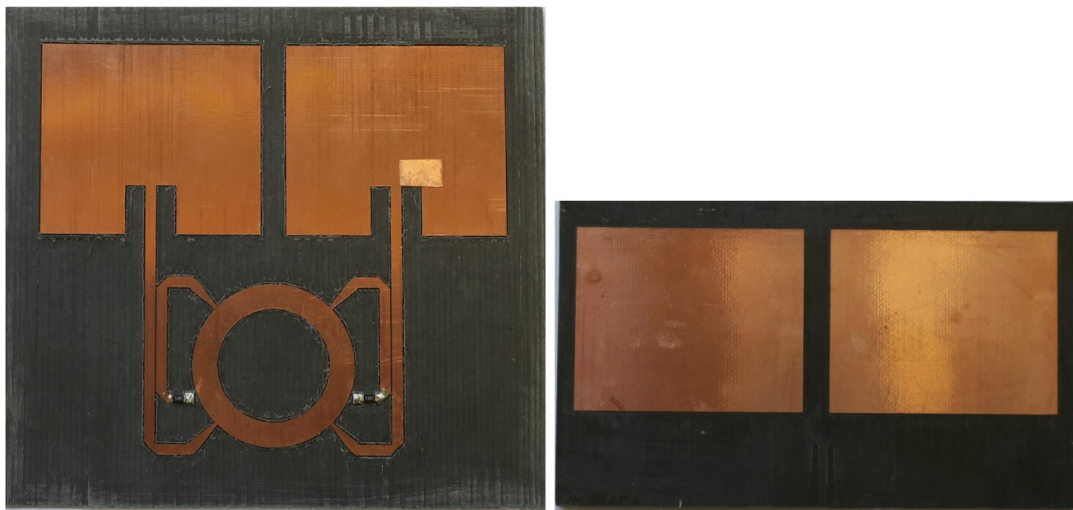


Figure 40 Photographs of the edge feed patch (left; $L \times W = 120 \text{ mm} \times 110 \text{ mm}$) and the aperture-coupled feed patch (right; $L \times W = 115 \text{ mm} \times 65 \text{ mm}$) retrodirective arrays.

5.2.1. Aperture-coupled Microstrip Patch Antenna

The aperture-coupled microstrip patch antenna acts as the received and re-transmit element and has linear-polarized characteristic. These antennas were fabricated on the 31 mil (0.787 mm) thick Duroid 5880 ($\epsilon_r = 2.2$) and had a width (w) of 48.4 mm and a resonant length (L) of 38.9 mm (physical aperture $A_p = 1.88 \times 10^{-3} \text{ m}^2$). The patch is fed through the longer edge (reversed feed), and a normal feed topology is compared to the reversed feed in Fig. 41. This reversed feed is designed on purpose to increase the overlapping areas with the routing circuitry on the bottom layer. More overlapping areas reduce substrate utilization and scattered fields from the ground plane. A tuning stub above the coupled slot has a length p_l of 12 mm and is added to match the impedance to 50Ω . The aperture has a length a of 10 mm and a width b of 6 mm and is placed at a distance (s) of 22.1 mm from the patch edge. For incident waves arriving at the patches, there is an additional 6.78° phase delay from the patch to the feed line (31 mil thick substrate).

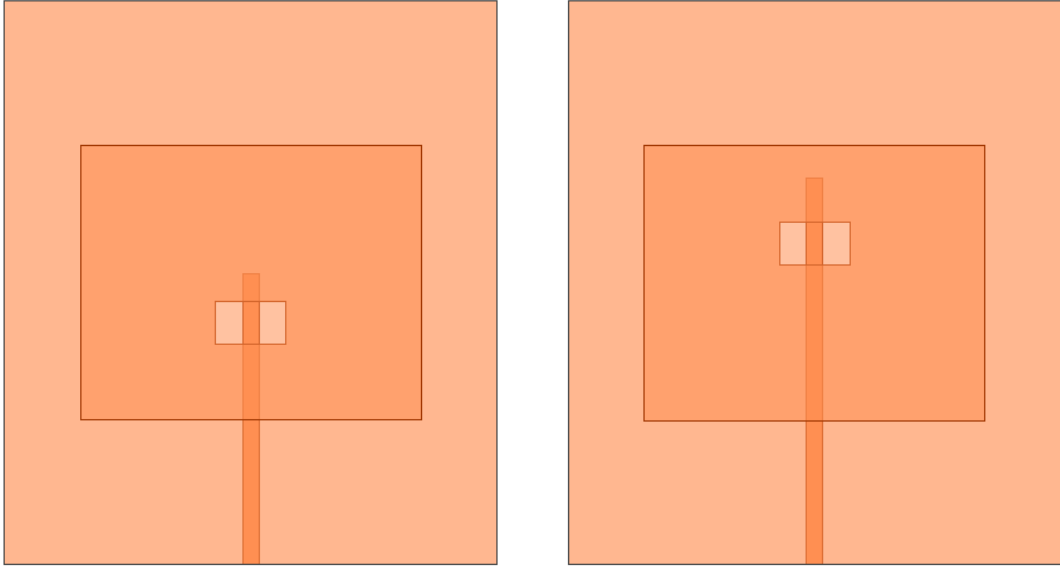


Figure 41 Aperture-coupled patch antennas with normal (left) and reversed (right) feed topology.

The patch antenna has $|S_{11}|$ equals to -29.51 dB (as shown in Fig. 42) at 2.42 GHz. Fig. 43 shows the simulated radiation pattern at 2.42 GHz for the two cut-planes (E-Plane and H-Plane). The antenna has a maximum gain G of 6.9 dB and a HPBW of $HPBW_{\theta} = 74^{\circ}$. The effective aperture (A_e) at $(\theta, \phi) = (0^{\circ}, 0^{\circ})$ is calculated by

$$A_e = \frac{\lambda_0^2}{4\pi} G = 5.98 \times 10^{-3} (m^2). \quad (15)$$

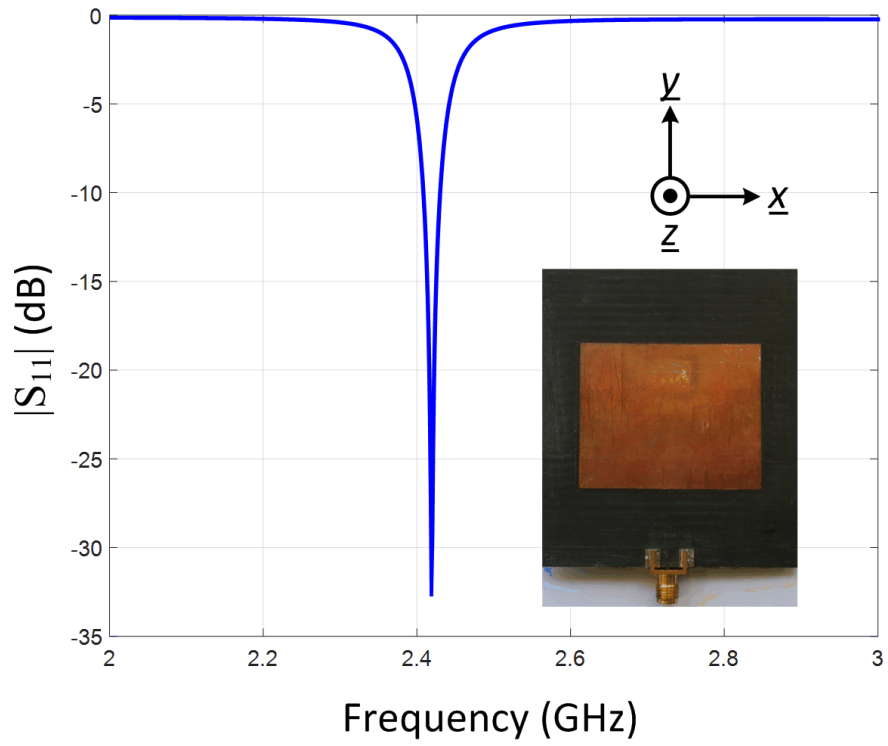


Figure 42 Simulated $|S_{11}|$ of the aperture-coupled microstrip patch.

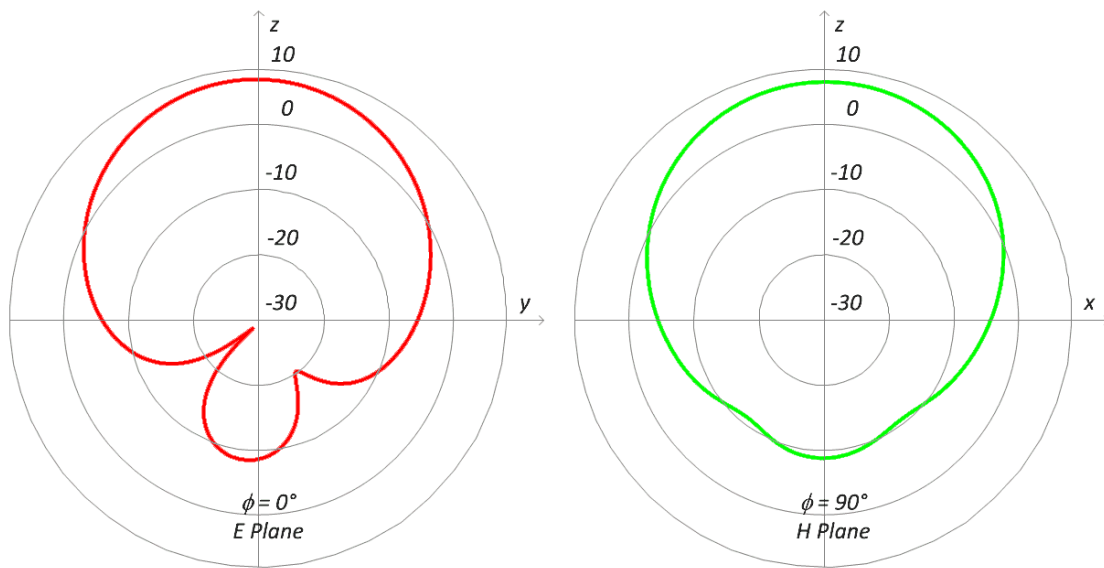


Figure 43 Simulated radiation pattern (dB) of the microstrip patch.

5.2.2. Directional Coupler

The directional coupler in Fig. 44 acts as a key component in achieving the traffic interchange between the incoming and outgoing signals. Also, the receiving and retransmitting signals are separated and recombined in this component. A gap (g) of 1 mm (between the through line and the coupled line) and a coupling length (c_l ; approximately $0.25 \lambda_g$, λ_g is the guided wavelength on the 31 mil Duroid 5880 substrate at 2.42 GHz) of 22.4 mm are designed to realize a 26.19 dB coupling factor ($S_{31} = -13.1$ dB) and 0.55 dB insertion loss ($S_{21} = -0.28$ dB) at 2.42 GHz (results are displayed in Fig. 45). The isolated port is connected to a 50 Ω SMD resistor to terminate the excess signals. Using the directional coupler to replace the ferrite circulator greatly reduces the circuit fabrication complexity and the requirements of the magnetic shielding. Although there is a coupling power loss between the through line and the couple line, the signal power can be reimbursed by adding additional low noise amplifiers (LNAs).

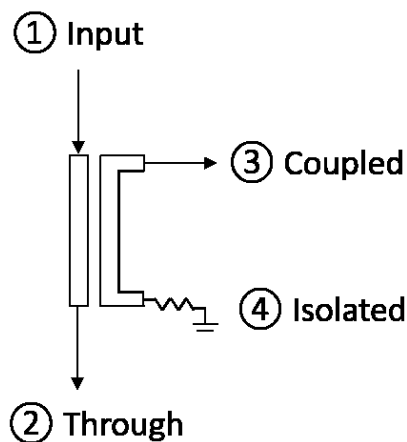


Figure 44 Geometry of the directional coupler.

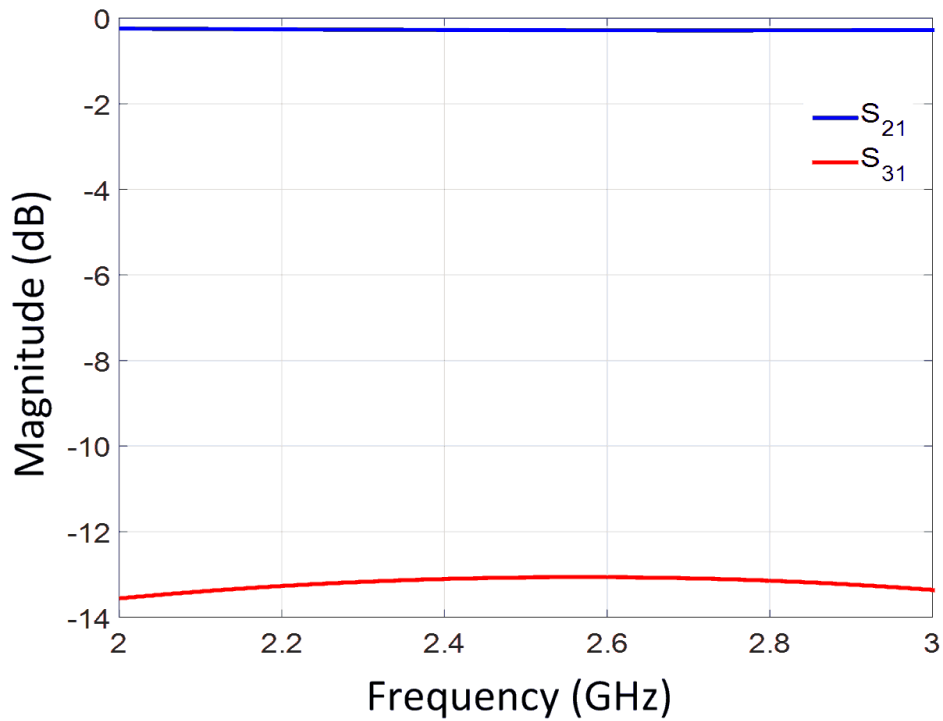


Figure 45 Simulated S_{21} and S_{31} of the directional coupler.

5.2.3. Crossover Ring

The crossover ring is designed to enable the cross-signal interchange within one planar surface when the crossing between two lines is inevitable. There are other methods, such as trace routing, wire bonding [43], air bridges [44, 45], wired via [46], and change layers [47], which can deal with the cross-traffic dilemmas; however, they all increase the fabrication complexity. Another advantage of the crossover ring is the symmetry property, so the interchange signals have the same path length which is important from a system's point of view.

A crossover ring geometry was designed and shown in Fig. 46. When signals input from port #1, the in-phase signals recombine at port #3, which is designated as the output port. On the other hand, port #2 and #4 are the isolation ports. The signals arrive at the isolation port would cancel each other because the recombining signals are out of phase.

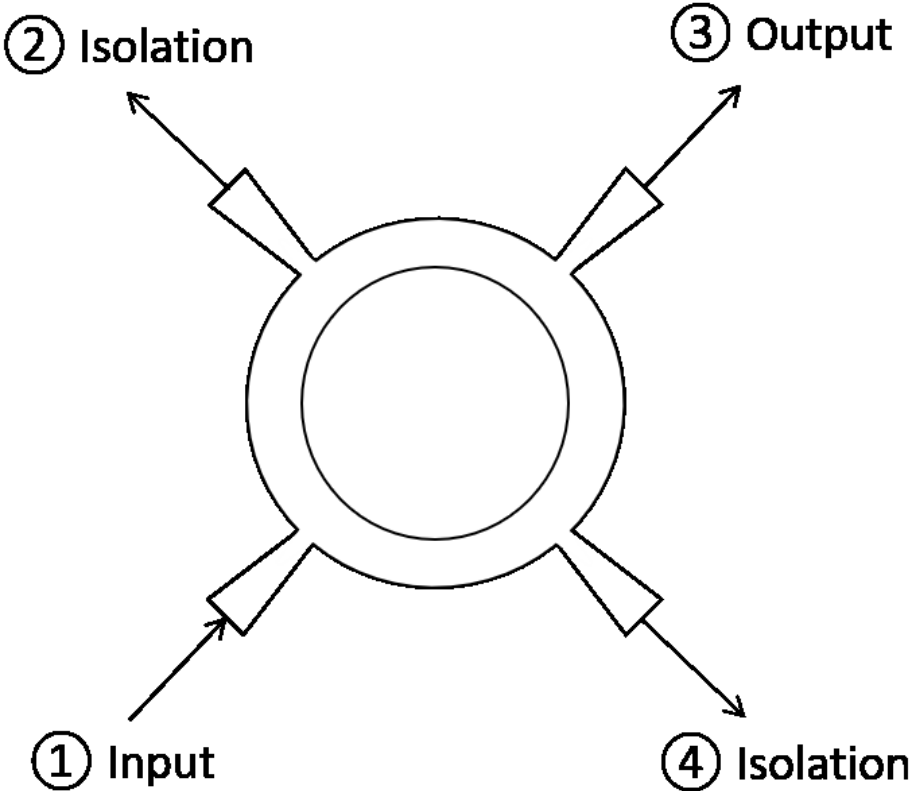


Figure 46 Geometry of the crossover ring structure.

The ring structure has inner radius of $r_{in} = 12.3$ mm and outer radius of $r_{out} = 17.7$ mm. The ports are distributed equally around the four corners (top-left, top-right, bottom-

left, and bottom-right) of the ring structure, and the length between each port is optimized to 90° electrical length at 2.42 GHz. As a result, the crossover ring provides a 26.18 dB isolation ($S_{41} = -13.09$ dB) and a 1.26 dB insertion loss ($S_{31} = -0.63$ dB) at 2.42 GHz (as shown in Fig. 47). From the system's perspective, high isolation characteristic is important because it guarantees that the signals go to the correct direction.

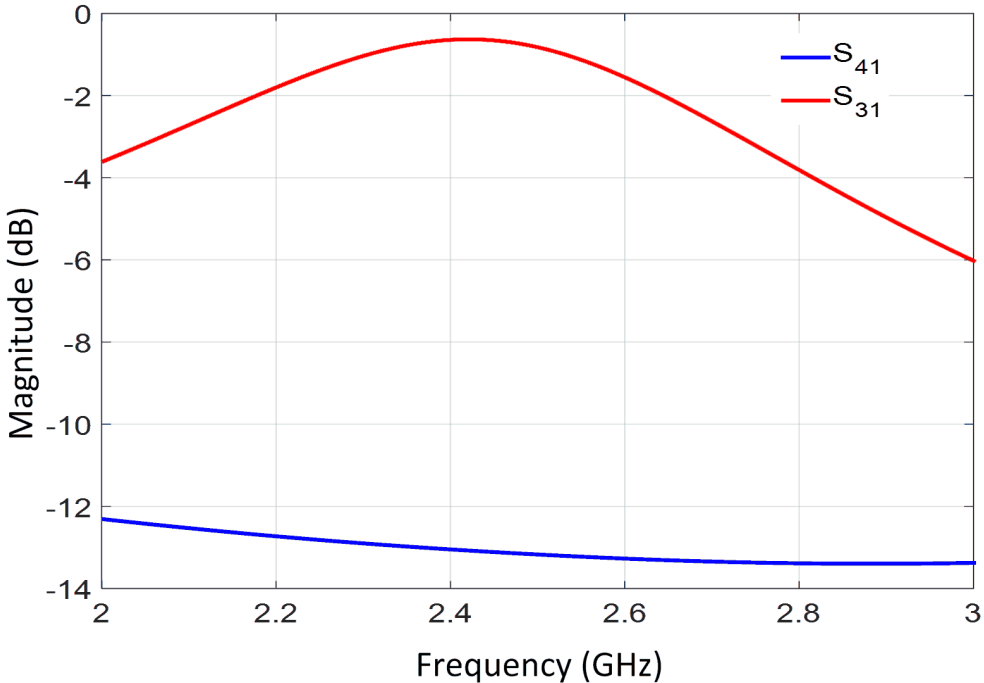


Figure 47 Simulated S_{41} and S_{31} of the crossover ring.

5.2.4. Delay Line Phase Shifter

For the phased array application, the easiest way to drive the main beam is to add

a phase shifter on each channel and provide the corresponding phase difference according to the scan angle. For the purpose of demonstration, a delay line phase shift is applied to emulate a phase shifter. The delay line phase shifter has two purposes in this work. For the retrodirective array prototype, the delay lines are used to make the reradiated and scattered fields in phase. For the relay system shown in Fig. 48, the delay lines give rise to the phase differences between two channels, and the incoming signals at array broadside ($\theta_i, \phi_i = 0^\circ$) are reradiated back to the reflection direction (θ_r), which is 30° in this case. Both θ_i and θ_r are the angles related to the z-axis. Since the array elements have spacing d of 54 mm ($0.44 \lambda_0$), the required phase is obtained by

$$\psi = \beta d \cdot \sin\theta_r + \alpha, \quad (16)$$

where β is the phase constant of the free space, and α is the applied delay line phase shift. To make $\theta_r = -30^\circ$, α is calculated to be 79.2° , which is equivalent to 19.94 mm electrical length. Note that the reflection angles vary according to different incident angles (as summarized in Table 2), which is further investigated in the pattern analysis section.

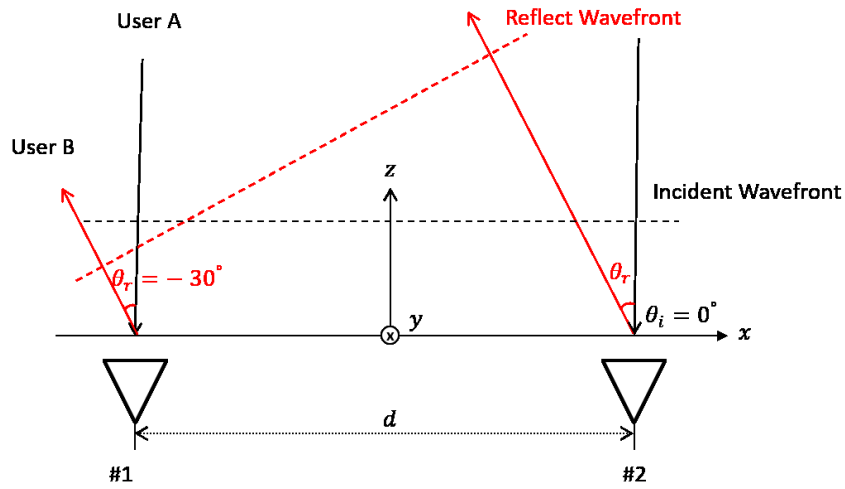


Figure 48 Illustration of a plane wave ($\theta_i, \phi_i = 0^\circ$) incidents on the relay system.

Table 2 - Phases at each antenna element of different plane wave incident and main beam reflection angles for the two delay line phase shifters with 19.94 mm length difference

Incident Angle ($\theta_i, \phi_i = 0^\circ$)	Incident Phase #1	Incident Phase #2	Reflection Angle (θ_r)	Reflect Phase #1	Reflect Phase #2
0°	0°	0°	-30°	-180°	-100.8°
-5°	-6.83°	6.83°	-24.7°	-173.17°	-107.63°
-10°	-13.62°	13.62°	-19.35°	-166.38°	-114.42°
-15°	-20.29°	20.29°	-14.25°	-159.71°	-121.09°
-20°	-26.82°	26.82°	-9.38°	-153.18°	-127.62°
-25°	-33.14°	33.14°	-4.73°	-146.86°	-133.94°
-30°	-39.2°	39.2°	0°	-140.79°	-140°

5.3. Array Radiation Pattern Analysis

When an incident wave arrives at a metal plate, three waves are generated. They are scattered waves from the metal plane (assume PEC material), diffraction waves from the edges, and surface waves traveling along the surface. In this work, the edges diffraction and traveling surface waves are assumed small and excluded. As a result, the total radiation pattern for this retrodirective array is the summation of the scattered field from the metal ground plane and the reradiated field from the patch antennas.

5.3.1. Geometrical Optics Analysis

To make the radiation pattern have maximum gain at array broadside, it is imperative to make the scattered fields and the reradiated fields in phase. The geometrical optics (GO) ray tracing technique is adopted here to analyze the E-fields between each boundary. For an arbitrary incident wave (\overline{E}^i), the fields are decomposed into parallel ($\overline{E}_{\parallel}^i$) and perpendicular (\overline{E}_{\perp}^i) components. In this case, only parallel (TM) polarized plane wave is investigated, and the E-fields among different interfaces are shown in Fig. 49.

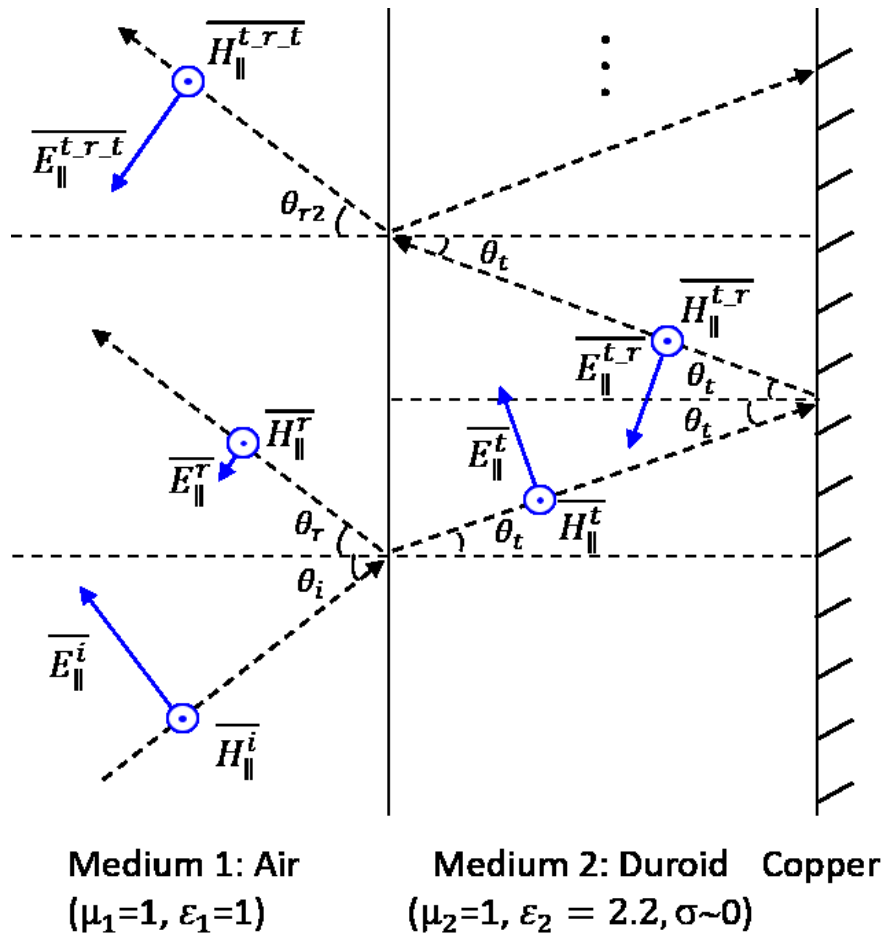


Figure 49 Parallel polarized plane wave reflects and refracts between boundaries.

As TM polarized plane waves first arrive at the array substrate, the waves within the effective aperture of the patch antennas are all extracted (as calculated $A_e \gg A_p$). For waves outside the effective aperture, a small portion of them reflects back to air ($\overline{E}_{\parallel}^r$), and the majority ($\overline{E}_{\parallel}^t$) refracts into the substrate. The reflection coefficient (Γ) and transmission coefficient (τ) depend on the incident angle (θ_i), the reflection angle (θ_r), the refraction

angle (θ_t), and the material property (μ , ϵ , and σ). For the known incident angle with the specular surface, the reflection and refraction angles are estimated by

$$\sqrt{\mu_1 \epsilon_1} \sin \theta_i = \sqrt{\mu_1 \epsilon_1} \sin \theta_r = \sqrt{\mu_2 \epsilon_2} \sin \theta_t. \quad (17)$$

The amplitudes of E_{\parallel}^r and $E_{\parallel}^{t,r-t}$ fields are expressed as

$$E_{\parallel}^r = \Gamma_{\parallel} E_{\parallel}^i = \frac{\eta_2 \cos \theta_t - \eta_1 \cos \theta_i}{\eta_2 \cos \theta_t + \eta_1 \cos \theta_i} E_{\parallel}^i, \text{ and} \quad (18)$$

$$E_{\parallel}^{t,r-t} = \tau_{\parallel 2,1} \Gamma_{\parallel copper} \tau_{\parallel 1,2} E_{\parallel}^i = \frac{2\eta_1 \cos \theta_t}{\eta_1 \cos \theta_r + \eta_2 \cos \theta_t} \cdot -1 \cdot \frac{2\eta_2 \cos \theta_i}{\eta_2 \cos \theta_t + \eta_1 \cos \theta_i} E_{\parallel}^i, \quad (19)$$

where $\tau_{\parallel 1,2}$ is the transmission coefficient from medium 1 to medium 2, $\Gamma_{\parallel copper}$ is the reflection coefficient from medium 2 to copper, which is -1 (intrinsic impedance of copper $\eta_{copper} \approx 0$) in this case, and $\tau_{\parallel 2,1}$ is the transmission coefficient from medium 2 to medium

1. For various incident angles, the corresponding θ_r , θ_t , E_{\parallel}^r , and $E_{\parallel}^{t,r-t}$ are summarized in Table 3. The 3rd or higher order reflections in medium 2 are assumed small and ignored.

Table 3 - The corresponding θ_r , θ_t , and electric fields with the known incident angles

Incident Angle (θ_i)	Reflection Angle (θ_r)	Refraction Angle (θ_t)	E_{\parallel}^r	$E_{\parallel}^{t,r-t}$
0°	0°	0°	-0.1946	-0.9621
10°	10°	6.72°	-0.1906	-0.9637
20°	20°	13.33°	-0.1778	-0.97
30°	30°	19.7°	-0.15	-0.9684
40°	40°	25.68°	-0.1153	-0.9867

The refract waves ($\overline{E_{\parallel}^t}$) impinged on the copper plate are totally reflected back, and the scattered fields are derived by using the radiation integral. Since there is no field inside the conductor, the scattered E-field vector ($\overline{E_{\parallel}^{t-r}}$) is exactly the same as the incident field ($\overline{E_{\parallel}^t}$) in amplitudes but 180° out of phase. Note that the final waves ($\overline{E_{\parallel}^{t-r-t}}$) scattered out of the array substrate have an additional phase change from the ground plane and the substrate. The phase change from the substrate is called the round-trip substrate phase, and it is expressed as $2\beta_s \cdot h \cdot \sec \theta$, where β_s is the phase constant of the substrate and h is the thickness of the substrate. For thin substrate with normal incidence, the round-trip substrate phase is close to 0°. Table 4 shows round-trip substrate phases with different refraction angles.

Table 4 - Round-trip phase delay of the wave propagating along the substrate (31 mil thickness) with different refraction angles

Refraction Angle (θ_t, ϕ_t)	Round-trip Substrate Phase
(0°,0°)	6.78°
(10°,0°)	6.89°
(45°,0°)	9.59°
(70°,0°)	19.84°
(80°,0°)	39.07°

In contrast to the reradiated E-field from the patch antennas, the phase changes only come from the contribution of the traffic routing network path delay (l). In conclusion, to make the reradiated and scattered fields in phase (0° phase difference) at array broadside, it is necessary to maintain the traffic routing network that has electrical path length approximated to $n \cdot \lambda_g$, ($n = 1, 2, 3, \dots$). Note that an additional phase change from the directional coupler has to add back in. If the reradiated and scattered fields are not in phase, the destructive interference would occur, and in [39] the comparisons of different out of phase results are provided.

5.3.2. Scattered Field

The incident waves impinged on the metal plate are reflected back, and the whole scattered fields are derived by integrating currents over the illuminated surface. One quantity used to describe the strength of the scattered field is the RCS, and it is defined as

$$\sigma = \lim_{R \rightarrow \infty} 4\pi R^2 \frac{|\bar{E}_s|^2}{|\bar{E}_i|^2} (m^2), \quad (20)$$

where \bar{E}_s is the scattered electric field at the receiver, and \bar{E}_i is the electric field of the plane wave incidents on the target. One property of the RCS is its range independence; however, it is still frequency dependent. The flat surface RCS [48] of normal incidence gives

$$\sigma = \frac{4\pi A^2}{\lambda_0^2} (m^2), \quad (21)$$

where A is the physical area. In this work, the RCS of a rectangular metal plate ($A = L \times W = 115 \times 65 \text{ mm}^2$), which has the same dimension as the retrodirective array is calculated to have RCS of $4.56 \times 10^{-2} (m^2) = -13.4 \text{ dBsm}$.

5.3.3. Reradiated Field

The reradiated pattern $F(\theta, \phi)$ of the two-element retrodirective array is estimated by pattern multiplication method, where $AF(\theta, \phi)$ is the array pattern with each antenna element substituted by an isotropic source. The element pattern $EP(\theta, \phi)$ is the single antenna pattern placed at the origin. In Fig. 50, the locations of the array elements are designated as $P_n(x_n, y_n, z_n)$, where $n = 1, 2$; the location of the observer is defined as $R(r, \theta, \phi)$. In the far-field, $\overline{P_n R}$ is approximately parallel to \overline{OR} , where O is the origin.

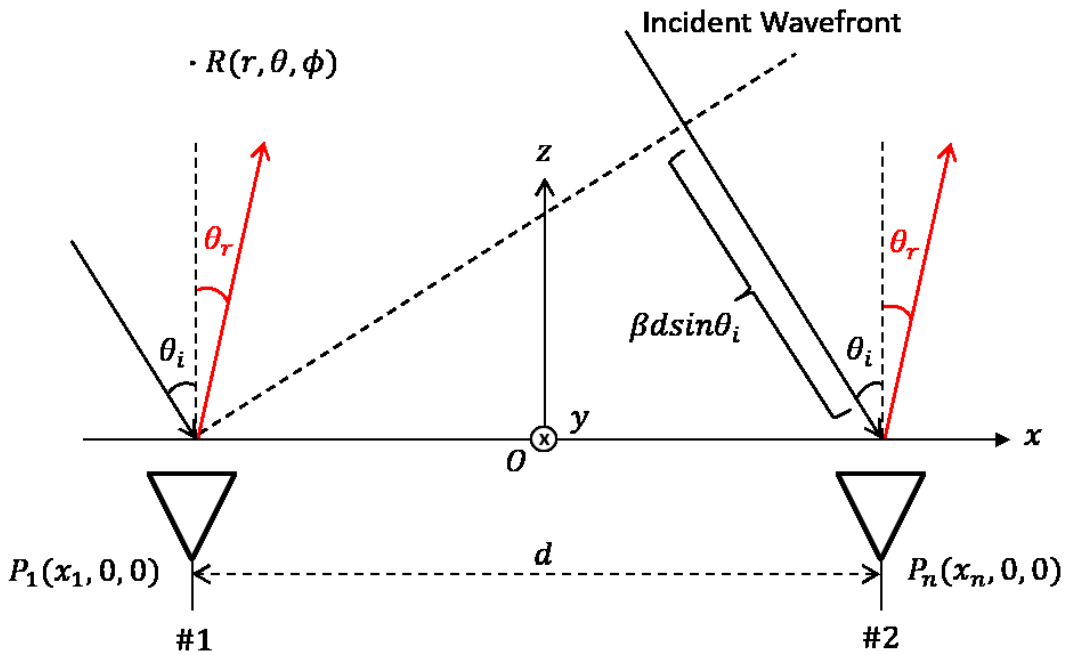


Figure 50 Two-element retrodirective array positioned along the x-axis ($\phi_i = 0^\circ$).

5.4. Experiment and Results

Two experiments were conducted in this section. First, the retrodirective array prototype acted as the Van Atta array structure is investigated. Second, a phase difference adds on the array prototype to make it becomes a signal relay system, and the phase difference is created by changing the length of the delay line phase shifter. The ultimate goal was to relay signals between 0° and 30° . The retrodirective is placed on the x-y plane and is facing the z-axis.

5.4.1. Retrodirective Array Prototype

The retrodirective array prototype with 0° phase difference between interchange channels is demonstrated and evaluated in this section. The total radiation pattern from the prototype is the summation of all the reflected waves, such as reradiated fields and scattered fields. It is favorable to understand the contribution of each individual field; therefore, a method of estimation is designed to provide more detailed information.

For scattered fields estimation, two patch antennas from the prototype are terminated to the ground plane, and a plane wave excitation acts as the signal source. Thus, the radiation pattern mainly comes from the scattered fields of the ground plane area, which is defined as the scattered plate. This method provides a more accurate estimation rather than measuring the scattered field from a metal plate.

For reradiated fields estimation, the reradiated fields are the radiation pattern of two patch antennas fed with conjugate phases from the incident waves. This method can provide the shape of the pattern, but not the amplitudes. Thus, the reradiated field pattern

(patch array radiation pattern) is normalized to the scattered plate for the purpose of comparison.

5.4.2. Radiation Pattern of the Retrodirective Array Prototype

The first experiment demonstrates that the bistatic RCS (the transmitter and the receiver are not the same) of a normal plane wave ($\theta_i = 0^\circ$, $\phi_i = 0^\circ$) impinges on a retrodirective array prototype with traffic routing network path length (l) of -720° (minus sign means the phase delay), which is the in-phase case. The in-phase case means that the scattered field and the reradiated field are added constructively, and therefore, a maximum RCS from the reflected waves is expected.

The bistatic RCSs of a metal plate ($L \times W = 115 \text{ mm} \times 65 \text{ mm}$), the scattered plate ($L \times W = 115 \text{ mm} \times 65 \text{ mm}$), the retrodirective array ($L \times W = 150 \text{ mm} \times 65 \text{ mm}$), as well as the radiation pattern from the patch array are simulated and displayed in Fig. 51. The maximum bistatic RCS of the retrodirective array and the scattered plate are both at array broadside and equal to -17.73 dBsm and -28.34 dBsm , respectively. Considering the A_e of a single patch antenna at $(\theta, \phi) = (0^\circ, 0^\circ)$ is $5.98 \times 10^{-3} \text{ (m}^2\text{)}$, where the total area of the retrodirective array is $7.475 \times 10^{-3} \text{ (m}^2\text{)}$; therefore, the total reflected field that can be deferred majorly comes from the reradiated field. Moreover, the RCS of the retrodirective array pattern is close to the patch array pattern. Likewise, the bistatic RCS of the metal plate is -9.73 dBsm , which is 18.61 dBsm higher than the RCS of the scattered plate, and it verifies that the primary incident waves are captured by the patch array. A metal plate acts as a reference, and it is considered as the maximum RCS. The retrodirective array prototype has a lower RCS than the metal plate because of the loss from the traffic routing

network and the phase nonideality. The phase nonideality is due to the higher order internal reflection, and it results in destructive interference among the reflected waves.

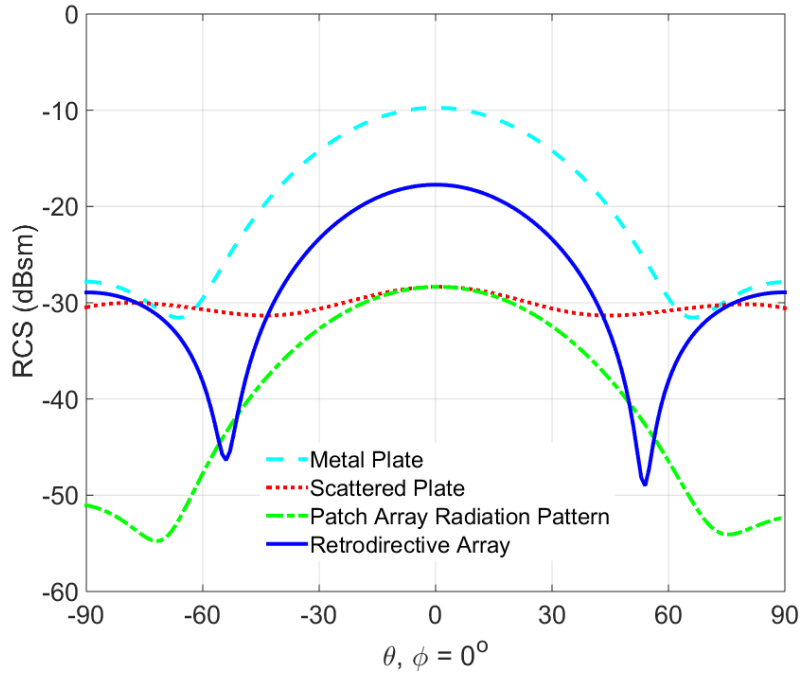


Figure 51 Simulated bistatic RCSs (normal incidence) of a metal plate, the scattered plate, the retrodirective array ($l = -720^\circ$), and a normalized patch array radiation pattern.

The second experiment indicates that the bistatic RCS of a normal plane wave ($\theta_i = 0^\circ, \phi_i = 0^\circ$) impinges on a retrodirective array prototype with traffic routing network path length (l) of -900° , which is the out-of-phase case. The out-of-phase case means that the scattered field and the reradiated field are added destructively, and therefore, a

minimum reflected RCS is expected. After all, the reradiated waves have 180° phase difference compared to the scattered waves.

The bistatic RCSs of a metal plate ($L \times W = 140 \text{ mm} \times 65 \text{ mm}$), the scattered plate ($L \times W = 140 \text{ mm} \times 65 \text{ mm}$), the retrodirective array ($L \times W = 140 \text{ mm} \times 65 \text{ mm}$), as well as the radiation pattern from the patch array are simulated and displayed in Fig. 52. The maximum bistatic RCS of the scattered plate and the metal plate are both equal to -20.18 dBsm and -8.21 dBsm at $(\theta, \phi) = (0^\circ, 0^\circ)$, respectively. On the contrary, the retrodirective array has minimum bistatic RCS of -33.74 dBsm at $(\theta, \phi) = (0^\circ, 0^\circ)$. This result shows that the scattered and reradiated fields are added destructively at array broadside, and the cancellation effect starts to deteriorate when the array scans away from $(\theta, \phi) = (0^\circ, 0^\circ)$. Comparing the out-of-phase design with the in-phase design, a 16.01 dBsm RCS difference is recorded. This experiment provides a clear understanding of the importance of the in-phase retrodirective array design.

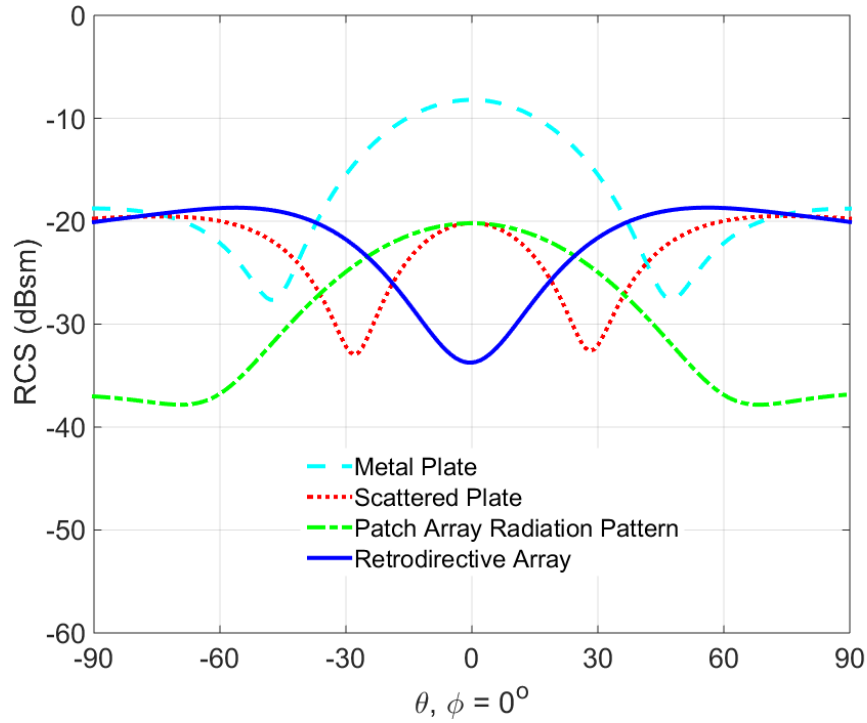


Figure 52 Simulated bistatic RCSs (normal incidence) of a metal plate, the scattered plate, the retrodirective array ($l = -90^\circ$), and a normalized patch array radiation pattern.

The third experiment uses that the bistatic RCS of an oblique plane wave ($\theta_i = 45^\circ$, $\phi_i = 270^\circ$) impinges on a retrodirective array prototype with traffic routing network path length (l) of -720° , which is the in-phase case. The bistatic RCSs of a metal plate ($L \times W = 115 \text{ mm} \times 65 \text{ mm}$), the scattered plate ($L \times W = 115 \text{ mm} \times 65 \text{ mm}$), the retrodirective array ($L \times W = 115 \text{ mm} \times 65 \text{ mm}$), as well as the radiation pattern from the patch array are simulated and displayed in Fig. 53. The maximum bistatic RCS of the scattered plate and the metal plate are -27.08 dBsm and -14.11 dBsm at $(\theta, \phi) = (0^\circ, 0^\circ)$, respectively. Similarly, the maximum bistatic RCS of the retrodirective array is -25.38 dBsm at $(\theta, \phi) =$

$(0^\circ, 0^\circ)$, which is 7.65 dBsm lower than the normal incidence. The RCS reduction from the oblique incidence can be explained as follows.

First, when a plane wave obliquely arrives upon a specular surface, the incident waves should obey the Snell's law of reflection. If the incident angle of $\theta_i = 45^\circ$ and $\phi_i = 270^\circ$, the reflection angle would be $\theta_r = -45^\circ$ and $\phi_r = 270^\circ$, which is away from the observation angles ($-90^\circ \leq \theta \leq 90^\circ$, $\phi = 0^\circ$).

Second, the patch antenna has a smaller A_e and lower gain at oblique angle; therefore, less power can be collected and transmitted. In fact, the oblique incidence would create exponential power reduction to the retrodirective array.

Third, the round-trip substrate phases for radiated and scattered fields are different. When the incident angle increases, the phase difference from the round-trip substrate phases becomes larger as well. According to Table 3., a normal plane wave incidence would create 6.78° round-trip substrate phase for both reradiated and scattered fields; however, for $\theta_i = 45^\circ$, $\phi_i = 270^\circ$ incidence, the round-trip substrate phases for reradiated and scattered fields are 6.78° and 9.59° , respectively.

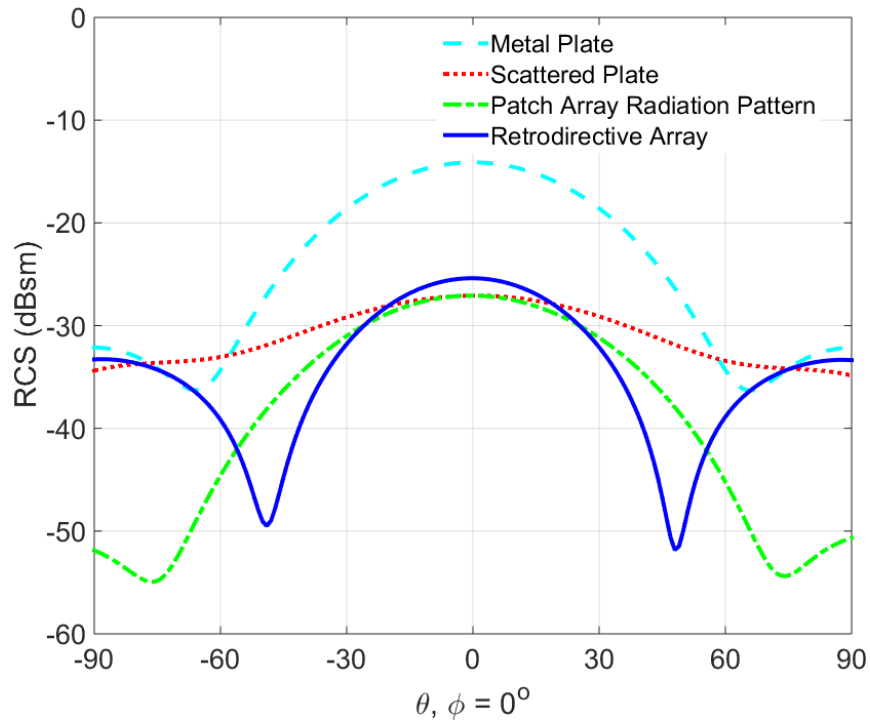


Figure 53 Simulated bistatic RCSs (oblique incidence) of a metal plate, the scattered plate, the retrodirective array ($l = -720^\circ$), and a normalized patch array radiation pattern.

The fourth experiment shows that the bistatic RCS of an oblique plane wave ($\theta_i = 45^\circ, \phi_i = 270^\circ$) impinges on a retrodirective array prototype with traffic routing network path length (l) of -900° , which is the out-of-phase case. The bistatic RCSs of a metal plate ($L \times W = 140 \text{ mm} \times 65 \text{ mm}$), the scattered plate ($L \times W = 140 \text{ mm} \times 65 \text{ mm}$), the retrodirective array ($L \times W = 140 \text{ mm} \times 65 \text{ mm}$), as well as the radiation pattern from the patch array are simulated and displayed in Fig. 54. The retrodirective array has a minimum RCS of -25.09 dBsm at $(\theta, \phi) = (0^\circ, 0^\circ)$.

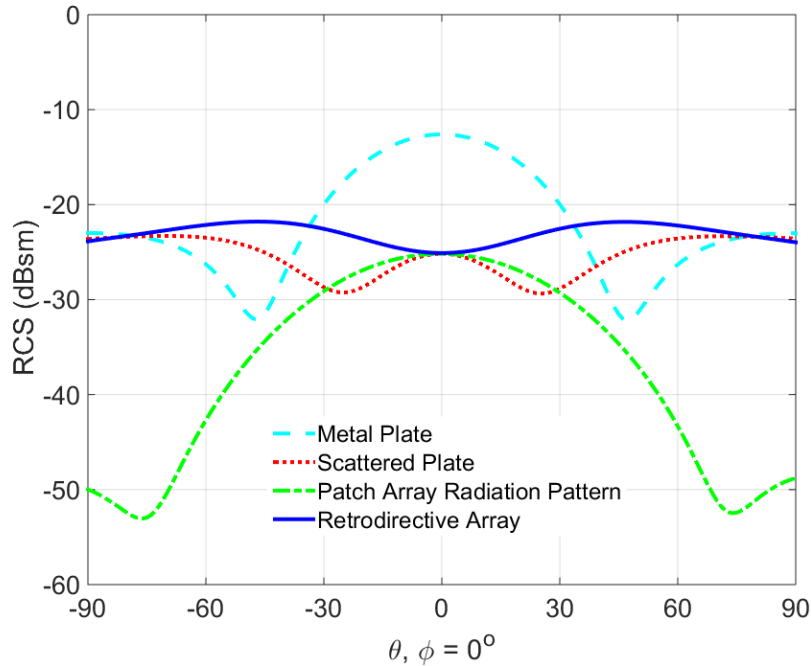


Figure 54 Simulated bistatic RCSs (oblique incidence) of a metal plate, the scattered plate, the retrodirective array ($l = -900^\circ$), and a normalized patch array radiation pattern.

In spite of the in-phase field consideration, another important functionality for the array prototype is to automatically reflect the incident waves back to the signal source without any prior knowledge of DOAs. Three different incident angles ($\theta_i = 0^\circ, 15^\circ, 30^\circ$ and $\phi_i = 0^\circ$) were examined to verify the capability. Fig. 55 shows the simulated bistatic RCSs from different incident angles. Even though the main beam does not have maximum RCS at the corresponding reflected angles, the main beam demonstrates the tendency that the scan angle shifts. For $\theta_i = 0^\circ, 15^\circ, 30^\circ$ and $\phi_i = 0^\circ$ incidences, the bistatic RCSs are -17.73 dBsm, -20.59 dBsm, and -25.8 dBsm, respectively. The RCS decreases as the incident angles are away from $(\theta, \phi) = (0^\circ, 0^\circ)$.

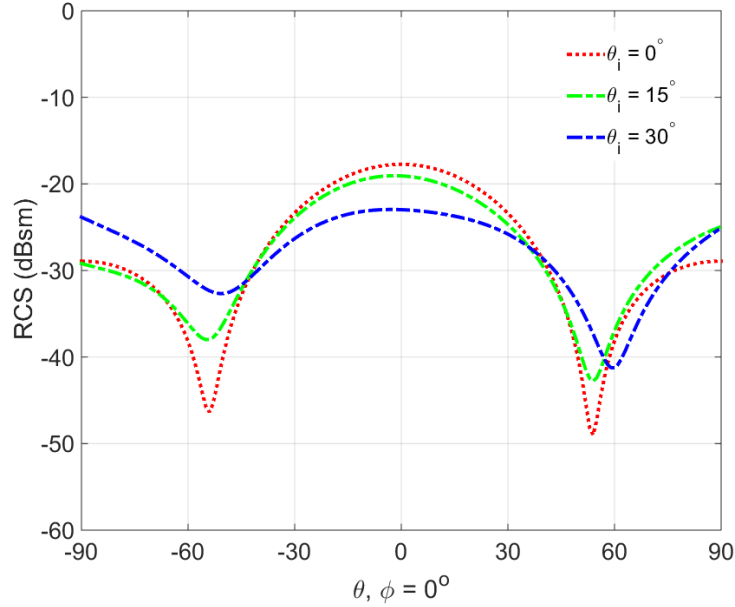


Figure 55 Simulated bistatic RCSs of the retrodirective array with oblique TM polarized plane wave incidence ($\theta_i = 0^\circ, 15^\circ, 30^\circ, \phi_i = 0^\circ; l = -720^\circ$).

On the other hand, another RCS representation uses the monostatic RCS; the monostatic means that the transmitter and the receiver are at the same angle. An experiment performs that the monostatic RCS of a normal plane wave ($-90^\circ \leq \theta_i \leq 90^\circ, \phi_i = 0^\circ$) impinges on a retrodirective array prototype with traffic routing network path length (l) of -720° , which is the in-phase case. The monostatic RCSs of a metal plate ($L \times W = 115 \text{ mm} \times 65 \text{ mm}$), the scattered plate ($L \times W = 115 \text{ mm} \times 65 \text{ mm}$), the retrodirective array ($L \times W = 115 \text{ mm} \times 65 \text{ mm}$), as well as the radiation pattern from the patch array are simulated and displayed in Fig. 56.

The maximum monostatic RCS of the retrodirective array and the metal plate are equal to -18.22 dBsm and -9.75 dBsm at $(\theta, \phi) = (0^\circ, 0^\circ)$, respectively. The scattered plate has a minimum RCS of -28.65 dB at $(\theta, \phi) = (0^\circ, 0^\circ)$. For the scattered plate, there is a notch around $(\theta, \phi) = (0^\circ, 0^\circ)$, which illustrates that the principal incident powers are absorbed by the patch array; therefore, only a few waves are scattered back.

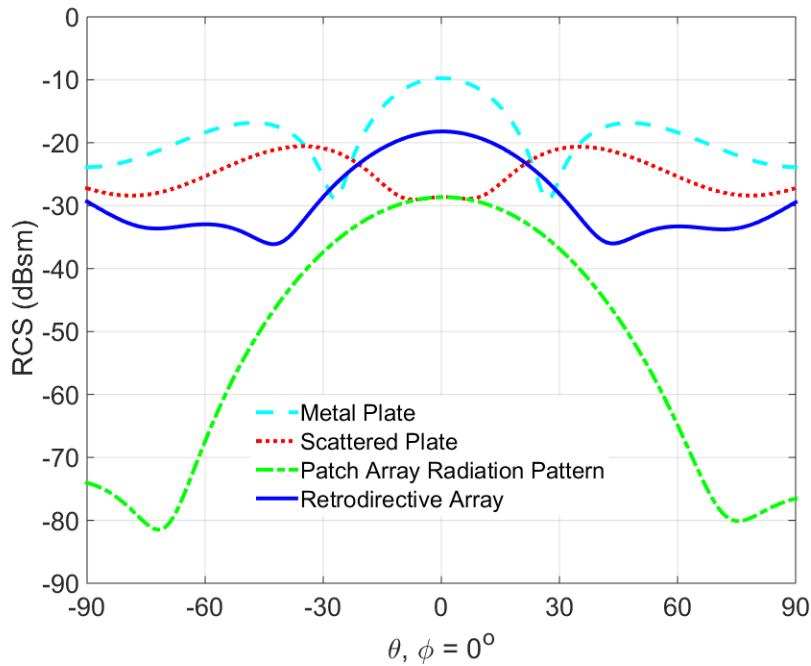


Figure 56 Simulated monostatic RCSs of a metal plate, the scattered plate, the retrodirective array ($l = -720^\circ$), and a normalized patch array radiation pattern.

In the same way, an experiment uses that the monostatic RCS of a normal plane wave ($-90^\circ \leq \theta_i \leq 90^\circ, \phi_i = 0^\circ$) impinges on a retrodirective array prototype with traffic

routing network path length (l) of -900° , which is the out-of-phase case. The monostatic RCSs of a metal plate ($L \times W = 140 \text{ mm} \times 65 \text{ mm}$), the scattered plate ($L \times W = 140 \text{ mm} \times 65 \text{ mm}$), the retrodirective array ($L \times W = 140 \text{ mm} \times 65 \text{ mm}$), as well as the radiation pattern from the patch array are simulated and displayed in Fig. 57.

The retrodirective array has a minimum RCS of -32.55 dBsm at $(\theta, \phi) = (0^\circ, 0^\circ)$. The metal plate has a maximum RCS of -8.23 dBsm at $(\theta, \phi) = (0^\circ, 0^\circ)$, and the scattered plate has a RCS of -20.39 dBsm at $(\theta, \phi) = (0^\circ, 0^\circ)$.

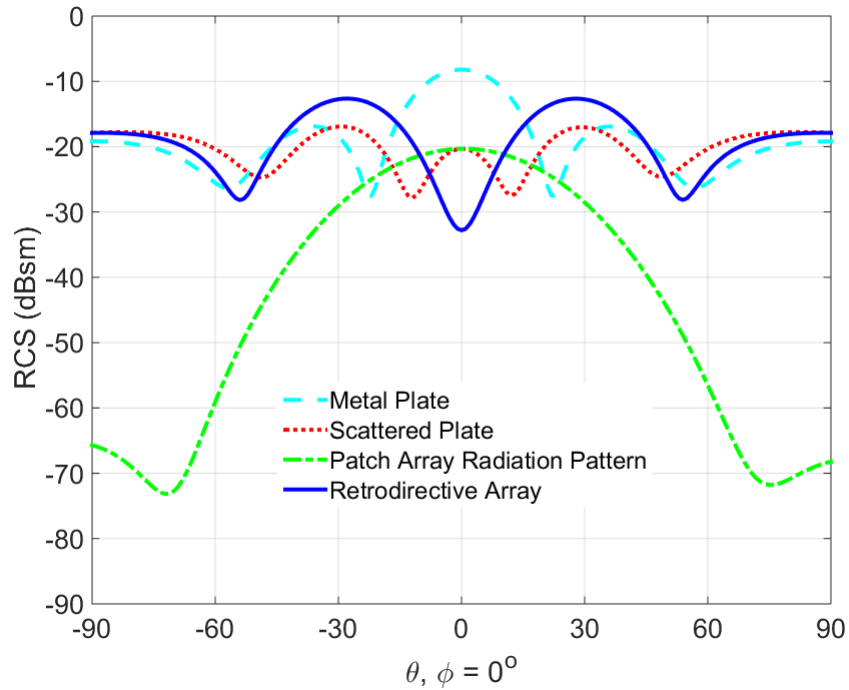


Figure 57 Simulated monostatic RCSs of a metal plate, the scattered plate, the retrodirective array ($l = -900^\circ$), and a normalized patch array radiation pattern.

5.4.3. Retrodirective Array as a Relay System

Up to now, the retrodirective array prototype has the same functionality as the conventional Van Atta array, and it can automatically reflect back the incoming signals to the signal source. Next, to facilitate a relay system with 30° relay angles, the prototype is modified to provide a 79.2° phase difference between two antennas. Therefore, a 19.94 mm path difference is applied by changing the length of the delay line phase shifter. On the other hand, the path difference between both of the delay line phase shifters would make the traffic routing network no longer maintain symmetry property. In general, the received signal from the patch antenna forwarded to the paired antenna cannot be recombined in phase. To solve the problem, a Qorvo SGA3486Z SiGE HBT MMIC amplifier [49] is added on each channel to not only boost the signal strength but also isolate the unwanted signals (22.2 dB reversed isolation @ 2.4 GHz) from the reversed direction. The broadband amplifier can provide DC to 5 GHz RF signals amplification. For this amplifier, one of the benefits is that its internal impedance matches to 50Ω . Adding the amplifier can greatly alleviate the loss from the direction coupler, and the scattered fields from the ground plane become much smaller compared to the amplified reradiated fields. Consequently, making the scattered and reradiated fields in phase is neglected. A modified retrodirective array was fabricated and shown in Fig. 58.

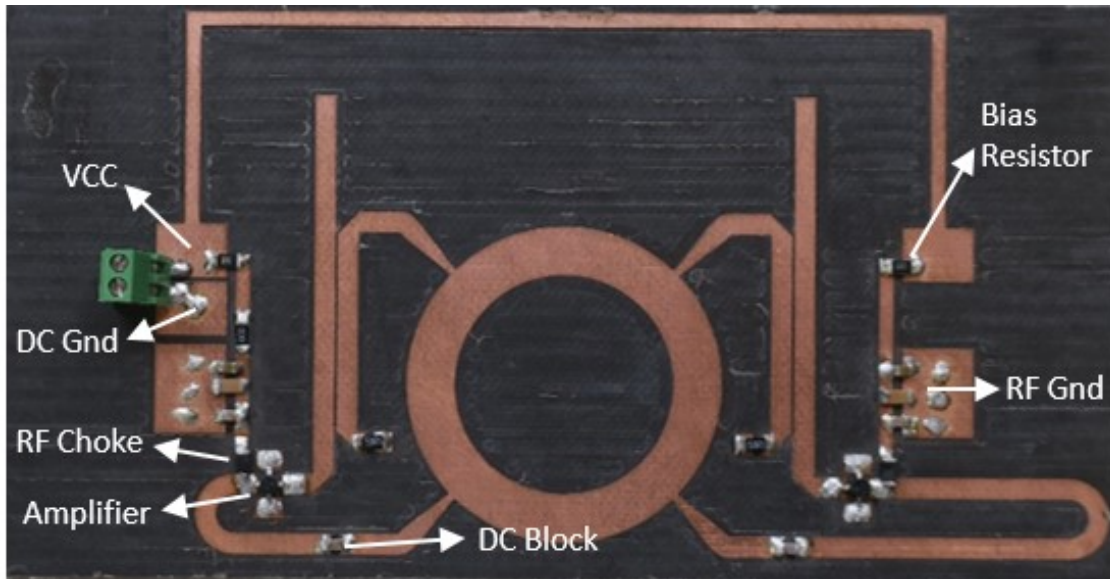


Figure 58 The retrodirective array relay system ($L \times W = 126 \text{ mm} \times 65 \text{ mm}$).

A 5V DC voltage is connected to the voltage at the common collector (VCC) pad to provide biased voltage for the amplifier, and a 68Ω bias resistor is connected to bring 35 mA operating current to the amplifier. Because the input and output impedance of the amplifier are 50Ω , no additional impedance matching network is added. With the proper setup, the amplifier is supposed to contribute typical 16.5 dB gain, 3.4 dB noise figure, 22.2 dB reverse isolation, 10.8 dB input return loss, and 16.1 dB output return loss at 2.4 GHz. An 18 nH SMD inductor acts as the RF choke, and two 56 pF capacitors are inserted as the DC block. Notice that the DC block only applies on one side of the amplifier. To diminish the RF leakage from the channels, 22 pF, 1 nF, and 1 μF capacitors are chosen to short the RF signals to the ground.

5.4.4. Radiation Pattern of the Relay System

The retrodirective array relay system is placed in the anechoic chamber to measure the bistatic gain of the reflected waves. A horn antenna provides a normal plane wave ($\theta_i = 0^\circ$, $\phi_i = 0^\circ$) incidence, and it is placed horizontally facing the retrodirective array relay system. To minimize the fields contributed from the unwanted horn antenna, absorbers are placed around it to minimize the backscatter fields. The measured reflected field together with the simulated two-element patch array radiation pattern are illustrated in Fig. 59. The measured pattern is normalized to the simulated one to make a comparison. Both of the fields have main beams around -30° , which shows good agreement with the full-wave simulations.

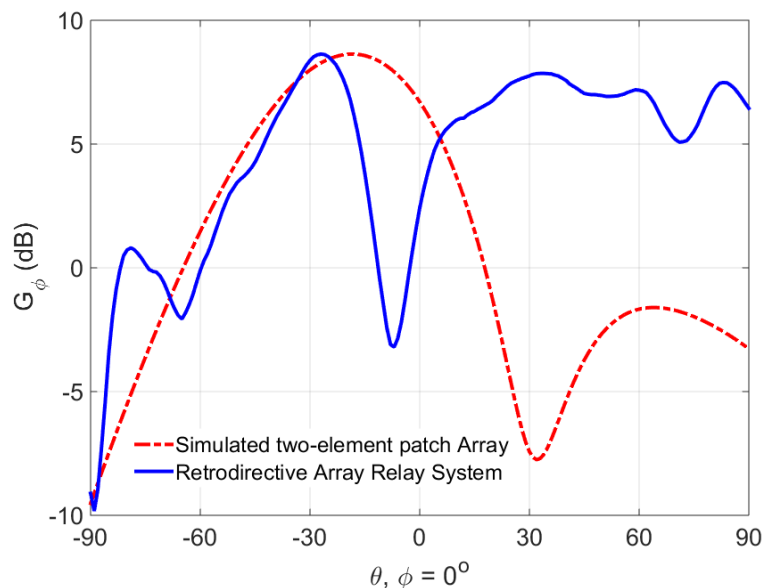


Figure 59 Measured bistatic radiation pattern of the retrodirective array relay system along with the simulated two-element patch array.

5.5. Conclusion

This work [50] successfully demonstrates a retrodirective array prototype based on the conventional Van Atta array structure along with a signal relay system modified from the retrodirective array prototype. The ferrite circulator is commonly found in these systems in terms of doing the duplex signal interchange and replaced by a traffic routing network to simplify the overall system design. This work clearly explains the constitution of the reflect waves, which is the combination of reradiated and scattered waves, and how to adjust the delay line phase shifter to make the reradiated and scattered fields in phase. Without carefully adjusting the phases [51], a destructive interference may occur and the notch may appear on the main beam. To sum up, the constructive or destructive interferences of the reradiated fields can be tuned by adjusting the phase shifter.

6. AN INVESTIGATION OF INDIRECT BEAMFORMING AND BEAMSHAPING IMPLEMENTED ON A SLOT ARRAY

6.1. Introduction

This project investigated both the indirect beamforming and beamshaping techniques implemented on a slot array with two hundred circular slots at 60 GHz. The goal was to generate a high gain radiation pattern with low SLL (especially for the sidelobes around the main beam) from a single plane wave excitation. A former work [52] demonstrated the process by using a single plane wave excitation impinges on a metal holey plate to create a -12.8 dB SLL radiation pattern. The holey plate was engraved with two hundred and ten circular slots with a uniform distribution over a circular aperture of 28λ in radius. Each circular slot has an equal radius of $\lambda/8$, and the radiation pattern was measured at 71.25 GHz.

This work inherited a major essence in [52], but we further examine the capabilities of beam scanning and beamshaping. First, circular slots of various slot apertures were implemented to distribute tapered electric fields, and then the beamshaping results were examined. Second, plane waves with different incident angles were conducted to investigate the beam scanning performance.

The reason to use two hundred circular slots instead of a two-hundred-element phased array is to reduce the array complexity and the total cost. One advantage of this topology is to create a high gain and a low SLL radiation pattern. Although there are

certain drawbacks in the use of a slot array, such as parts of the incident waves being reflected from the metal ground plane, the slot array is still superior due to the high gain and low-cost characteristics.

6.2. Array Overview

6.2.1. Metal Plate

A copper sheet was used as the ground plane of the slot array. As shown in Fig. 60 and Fig. 61, the metal plate was engraved with two hundred circular slots with a uniform distribution over a circular aperture of 15λ in radius, which equals 75 mm. Each slot aperture has the same radius of $\lambda/2$, and the radiation pattern was measured at 60 GHz. To measure the radiation pattern, a plane wave has to impinge on one side of the plate, and the incident waves reradiate on the other side. Parts of the incident waves pass through the slot array, but some of the waves are blocked by the copper ground plane and reflect back. This slot array with the equal slot aperture acts as a prototype array, and the performances are evaluated to make comparisons with various slot aperture array. All mutual coupling effects are assumed small and ignored in this work.

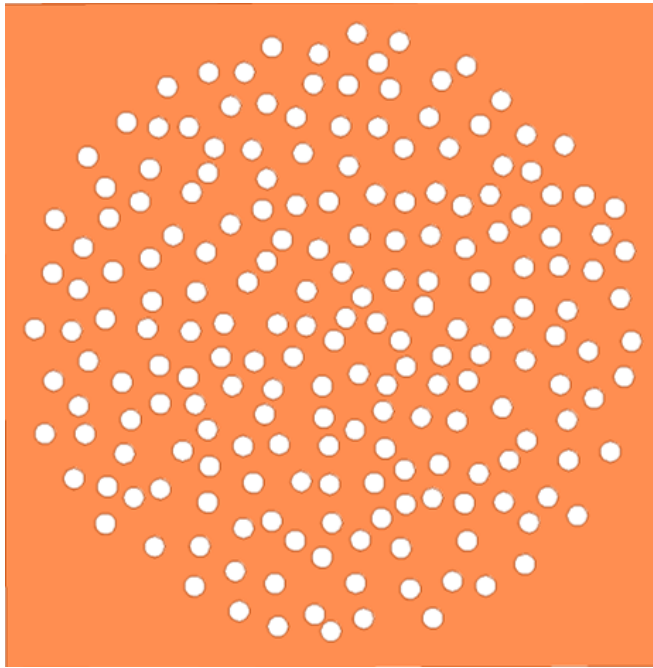


Figure 60 A two-hundred-element slot array prototype simulated in the HFSS.

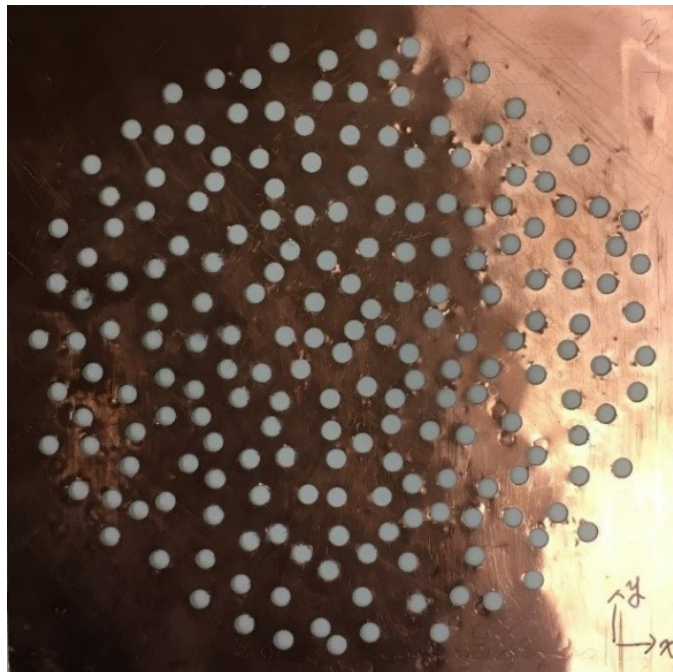


Figure 61 A photo of the two-hundred-element slot array prototype.

In addition, the copper sheet is thin and flexible; therefore, two transparent plastic plates are designed to sandwich the copper sheet, which becomes more rigid (as shown in Fig. 62).

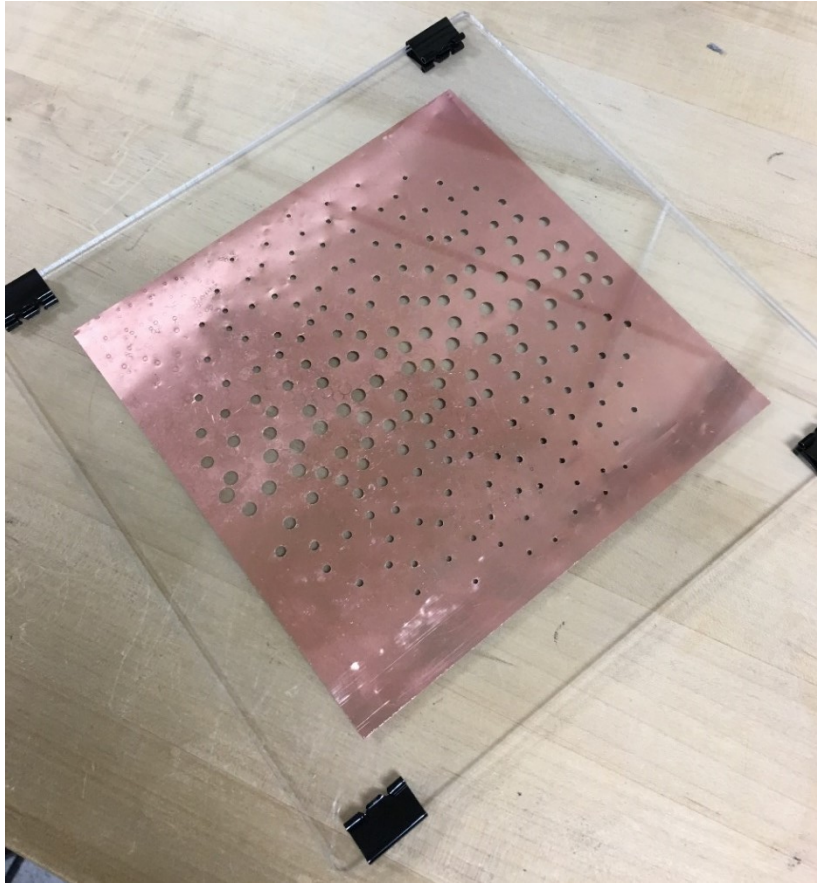


Figure 62 A photo of the slot array in the middle of two plastic board.

6.2.2. Circular Slots

The first work in this experiment is to determine the slot aperture. The radius of the slot aperture is designed as big as possible to allow more electric fields to pass;

however, it still needs to maintain the diffraction characteristics. A 2.5 mm slot aperture in radius is selected as the biggest aperture size. On the other hand, the lower bound of the slot aperture is set to 1.5 mm in radius. Using circular slots instead of rectangular slots allows different polarized waves to pass; therefore, a more extensive advanced beamforming method, such as a circular polarized beamforming, can be implemented for future work. Another reason is that the slot array can be rotated to emulate as another new slot array without actually making a new one.

6.2.3. Plane Wave Excitation

A plane wave is used in the simulation as the incident waves to excite the slot array, although a uniform plane wave does not exist in the real world [13]. One well-known feature of the plane wave is that the power density and phases are uniform everywhere along the wavefront. The average power density \bar{S}_{av} of a plane wave is described as

$$\bar{S}_{av} = \hat{z} \frac{|\bar{E}|^2}{2\eta} \text{ (w/m}^2\text{)}, \quad (22)$$

where η is intrinsic impedance of the free space; \hat{z} indicates the wave propagation direction, and \bar{E} is the electric field of the electromagnetic wave.

6.3. Array Beamshaping

Developing systematic beamshaping procedures for a slot array is one of our task in this experiment. Instead of using the same size of circular slots illustrated in [52], this work uses various sizes of circular slots to distribute tapered amplitudes to each array element. Clearly, the larger slot aperture results in a stronger electrical field. One reason

for this is that the amplitudes are much easier to facilitate by changing the slot aperture than using a LNA. Using a LNA with a gain range of 30 dB is impractical and expensive.

The Binomial coefficients of “1, 6, 15, 20, 15, 6, 1” are selected as the amplitude tapering curve because large coefficients of variation are more effective in this experiment. We recognize that the average SLL of the random array is inversely proportional to the array elements. For two hundred random array elements, the expected average SLL is around -20 dB. Thus, a large tapering coefficient of variation has to be adopted to strengthen the tapering effects.

To implement the idea, correctly assigning the right slot aperture to each circular slot is crucial. Therefore, extensive calculations are involved and the procedures are elaborated on in this section thoroughly. With the correct calculations and amplitude distributions, a high gain radiation pattern together with a low SLL for the slot array is expected. Simulated beamshaping results for azimuth and 3π scans are evaluated, and all the experiments are designed and operated at 60 GHz.

6.3.1. Tapering Method

For phased array applications, there are normally three kinds of scans can be categorized, including azimuth scans, elevation scans, and 3π scans. These three kinds of scans are related to horizontal, vertical, and radial tapering, respectively. Both horizontal and radial amplitude tapering methods are demonstrated in this section.

6.3.2. Find the Array Aperture

To deliver a precise current distribution to each circular slot, it is imperative to find the array aperture and determine the aperture origin. For radial tapering, the array aperture is designated as the smallest region that encloses the whole circular slots; for horizontal tapering, the array aperture is designated as the smallest region that encloses the utmost left and right circular slots. Both array apertures are orthogonal to the scan angle vector \bar{S} . Fig. 63 shows two hundred circular slots projected on the array aperture. Keep in mind, the array aperture changes with the scan angle.

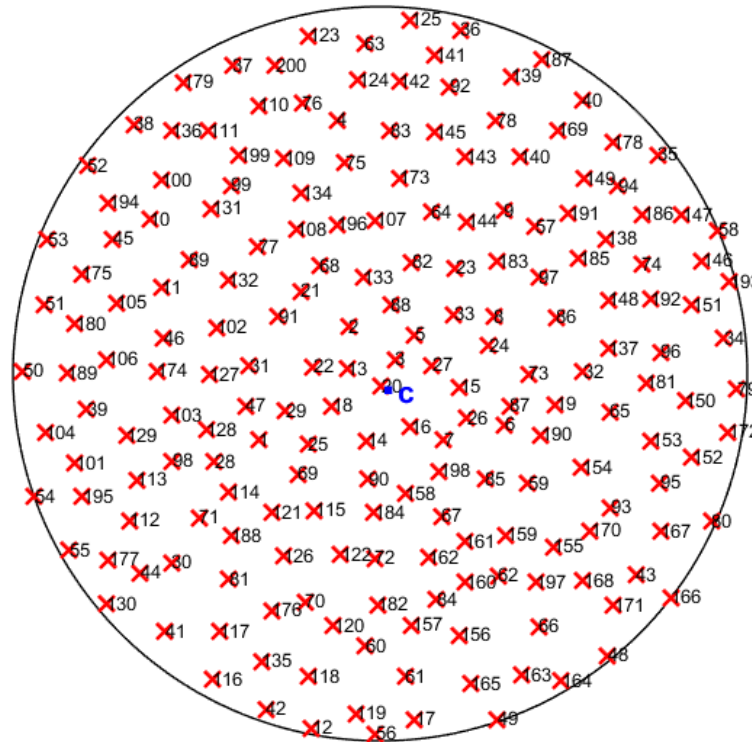


Figure 63 Two hundred circular slots (red cross) projected on the array aperture, and the center blue dot is the aperture origin.

6.3.3. Distribution Counts

For horizontal tapering, one reference vector \bar{u} is essential to create by

$$\bar{u}(x, y, z) = (\cos\theta_s \cos\phi_s, \cos\theta_s \sin\phi_s, -\sin\theta_s). \quad (23)$$

Next, project the circular slots to the \bar{u} vector, and the projection vectors of each circular slot are used to determine the distribution counts. Fig. 64 displays the distribution counts of the circular slots within each segment, the counts around the array aperture origin are much higher than that around the edges. Therefore, while elements around the array aperture origin have to reduce the amplitudes, elements at the edges have to increase them. The adjustment of the amplitudes by the counts is shown in Fig. 65.

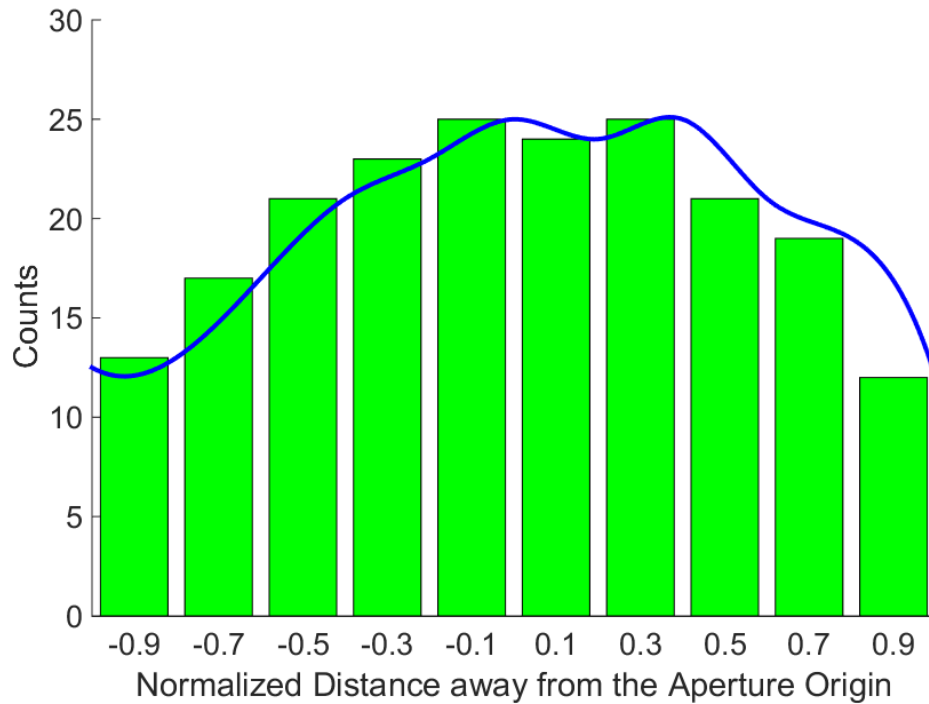


Figure 64 Counts distribution along the array aperture – horizontal tapering.

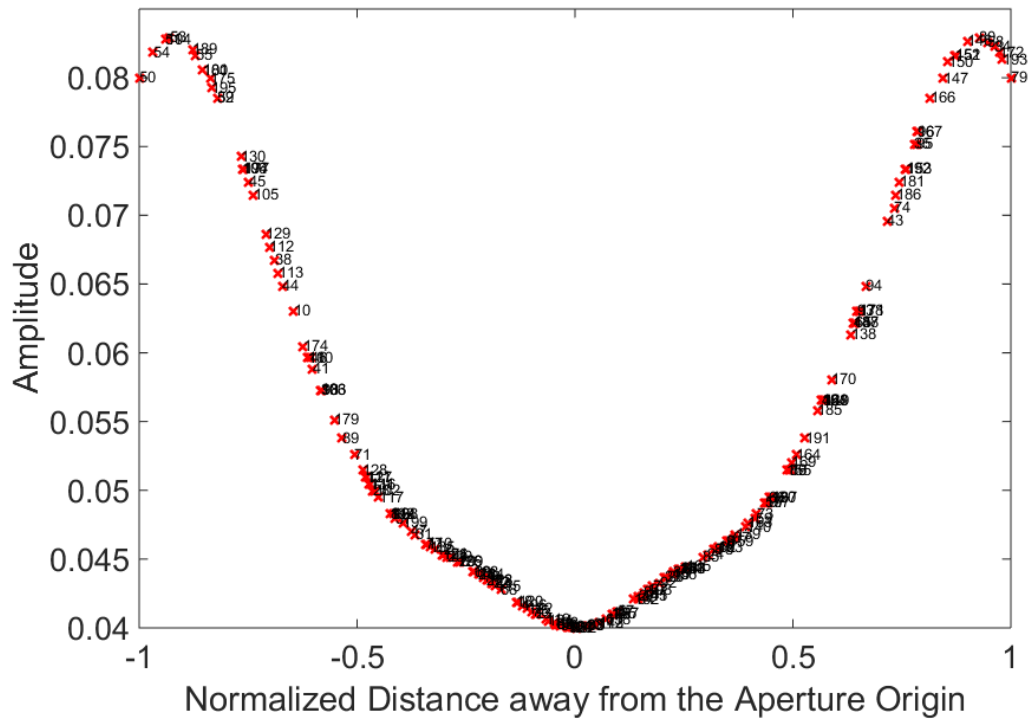


Figure 65 Amplitude adjustment according to the counts – horizontal tapering.

Similarly, for radial tapering, the radius of each circular slot is used to determine the distribution counts. In Fig. 66 displays the distribution counts of the circular slots within each segment. On the contrary, the counts around the array aperture origin are much lower than the counts around the edges. As a result, elements around the array aperture origin have to increase the amplitudes, whereas elements at the edges have to reduce the amplitudes. The result after adjusting the amplitudes by the counts is shown in Fig. 67.

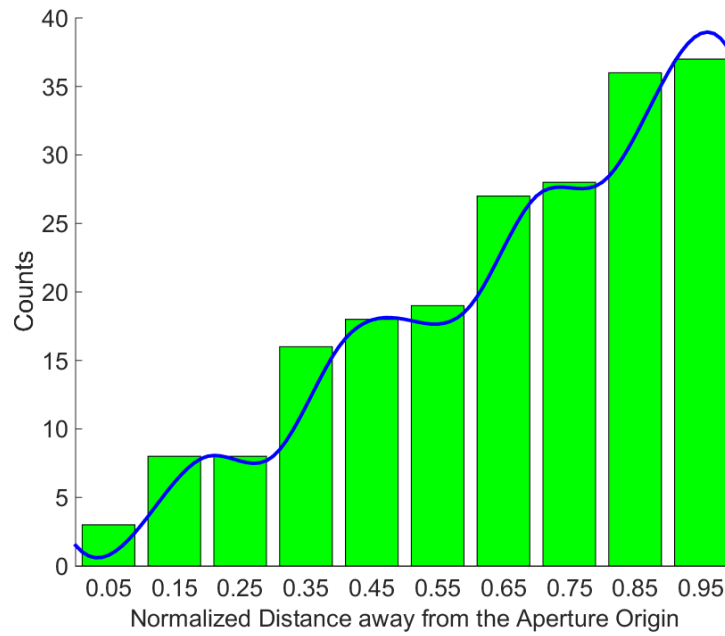


Figure 66 Distribution counts slots along the array aperture – radial tapering.

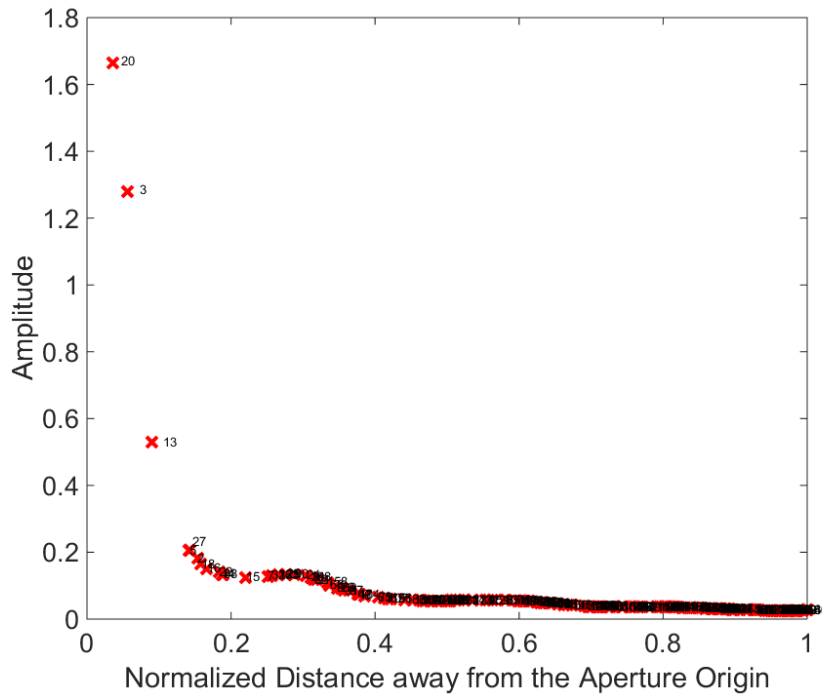


Figure 67 Amplitude adjustment according to the counts – radial tapering.

6.3.4. Amplitude Mapping

For horizontal tapering, the projection vectors of each circular slot are used to determine the corresponding tapered amplitudes. In this work, the Binomial coefficients of “1, 6, 15, 20, 15, 6, 1” are implemented as the amplitude tapering curve along the array aperture. Fig. 68 displays the mapping amplitudes of each array element along the array aperture. The elements around the aperture origin have the higher tapered amplitude, and elements around the edge have the lower tapered amplitude. The red crosses are the mapping amplitudes of each element.

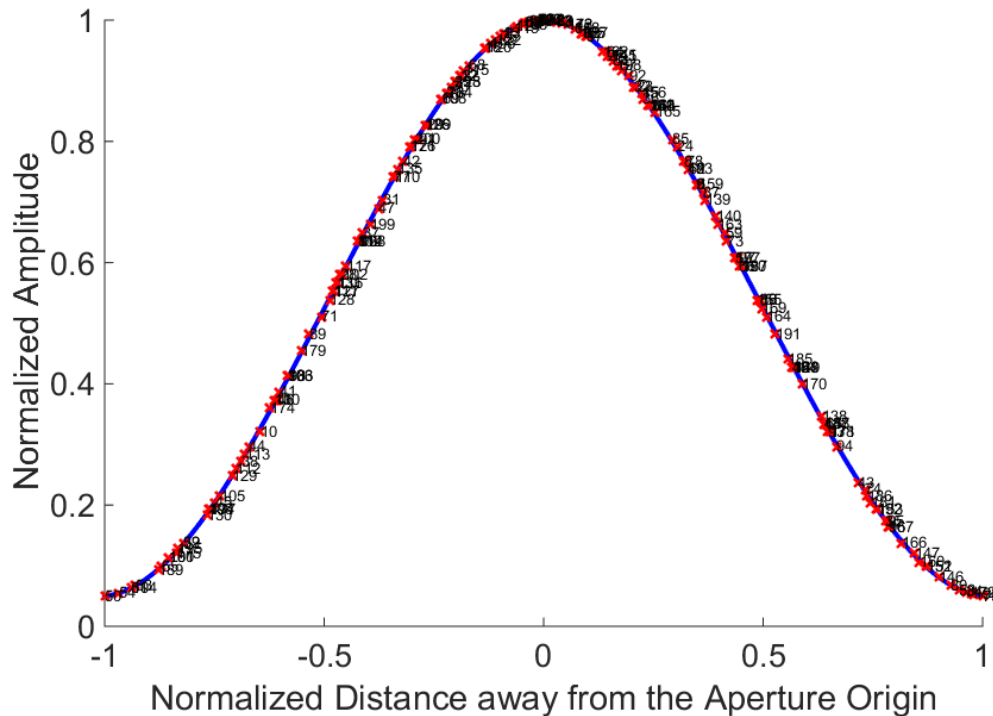


Figure 68 Two hundred circular slots map to the normalized amplitude tapering curve

(blue curve) – horizontal tapering.

For radial tapering, the radius of each circular slot is used to determine the corresponding tapered amplitudes. Fig. 69 displays the mapping amplitudes of each array element along the array aperture. The elements around the aperture origin have the higher tapered amplitude, and elements around the edge have the lower tapered amplitude.

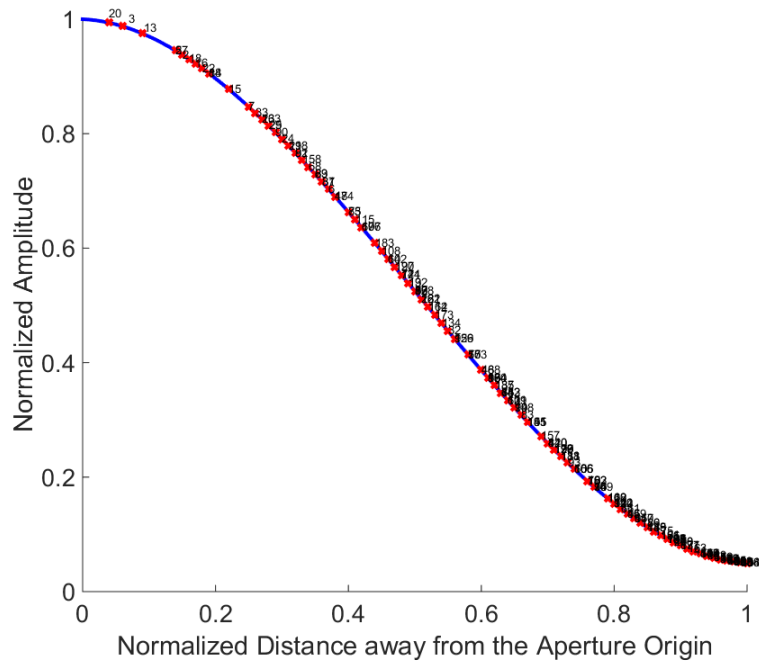


Figure 69 Two hundred circular slots map to the normalized amplitude tapering curve (blue curve) – radial tapering.

6.3.5. Slot Aperture vs. Amplitude

A major feature in this experiment is the use of various slot aperture to distribute the intensity of the amplitude. For this reason, a plot displays in Fig. 70 gives the relation

between the slot aperture and the field amplitudes, and, obviously, the larger slot aperture has stronger field amplitude. The amplitudes decrease linearly from aperture radius of 2.5 mm to 1.5 mm, and exponentially from aperture radius of 1.5 to 0.5 mm. The amplitudes exponentially drop from 0.5mm to 1.5 mm.

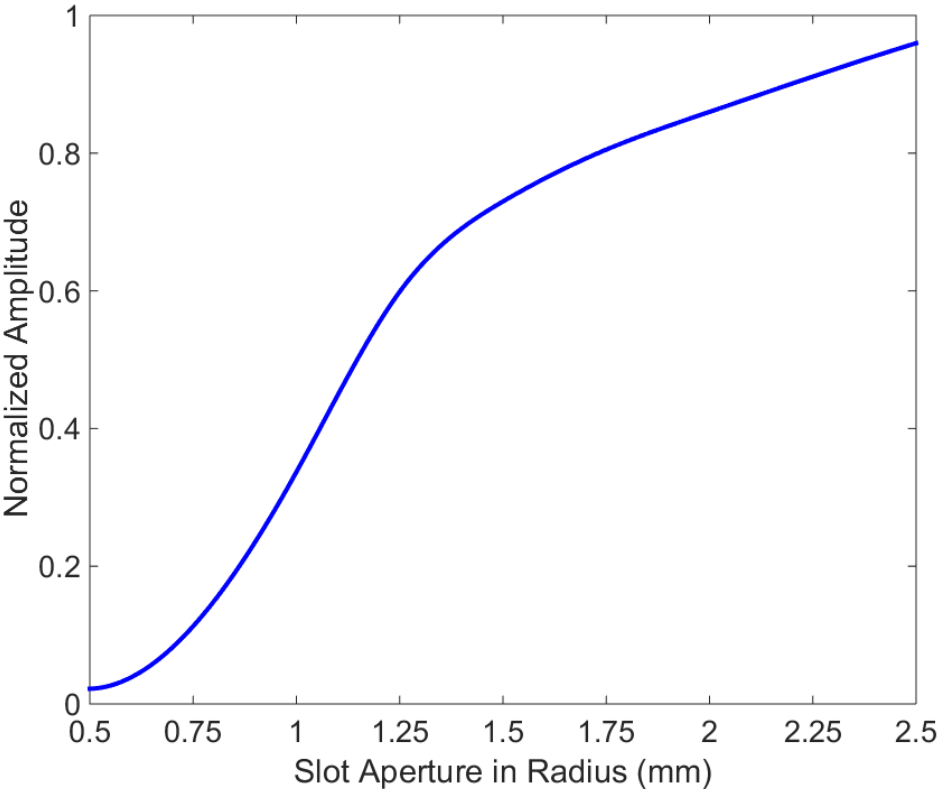


Figure 70 Field amplitudes vs. slot aperture.

For horizontal tapering, the final estimated aperture radius of each array element is shown in Fig. 71. The aperture radius ranges from 0.75 mm to 2.5 mm.

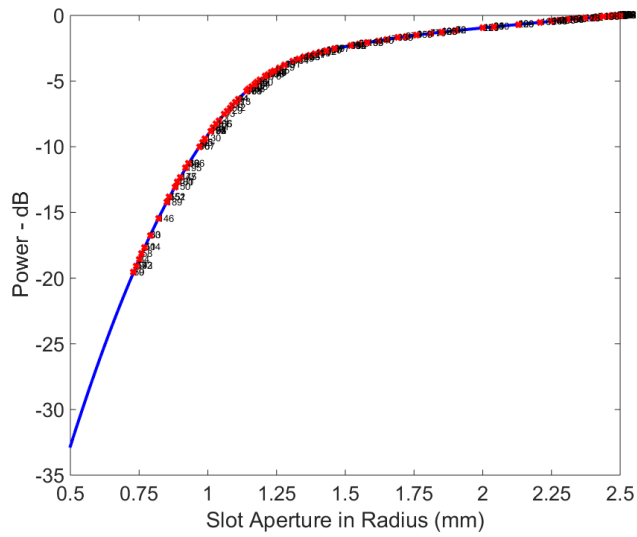


Figure 71 The estimated slot aperture for each circular slot – horizontal tapering.

For radial tapering, the final estimated aperture radius of each array element is shown in Fig. 72. The aperture radius ranges from 0.61 mm to 2.5 mm.

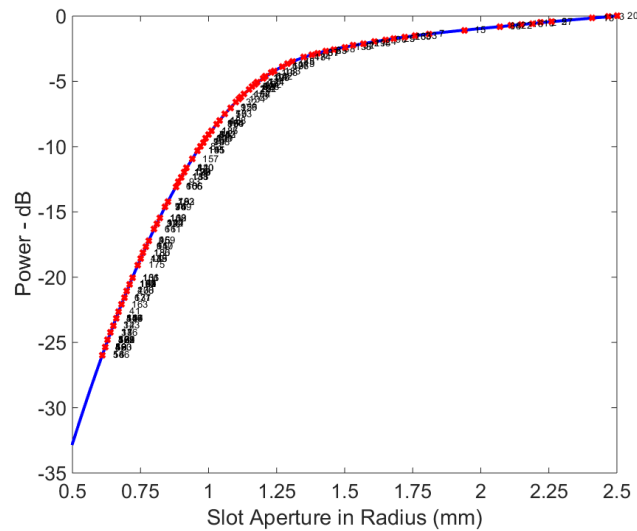


Figure 72 The estimated slot aperture for each circular slot – radial tapering.

6.4. Array Indirect Beamforming

The beam scanning capability of a slot array is examined in this section. Apart from the direct beamforming method described in [33], the slot array steers the main beam by changing the angles of the incident waves. Therefore, this kind of beamforming method is categorized as the indirect beamforming, and it is different from the direct beamforming and reflect beamforming as discussed respectively in Chapter 2 and Chapter 5. One phenomenon found is that the scan angle of the slot array is proportional to the angle of the incident wave. The incident angle is defined as the angle between the normal vector of the plane and the ray. For example, if the plane wave has an incident angle of 30° , the array has a scan angle of 30° .

6.5. Simulation Results

I had conducted two experiments in this section. First, the slot array with horizontal and radial tapering (as shown in Fig. 73 and Fig. 74) were tested, and the simulation results were compared to the slot array prototype. In addition, the slot array with radial tapering design was rotated by 90° to simulate as another new array. The slot array shown in Fig. 73 has slot aperture from 0.75 mm to 2.5mm, and the slot array shown in Fig. 74 has slot aperture from 0.6 mm to 2.5mm. Both arrays have circular slots distributed uniformly over an array aperture of 15λ in radius. The second part of the experiment was to prove the beam scanning capability by changing the incident angles of the signal source. Two kinds of tapering designs along with the prototype were examined and compared in this part. A plane wave excitation was chosen as the signal source in this simulation, and all the work was simulated in the HFSS.

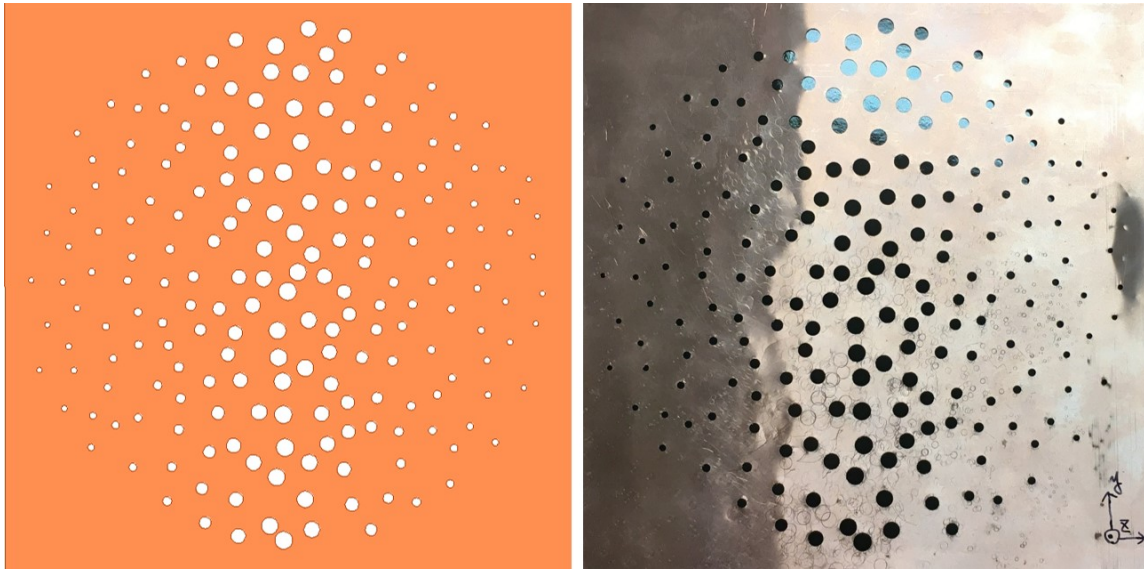


Figure 73 The slot array with horizontal tapering modeled in the HFSS (left), and the fabricated plate (right).

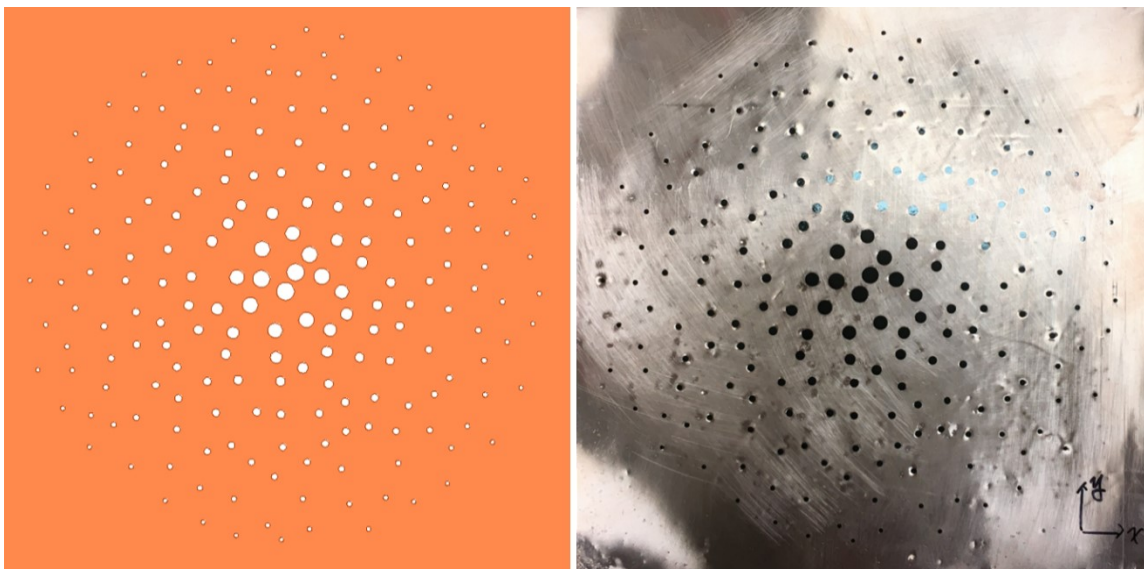


Figure 74 The slot array with radial tapering modeled in the HFSS (left), and the fabricated plate (right).

In Fig. 75, the simulated radiation pattern of the slot array prototype has the maximum gain of 51.2 dB at $(\theta, \phi) = (0^\circ, 0^\circ)$ and a -19.1 dB SLL is observed. The maximum sidelobe is 32.1 dB at $(\theta, \phi) = (3.2^\circ, 0^\circ)$. The radiation pattern with horizontal tapering is normalized to the maximum gain of the slot array prototype for comparison. For horizontal tapering result, it has a SLL of -18.5 dB, and the maximum sidelobe is 32.7 dB at $(\theta, \phi) = (-31^\circ, 0^\circ)$.

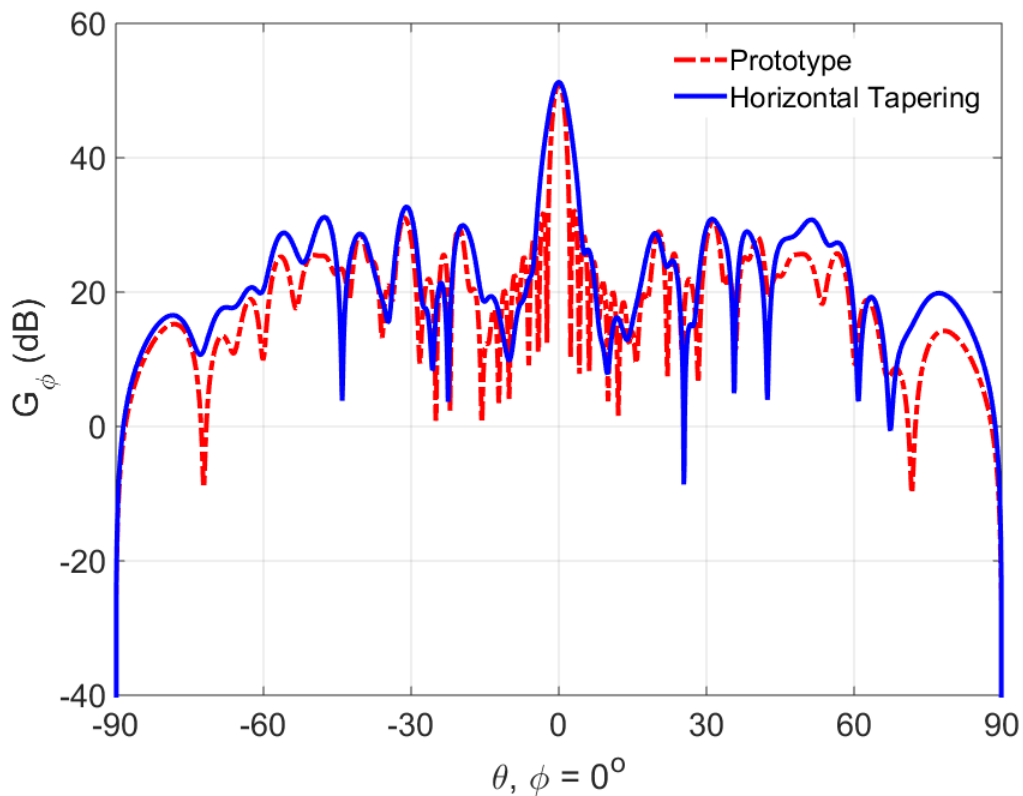


Figure 75 Simulation results of the slot array prototype and the array with horizontal tapering.

In Fig. 76, the radiation pattern with radial tapering is normalized to the maximum gain of the slot array prototype for a better comparison. For radial tapering result, it has a SLL of -18.5 dB, and the maximum sidelobe is 32.7 dB at $(\theta, \phi) = (-31^\circ, 0^\circ)$.

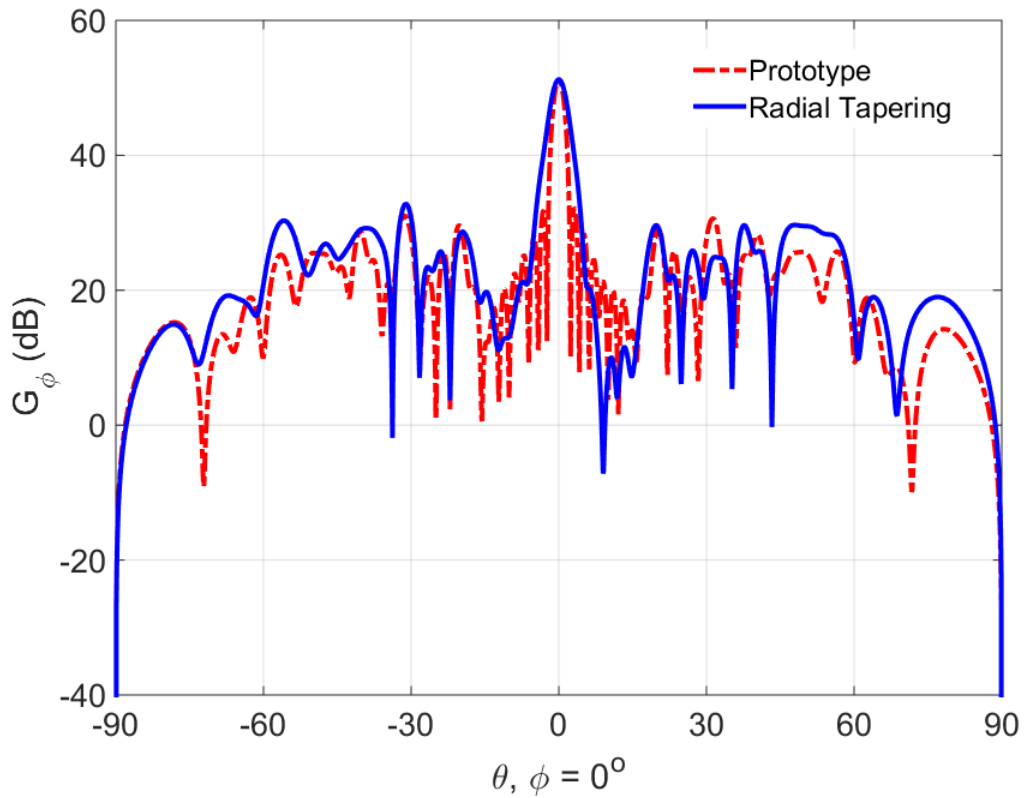


Figure 76 Simulation results of the slot array prototype and the array with radial tapering.

In Fig. 77, the original slot array with radial tapering is rotated by 90° to act as a brand-new slot array. The radiation pattern with radial tapering is normalized to the

maximum gain of the slot array prototype, which is 51.2 dB at $(\theta, \phi) = (0^\circ, 0^\circ)$, for a better comparison. For radial tapering result, it has a SLL of -16.7 dB, and the maximum sidelobe is 34.5 dB at $(\theta, \phi) = (-30^\circ, 0^\circ)$.

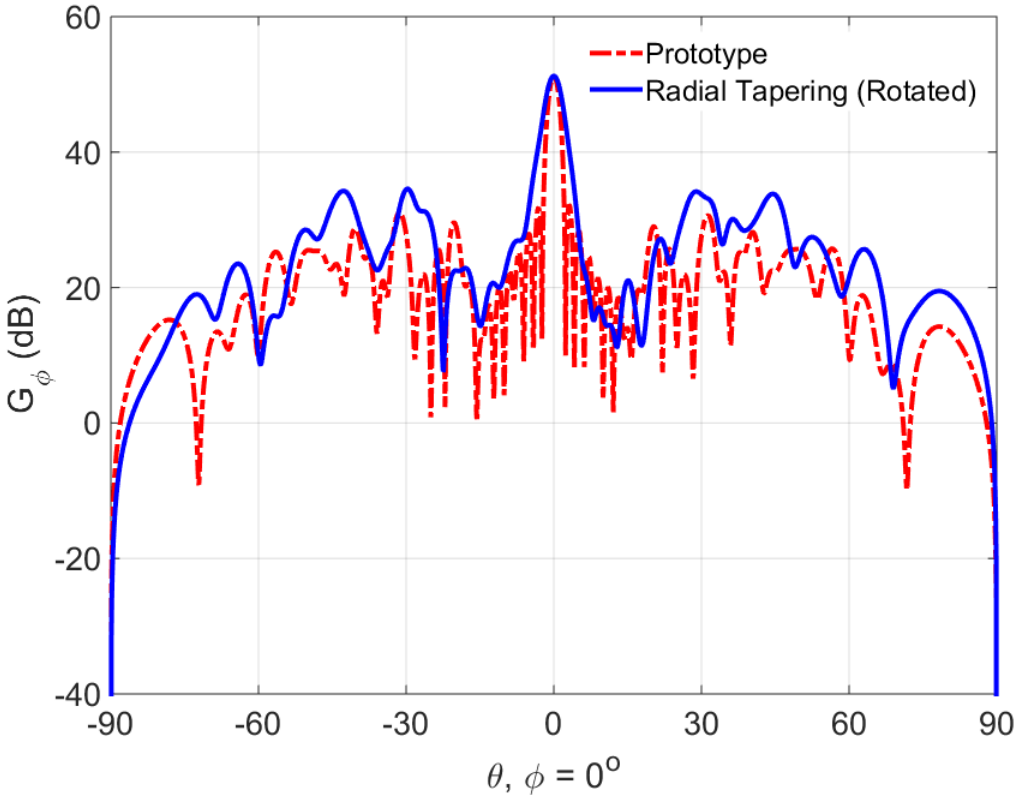


Figure 77 Simulation results of the slot array prototype and the rotated array with radial tapering.

Next, the beam scanning capabilities are investigated by changing the incident angles of the plane wave. Therefore, a plane wave with 30° incident angle is adopted in the

following tests. In Fig. 78, the simulated radiation pattern of the slot array prototype has the maximum gain of 59.3 dB at $(\theta, \phi) = (30^\circ, 0^\circ)$ and an -18.95 dB SLL is observed. The maximum sidelobe is 40.35 dB at $(\theta, \phi) = (-1.1^\circ, 0^\circ)$. The radiation pattern with horizontal tapering is normalized to the maximum gain of the slot array prototype for a better comparison. For horizontal tapering result, it has a SLL of -16.1 dB, and the maximum sidelobe is 43.2 dB at $(\theta, \phi) = (-14^\circ, 0^\circ)$.

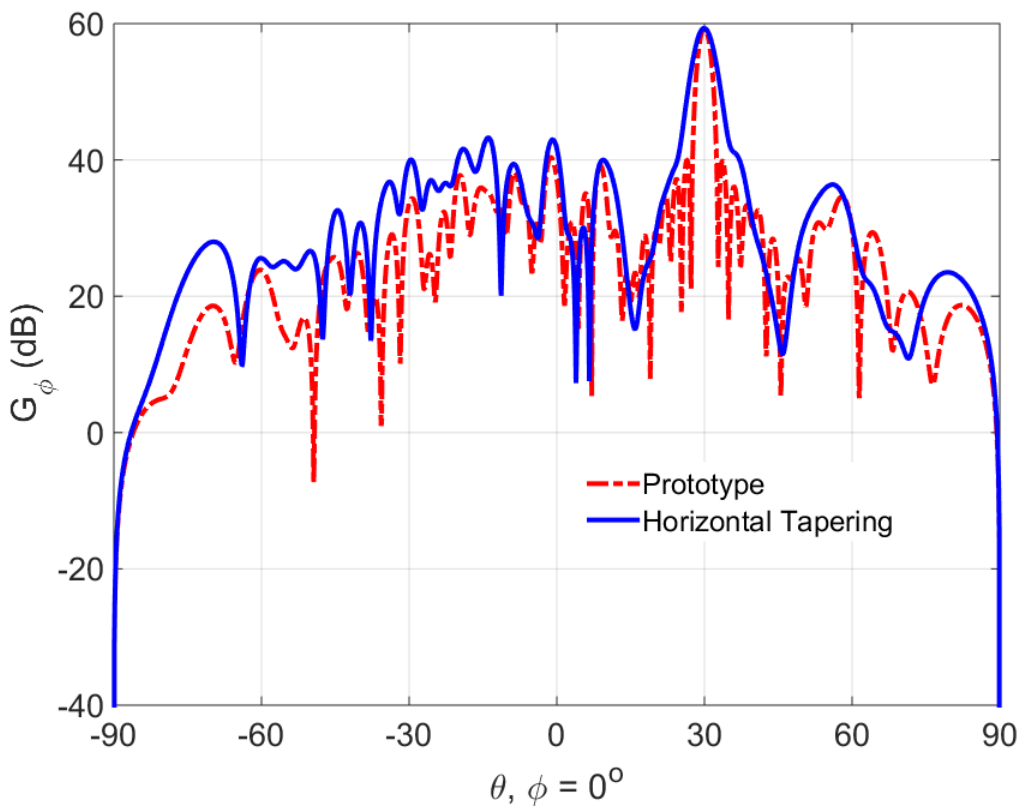


Figure 78 Simulation results of the slot array prototype and the array with horizontal tapering for $(\theta_i, \phi_i) = (30^\circ, 0^\circ)$.

In Fig. 79, the radiation pattern with radial tapering is normalized to the maximum gain of the slot array prototype for a better comparison. For radial tapering result, it has a SLL of -16.1 dB, and the maximum sidelobe is 43.2 dB at $(\theta, \phi) = (-1^\circ, 0^\circ)$.

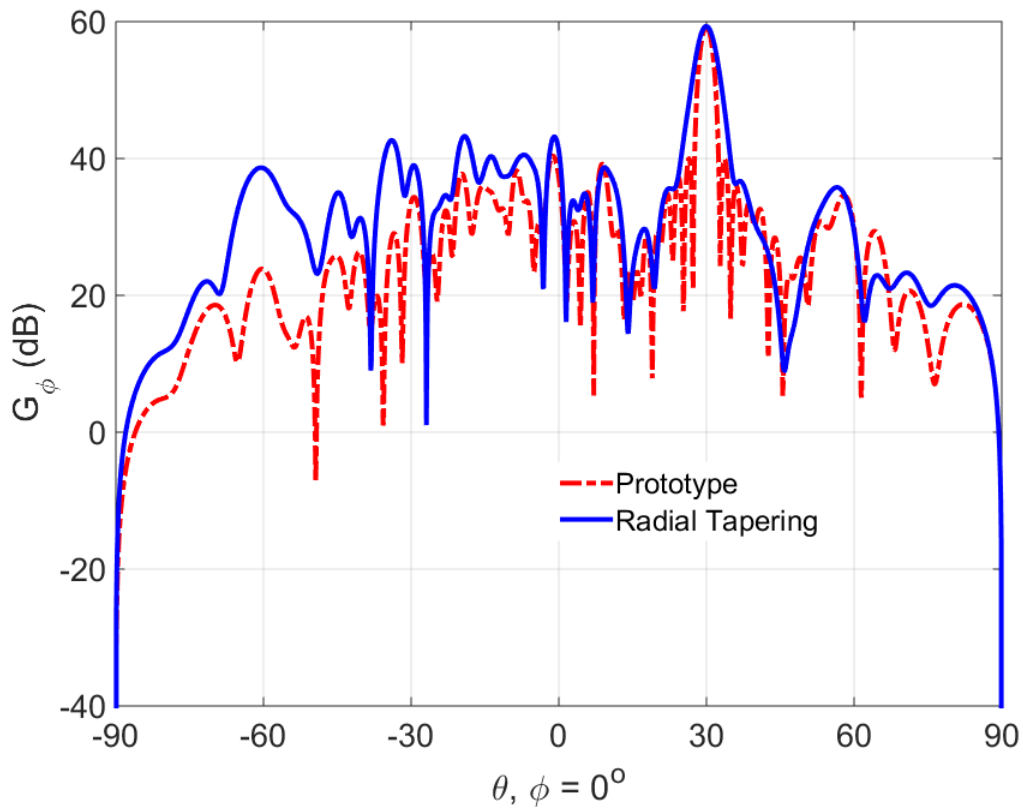


Figure 79 Simulation results of the slot array prototype and the array with radial tapering for $(\theta_i, \phi_i) = (30^\circ, 0^\circ)$.

For the slot array with radial tapering and rotated by 90° , the radiation pattern (as shown in Fig. 80) is normalized to the maximum gain of the slot array prototype for a better

comparison. For radial tapering result, it has a SLL of -12.5 dB, and the maximum sidelobe is 46.8 dB at $(\theta, \phi) = (-10.5^\circ, 0^\circ)$.

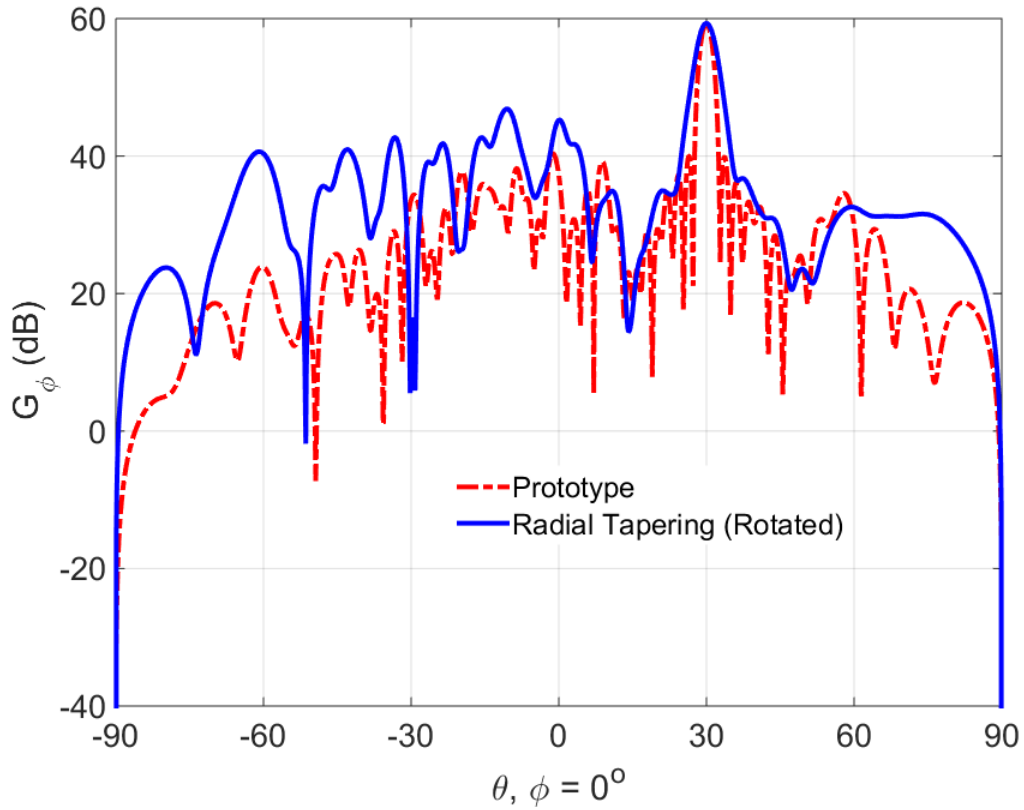


Figure 80 Simulation results of the array prototype and the rotated array with radial tapering for $(\theta_i, \phi_i) = (30^\circ, 0^\circ)$.

After applying tapered amplitudes to each array element, there is no significant sidelobe reduction observed in these tests; however, the maximum sidelobe moves greatly

away from the main beam. The sidelobes around the main beam are merged into it. Even though the plate is rotated by 90° , the effect of beamshaping can still be recognized.

The reasons that the sidelobe reduction effects are not noticeable can be analyzed as follows. First, the array prototype already has a large number of random elements. As mentioned in Chapter 1, the average SLL of the random array is inversely proportional to the array elements. For two hundred random circular slots, an average SLL of -23.01 dB is expected. Therefore, for a large number of random array, the sidelobe reduction is trivial. Second, the array prototype already has density tapering characteristic by nature, and the SLL is further reduced.

Combining all these points, even though a large variation of Binomial coefficients is used in this test, the effects of the sidelobe reduction are still minor. Therefore, an anechoic chamber measurement is not implemented in this work. At last, the tapering method goes with the side effects of broader beamwidth, decreased directivity, and lower aperture efficiency.

6.6. Conclusion

This work has successfully developed an amplitude tapering algorithm and an indirect beamforming method specifically for the slot array. The procedures of amplitude tapering are clearly illustrated and explained. The slot array that scans the main beam by changing the incident angle of the plane wave was implemented. Finally, simulated results of tapering, and non-tapering are provided to benchmark the beamshaping performance.

7. CONCLUSION AND FUTURE WORK

This dissertation clearly explains the fundamental ideas of the phased array, volumetric array, random array, circular polarization, mobile platform, and wireless phased synchronization. The ultimate goal of wireless phased array applications carried out by mobile platforms was proposed. Three challenges to realize the idea are illustrated. Five projects developed in this dissertation provide the solutions to attain this goal. The first three projects are related to the beamforming and beamshaping algorithms, and the last two are about its applications.

For future work, it is observed that the use of coaxial cables in volumetric array resulted in additional scattering, shielding, and shadowing issues. Although most of the supporting substance comes from wood or plastic material in the experiment, there are still some effects from the coaxial cables. A better way to diminish the effects once and for all is to adopt fiber optics instead of coaxial cables. Fiber optics are proven to provide both RF signals [53] and DC power [54] to the antennas, and without a doubt, fiber material is merely transparent at RF. Other advantages of employing fiber optics, such as low loss and wider bandwidth, are also reported in [54].

REFERENCES

- [1] D. C. Jenn, J. H. Ryu, T. Yen-Chang and R. Broadston, "Adaptive phase synchronization in distributed digital arrays," 2010 NASA/ESA Conference on Adaptive Hardware and Systems, Anaheim, CA, USA, 2010, pp. 199-204.
- [2] T. Noguchi, Y. Daido and J. Nossek, "Modulation techniques for microwave digital radio," in IEEE Communications Magazine, vol. 24, no. 10, pp. 21-30, October 1986.
- [3] J. R. van der Merwe, W. P. du Plessis, F. D. V. Maasdorp and J. E. Cilliers, "Introduction of low probability of recognition to radar system classification," 2016 IEEE Radar Conference (RadarConf), Philadelphia, PA, 2016, pp. 1-5.
- [4] M. Khan and D. Chatterjee, "Effect of feeding techniques on U-slot loaded microstrip patch," 2016 IEEE International Symposium on Antennas and Propagation (APSURSI), Fajardo, 2016, pp. 195-196.
- [5] Buchanan, K.; Huff, G.H., "A Stochastic Mathematical Framework for the Analysis of Spherically-Bound Random Arrays," in Antennas and Propagation, IEEE Transactions on, vol.62, no.6, pp.3002-3011, June 2014.
- [6] Tennant, A.; Fray, A.F., "A 64 element broad band volumetric array antenna," in Antennas and Propagation Society International Symposium, 1998. IEEE, vol.3, no., pp.1417-1420 vol.3, 21-26 June 1998.
- [7] Barott, W.C.; Steffes, P.G., "A 3-D Pattern-Space Representation for Volumetric Arrays," in Antennas and Wireless Propagation Letters, IEEE, vol.7, no., pp.528-531, 2008.

- [8] J. M. Rigelsford and A. Tennant, "A Synthetic Acoustic Volumetric Array," Fourth IEEE Workshop on Sensor Array and Multichannel Processing, 2006., Waltham, MA, 2006, pp. 313-314.
- [9] C. Fischer, S. Appel, W. Gautier and W. Gruener, "Performance Characterization of a Polarisation Agile Wideband AESA," 2017 European Radar Conference (EURAD), Nuremberg, 2017, pp. 417-420.
- [10] A. Tennant, A. F. Fray, D. B. Adamson and M. W. Shelley, "Beam scanning characteristics of 64 element broadband volumetric array," in Electronics Letters, vol. 33, no. 24, pp. 2001-2002, 20 Nov 1997.
- [11] Shihyuan Yeh, "Development of a Digital Tracking Array with Single-Channel RSNS and Monopulse Digital Beamforming," M.S. thesis, Department of Electrical and Computer Engineering, Naval Postgraduate School, Monterey, California, 2010.
- [12] H. Wilden and J. Ender, "The Crow's-Nest Antenna - Special Aspects and Results," Microwave Conference, 1987. 17th European, Rome, Italy, 1987, pp. 509-514.
- [13] O. V. Doroshenko, "Plane wave propagation in elastic media with doubly periodic array of planar delaminations," 2017 Days on Diffraction (DD), St. Petersburg, 2017, pp. 94-99.
- [14] O. S. Dautov, "Excitation of the nonmagnetic isotropic media with linear dependence characteristic impedance along the direction of plane wave propagation," 2017 XI International Conference on Antenna Theory and Techniques (ICATT), Kiev, 2017, pp. 125-127.

- [15]B. K. Feng and D. C. Jenn, "Two-Way Pattern Grating Lobe Control for Distributed Digital Subarray Antennas," in IEEE Transactions on Antennas and Propagation, vol. 63, no. 10, pp. 4375-4383, Oct. 2015.
- [16]S. Isaacson, "Enhancement of radar signals by double bounce circular polarization," 1958 IRE International Convention Record, New York, NY, USA, 1961, pp. 10-16.
- [17]H. El-Ocla, "Radar cross-section of conducting targets in random media for circular polarization," Canadian Conference on Electrical and Computer Engineering, 2005., Saskatoon, Sask., 2005, pp. 1433-1436.
- [18]C. Chen and A. Babakhani, "Wireless synchronization of mm-wave arrays in 65nm CMOS," 2015 IEEE Custom Integrated Circuits Conference (CICC), San Jose, CA, 2015, pp. 1-4.
- [19]D. R. Brown, G. B. Prince and J. A. McNeill, "A method for carrier frequency and phase synchronization of two autonomous cooperative transmitters," IEEE 6th Workshop on Signal Processing Advances in Wireless Communications, 2005., 2005, pp. 260-264.
- [20]S. Berger and A. Wittneben, "Carrier phase synchronization of multiple distributed nodes in a wireless network," 2007 IEEE 8th Workshop on Signal Processing Advances in Wireless Communications, Helsinki, 2007, pp. 1-5.
- [21]Harrington, R.F., "Sidelobe reduction by nonuniform element spacing," in Antennas and Propagation, IRE Transactions on, vol.9, no.2, pp.187-192, March 1961.
- [22]Buchanan, K.; Huff, G.H., "Analysis and experiments on peaking sidelobe and scanning behavior in planar random arrays," in Antennas and Propagation Society

International Symposium (APSURSI), 2014 IEEE, vol., no., pp.1369-1370, 6-11 July 2014.

[23] Wilden, H.; Ender, J., "The crow's nest antenna-experimental results," in Radar Conference, 1990., Record of the IEEE 1990 International, vol., no., pp.280-285, 7-10 May 1990.

[24] Deshpande, M.; Das, N., "Rectangular microstrip antenna for circular polarization," in Antennas and Propagation, IEEE Transactions on, vol.34, no.5, pp.744-746, May 1986.

[25] Tranquilla, J.; Best, S., "Phase center considerations for the monopole antenna," in Antennas and Propagation, IEEE Transactions on, vol.34, no.5, pp.741-744, May 1986.

[26] I. V. Lindell, A. Sihvola and A. Favaro, "Plane wave propagation in extreme magnetoelectric (EME) medium," 2016 URSI International Symposium on Electromagnetic Theory (EMTS), Espoo, 2016, pp. 84-85.

[27] G. H. Huff, J. F. Chamberland, and J. S. Jensen, "Cognitive Motion-Dynamic Tethering of a Phased Array to an Android Smartphone," in IEEE Transactions on Antennas and Propagation, vol. 62, no. 3, pp. 1093-1101, March 2014.

[28] H. Wilden, "Crow's-nest antenna," in Electronics Letters, vol. 16, no. 7, pp. 256-257, March 27 1980.

[29] J. S. Jensen and G. H. Huff, "A cognitive spatial learning control system for volumetric random arrays," Radio Science Meeting (Joint with AP-S Symposium), 2015 USNC-URSI, Vancouver, BC, Canada, 2015, pp. 223-223.

- [30] G. Burnsed, D. Kalcik and J. Sherman, "C-band analog monolithic vector modulator," IEEE 1995 Microwave and Millimeter-Wave Monolithic Circuits Symposium. Digest of Papers, Orlando, FL, USA, 1995, pp. 91-94.
- [31] S. Bingham and B. Krause, "Broadband 1.5 GHz analog monolithic vector modulator," GaAs IC Symposium Technical Digest 1992, Miami Beach, FL, USA, 1992, pp. 33-36.
- [32] M. Emara, P. Rosson, K. Roth and D. Dassonville, "A Full Duplex Transceiver with Reduced Hardware Complexity," GLOBECOM 2017 - 2017 IEEE Global Communications Conference, Singapore, 2017, pp. 1-6.
- [33] Shihyuan Yeh, J. F. Chamberland and G. H. Huff, "An investigation of geolocation-aware beamforming algorithms for swarming UAVs," 2017 IEEE International Symposium on Antennas and Propagation & USNC/URSI National Radio Science Meeting, San Diego, CA, USA, 2017, pp. 641-642.
- [34] N. T. Binh, N. Q. Dinh, Y. Yamada and N. Michishita, "Design of density tapered array for arbitrary density distribution," 2016 International Conference on Advanced Technologies for Communications (ATC), Hanoi, 2016, pp. 375-379.
- [35] B. K. Feng and D. C. Jenn, "Grating Lobe Suppression for Distributed Digital Subarrays Using Virtual Filling," in IEEE Antennas and Wireless Propagation Letters, vol. 12, pp. 1323-1326, 2013.
- [36] A. Kumar and P. Murthy, "Synthesis of equally excited linear arrays," in IEEE Transactions on Antennas and Propagation, vol. 25, no. 3, pp. 425-428, May 1977.

- [37] F. S. Topalov, Y. V. Yukhanov, I. V. Ilin and T. Y. Privalova, "Controlling van-atta array scattering characteristics with HITTITE HMC247 phase shifter," 2017 Progress in Electromagnetics Research Symposium - Spring (PIERS), St. Petersburg, 2017, pp. 2065-2068.
- [38] E. Gruenberg and C. Johnson, "Satellite communications relay system using a retrodirective space antenna," in IEEE Transactions on Antennas and Propagation, vol. 12, no. 2, pp. 215-223, Mar 1964.
- [39] Shyh-Jong Chung and Kai Chang, "A retrodirective microstrip antenna array," in IEEE Transactions on Antennas and Propagation, vol. 46, no. 12, pp. 1802-1809, Dec 1998.
- [40] J. G. D. Hester and M. M. Tentzeris, "Inkjet-Printed Flexible mm-Wave Van-Atta Reflectarrays: A Solution for Ultralong-Range Dense Multitag and Multisensing Chipless RFID Implementations for IoT Smart Skins," in IEEE Transactions on Microwave Theory and Techniques, vol. 64, no. 12, pp. 4763-4773, Dec. 2016.
- [41] M. S. Trotter, C. R. Valenta, G. A. Koo, B. R. Marshall and G. D. Durgin, "Multi-antenna techniques for enabling passive RFID tags and sensors at microwave frequencies," 2012 IEEE International Conference on RFID (RFID), Orlando, FL, 2012, pp. 1-7.
- [42] E. Sharp and M. Diab, "Van Atta reflector array," in IRE Transactions on Antennas and Propagation, vol. 8, no. 4, pp. 436-438, July 1960.
- [43] C. Gregory, M. Lueck, A. Huffman, J. M. Lannon and D. S. Temple, "High density metal-metal interconnect bonding with pre-applied fluxing underfill," 2012 IEEE

62nd Electronic Components and Technology Conference, San Diego, CA, 2012, pp. 20-25.

- [44] C. H. Kim and Y. S. Kwon, "Thick-Copper-Buried Inductors Using Anodized Aluminum Package Substrates," in *IEEE Transactions on Components, Packaging and Manufacturing Technology*, vol. 2, no. 8, pp. 1260-1264, Aug. 2012.
- [45] R. C. Waterman, W. Fabian, R. A. Pucel, Y. Tajima and J. L. Vorhaus, "GaAs monolithic Lange and Wilkinson couplers," in *IEEE Transactions on Electron Devices*, vol. 28, no. 2, pp. 212-216, Feb 1981.
- [46] C. C. Tsai, Y. S. Cheng, T. Y. Huang, Y. A. Hsu and R. B. Wu, "Design of Microstrip-to-Microstrip Via Transition in Multilayered LTCC for Frequencies up to 67 GHz," in *IEEE Transactions on Components, Packaging and Manufacturing Technology*, vol. 1, no. 4, pp. 595-601, April 2011.
- [47] W. Liu, Z. Zhang, Z. Feng and M. F. Iskander, "A Compact Wideband Microstrip Crossover," in *IEEE Microwave and Wireless Components Letters*, vol. 22, no. 5, pp. 254-256, May 2012.
- [48] J. W. Crispin and A. L. Maffett, "Radar cross-section estimation for simple shapes," in *Proceedings of the IEEE*, vol. 53, no. 8, pp. 833-848, Aug. 1965.
- [49] Y. Yamaguchi, J. Kamioka, M. Hangai, S. Shinjo and K. Yamanaka, "A CW 20W Ka-band GaN high power MMIC amplifier with a gate pitch designed by using one-finger large signal models," 2017 IEEE Compound Semiconductor Integrated Circuit Symposium (CSICS), Miami, FL, 2017, pp. 1-4.

- [50] Shihyuan Yeh and G. H. Huff, "A Magnetless Duplex Retrodirective Patch Array with Phase Shifter for Signal Relay," 41st Antenna Applications Symposium, University of Illinois at Urbana-Champaign, IL, USA, 2017, pp. 53-74
- [51] B. D. Braaten, S. Asif, S. Khan, J. Hansen and D. L. Ewert, "A compact printed Van Atta Array with zero-phase CRLH transmission lines," 2015 IEEE International Symposium on Antennas and Propagation & USNC/URSI National Radio Science Meeting, Vancouver, BC, 2015, pp. 1856-1857.
- [52] Y. Lo and R. Simcoe, "An experiment on antenna arrays with randomly spaced elements," in IEEE Transactions on Antennas and Propagation, vol. 15, no. 2, pp. 231-235, March 1967.
- [53] M. Oishi, T. Hirasawa, K. Furuya, S. Akiba, J. Hirokawa and M. Ando, "3.5-Gbit/s QPSK Signal Radio-Over-Fiber Transmission With 60-GHz Integrated Photonic Array-Antenna Beam Forming," in Journal of Lightwave Technology, vol. 34, no. 20, pp. 4758-4764, Oct.15, 15 2016.
- [54] Y. Minamoto and M. Matsuura, "Optically controlled beam steering system with 60-W power-over-fiber feed for remote antenna units," 2016 Optical Fiber Communications Conference and Exhibition (OFC), Anaheim, CA, 2016, pp. 1-3.